④

Technical Document 1325
August 1988

Electromagnetic Scattering and Radiation by Arbitrary Configurations of Conducting Bodies and Wires

S. U. Hwu
D. R. Wilton

Applied Electromagnetics Laboratory
Department of Electrical Engineering
University of Houston

DTIC
ELECTE
OCT 0 4 1988
S   H   D

88 10 4 095

NAVAL OCEAN SYSTEMS CENTER
San Diego, California 92152-5000

E. G. SCHWEIZER, CAPT, USN
Commander

R. M. HILLYER
Technical Director

ADMINISTRATIVE INFORMATION

This report was prepared by Applied Electromagnetics Laboratory, Department of Electrical Engineering, University of Houston, for Code 822 of the Naval Ocean Systems Center.

Released by
I. C. Olson, Head
Antenna and RF Systems
Integration Branch

Under authority of
G. E. Ereckson, Head
Shipboard Systems
Division

JJ

REPORT DOCUMENTATION PAGE

1a. REPORT SECURITY CLASSIFICATION UNCLASSIFIED		1b. RESTRICTIVE MARKINGS			
2a. SECURITY CLASSIFICATION AUTHORITY		3. DISTRIBUTION/AVAILABILITY OF REPORT			
2b. DECLASSIFICATION/DOWNGRADING SCHEDULE		Approved for public release; distribution is unlimited.			
4. PERFORMING ORGANIZATION REPORT NUMBER(S) Technical Report Number 87-17		5. MONITORING ORGANIZATION REPORT NUMBER(S) NOSC TD 1325			
6a. NAME OF PERFORMING ORGANIZATION Applied Electromagnetics Laboratory	6b. OFFICE SYMBOL (if applicable)	7a. NAME OF MONITORING ORGANIZATION Naval Ocean Systems Center			
6c. ADDRESS (City, State and ZIP Code) Department of Electrical Engineering University of Houston		7b. ADDRESS (City, State and ZIP Code) San Diego, CA 92152-5000			
8a. NAME OF FUNDING/SPONSORING ORGANIZATION David Taylor Research Center	8b. OFFICE SYMBOL (if applicable) DTNSRDC	9. PROCUREMENT INSTRUMENT IDENTIFICATION NUMBER N66001-85-D-0203			
8c. ADDRESS (City, State and ZIP Code) Bethesda, MD 20084		10. SOURCE OF FUNDING NUMBERS			

	PROGRAM ELEMENT NO.	PROJECT NO.	TASK NO.	AGENCY ACCESSION NO.
	62121N	CM41	RH21S 21	DN088 509

11. TITLE (include Security Classification)

ELECTROMAGNETIC SCATTERING AND RADIATION BY ARBITRARY CONFIGURATIONS OF CONDUCTING BODIES AND WIRES

12. PERSONAL AUTHOR(S)

S. U. Hwu, D. R. Wilton

13a. TYPE OF REPORT Final	13b. TIME COVERED FROM Oct 1987 TO Dec 1987	14. DATE OF REPORT (Year, Month, Day) August 1988	15. PAGE COUNT 101

16. SUPPLEMENTARY NOTATION

17. COSATI CODES			18. SUBJECT TERMS (Continue on reverse if necessary and identify by block number)
FIELD	GROUP	SUB-GROUP	electromagnetic environment effects electromagnetic interference

19. ABSTRACT (Continue on reverse if necessary and identify by block number)

This report extends the approach to develop a procedure for analyzing an arbitrary configuration of conducting wires and bodies.

20. DISTRIBUTION/AVAILABILITY OF ABSTRACT ☐ UNCLASSIFIED/UNLIMITED ☒ SAME AS RPT ☐ DTIC USERS		21. ABSTRACT SECURITY CLASSIFICATION UNCLASSIFIED	
22a. NAME OF RESPONSIBLE PERSON J. C. Logan		22b. TELEPHONE (include Area Code) (619) 553-3780	22c. OFFICE SYMBOL Code 822

DD FORM 1473, 84 JAN
83 APR EDITION MAY BE USED UNTIL EXHAUSTED
ALL OTHER EDITIONS ARE OBSOLETE

Contents

2

List of Figures

3

Chapter 1

Introduction

In recent years, researchers in electromagnetics have expended considerable effort capitalizing on computational advances made possible by new developments in computer technology. These advances have made it easier to develop highly efficient, specialized computer codes for many scattering or radiation problems. However, because of the high cost of developing a code for each specialized geometry, it has increasingly become more cost effective to use possibly less efficient, but more general purpose codes which apply to a broader class of problems.

Most general purpose codes employ an integral equation formulation which is solved by the method of moments [1]. Under this type of formulation, the structure geometry is usually modeled either as a wire mesh or as a surface subdivided into discrete planar patches. The wire grid geometry modeling approach has been successfully used where primarily far field quantities such as RCS or radiation patterns are of interest. Principal advantages of the wire grid approach are that the geometry is easily specified for computer input, and only one-dimensional integrals need be numerically evaluated in the method of moments. The wire grid modeling approach, however, often proves unsatisfactory where near field quantities such as surface currents or input impedance are desired. One obvious difficulty is in interpreting computed wire currents as equivalent surface currents. Also, however, the storage of energy in the neighborhood of a wire mesh is not completely

equivalent to that of a continuous surface. As a result, computed resonant frequencies and reactive components of computed impedances are often shifted from their correct values.

Most of the difficulties involved in wire grid modeling may be overcome by surface patch modeling, and several such approaches have been developed. One well-tested scheme [2] makes use of the electric field integral equation (EFIE) formulation and a triangular surface patch modeling approach to represent the geometry. There are two principal advantages of this combination:

1. The EFIE formulation, in contrast to the magnetic field integral equation (MFIE), applies to open structures, and it allows voltage and load conditions to be easily specified at terminals defined on the structure.

2. Triangular patches are the simplest planar surfaces which can be used to model arbitrary surfaces and boundaries, and they permit patch densities to be varied locally so as to model a rapidly varying geometry or current distribution.

A disadvantage of the EFIE approach, however, is that the resulting integral equation contains both a singular kernel and derivative operators. These features require that an algorithm based on the EFIE formulation must be developed carefully to ensure that it is both accurate and numerically stable.

In this report, we extend the approach of [2] to develop a procedure for analyzing an arbitrary configuration of conducting wires and bodies. An important feature of the algorithm developed is its ability to handle wire-to-wire, surface-to-surface, and wire-to-surface junctions. Numerous applications requiring these modeling capabilities exist. For example, many practical antennas are formed by attaching some thin wire configuration to a conducting body, and exciting the resulting structure by maintaining a potential difference between the wire and conducting body at the attachment point. Often, the shape or electrical size of the conducting body is such that it cannot be treated as an

8

infinite ground plane. Examples of such structures include automobile radio antennas and wire antennas for shipboard communications. In both applications, the vehicle supporting the antenna has a complicated geometry whose physical dimensions are only on the order of a wavelength at the frequency of operation.

Several approaches to specific wire/body junction problems have been reported in the literature. Bolle and Morganstern [3] numerically solved the classically formulated case of a monopole protruding from a small sphere by considering it to be the limiting case of a conical antenna. Tesche and Neureuther[4] found current distributions on a monopole mounted on a conducting sphere by using the Green's function for the electric field produced by a point source in the presence of the sphere. Tsai [5] solved the problem of a monopole attached to spheres and cylinders based on a Fourier transform solution for the wire and the equivalence principle for the body. Cooper [6] measured current distributions and input impedances of monopoles attached to conducting cylinders. Albertsen et al. [7] determined radiation patterns for wires attached to a circular cylinder modeled by quadrilateral patches. Their formulation was based on the EFIE formulation for wires and the magnetic field integral equation (MFIE) for the cylinder. Shaeffer, Medgyesi-Mitschang and Putnam [8,9,10] have treated wires attached to bodies of revolution and to finite cylindrical bodies. Richmond [11] solved the problem of a monopole antenna mounted at the center of a circular disk by using the piecewise-sinusoidal Galerkin moment method. Marin and Catedra [12] used hybrid moment method/GTD techniques to treat a monopole mounted off-axis on a circular disk.

None of the above procedures treat wires mounted on a surface at an edge or vertex. Such problems seem to require an a priori knowledge of the form of the surface current distribution near the junction. This information usually must be determined by obtaining a Green's function associated with the specific junction configuration. Glisson and Wilton [13,14] determined this distribution for an edge by analyzing a semi-infinite current filament

9

attached to a conducting wedge. The derived distribution was used together with an EFIE formulation to treat a bent rectangular plate with an arbitrarily oriented wire attached to the plate at the bend. Newman and Pozar [15] treated the same problem by a similar procedure, later extending it to treat a wire attached to a plate at or near a knife edge [17] or at a bend [18].

To our knowledge, none of the above authors attempted to treat wires attached to arbitrarily shaped vertices on conducting bodies, presumably because Green's functions for arbitrary vertex geometries are unavailable. Rao [19], however, attempted to treat the arbitrary vertex attachment problem by *numerically* determining the variation of the current near an arbitrary junction at an edge or vertex. However, his approach was found to be ill-conditioned due to a near linear dependency in the basis functions associated with the wire junction and the neighboring surface patches. Costa and Harrington [20,21] closely followed Rao's approach, but eliminated the dependency in the basis functions. They implicitly assumed that for a junction of any geometrical configuration, only a junction basis function with a $1/r$ variation is needed to represent the surface current at the attachment point. They reasoned that basis functions on the surface would account for any angular variation of the junction current. Their approach is appealing because of its simplicity and generality.

In this work, we use the approach of Costa and Harrington—with a modification in the potential computations to increase the numerical efficiency—and apply this procedure to wire-to-surface junctions of arbitrary geometry. The problem of modeling arbitrary wire-to-surface junctions is the least well understood portion of the present analysis, and hence particular emphasis is placed here on validating numerical results from such problems. Unfortunately, bounds on computer resources limit our study to structures whose largest electrical dimensions are only a few wavelengths. Furthermore, very few measurements or computed results involving antennas attached to edges or vertices may be found in the

10

literature, and hence we make use of some indirect methods for validation of the results.

In Chapter 2, the formulation of the electric field integral equation for an arbitrary configuration of wires and conducting bodies is given. Current expansion functions and testing procedures are introduced in Chapter 3 to convert the integral equation into a matrix equation for numerical solution. Numerical results for a wide variety of wire-to-surface junction problems are presented in Chapter 4. Numerical examples are given illustrating the calculation of current distribution, charge density, input impedance, and far field patterns for various junction configurations including wires mounted on smooth surfaces, edges, and vertices. A brief summary of the research reported here is found in Chapter 5. Detailed derivations of the numerical methods used to compute the potential integrals required in the numerical procedure are given in appendices. A computer program, JUNCTION, based on the numerical procedures of this report has been developed and is described in [22].

Chapter 2

Electric Field Integral Equation Formulation

In this chapter the equivalence principle is used together with boundary conditions on conducting bodies and wires to derive the electric field integral equation (EFIE).

2.1 Equivalence Principle

Consider a perfectly conducting body which is placed in a homogenous medium (μ, ϵ) and whose surface is denoted by S with unit normal vector $\hat{n}$. The body is illuminated by an incident or impressed field (E^i, H^i) due to impressed electric and magnetic current sources J^i and M^i, respectively. (The incident field (E^i, H^i) is defined to be that which would exist in space if the body were not present.) The incident field induces a surface current on the conductor and this current in turn radiates scattered fields (E^s, H^s). The total field exterior to the body, (E, H), is a superposition of the incident field and the scattered field (i.e., $E = E^i + E^s$, $H = H^i + H^s$). The induced surface current is related to the surface tangential magnetic field $(J = \hat{n} \times H)$, but is unknown. Our task is to derive an integral equation for the induced surface current. If the integral equation can be solved for this current, all other electromagnetic quantities may be determined from it.

We invoke the equivalence principle [23] to allow the metal conductor to be removed and

12

replaced by a system of currents radiating in free space such that the fields produced are identical to those of the original problem. The steps to generate this equivalent situation are:

1. First the conducting body is removed and the resulting void is filled with the same material as the surrounding medium.

2. On the mathematical surface S previously corresponding to the conducting body, we place an electric surface current J_{eq} and a magnetic surface current M_{eq}. These currents are required to produce the same fields as in the original problem; therefore, they are called *equivalent* currents, and they are the sources of the scattered field (E^s, H^s).

3. The impressed currents as well as the equivalent currents now radiate in an infinite homogeneous medium and the fields produced by these currents can be determined by superposition (or equivalently, by means of potential representations of the fields).

4. We specify the exterior fields to be that of the original problem (so $E_{tan} = 0$ on S). We also specify the field interior to S to be zero.

5. The equivalent magnetic current must support any discontinuity in electric field at S, but since the tangential electric field is zero on both sides of S, the equivalent magnetic current M_{eq} must be zero. Since the interior magnetic field is zero, the equivalent electric current is identical to the *actual* surface current J on the conductor.

The correctness of the equivalent model can be easily verified by checking to see that all the postulated fields satisfy Maxwell's equations, including the jump discontinuity conditions. The above argument permits us to assert that the scattered fields due to currents on

13

conductor surfaces can be computed from potential integrals *as if the currents were in an infinite homogeneous medium.* This fact will be used in the next section.

At this point the surface current J is unknown because we do not know the scattered fields on the exterior of S. Since the equivalent current radiates in an infinite homogeneous medium, however, we may express the scattered fields produced by J in terms of potential integrals, and enforce boundary conditions on S to obtain an equation from which J may be determined.

2.2 Coupled Electric Field Integral Equation

The previous section provides a scheme for determining fields if the induced surface currents are given. The task now is to derive an integral equation for determining the currents.

Let S denote a configuration of perfectly conducting surfaces immersed in an incident electromagnetic field. In general, S may consist of a collection of conducting bodies and wires. The wires may be connected to smooth surfaces, edges, or vertices on the bodies, forming different junction configurations as shown in Fig. 2.1. S is then to be viewed as the union of the bodies and the wires, which can be expressed as follows:

$$S = S_B \cup S_W = \left[\bigcup_{k=1}^{N_b} S_{B^k} \right] \cup \left[\bigcup_{l=1}^{N_w} S_{W^l} \right] \tag{2.1}$$

where N_b and N_w are the number of bodies and the number of wires, respectively. The wire radii may vary but are always assumed to be small compared to the wavelength, thus eliminating the need to consider any circumferential variation or components of wire currents.

An electric field E^i, defined to be the field due to an impressed source in the absence of S, is incident on and induces a surface current J and total current I on S_B and S_W, respectively. A pair of coupled integral equations for the configuration of wires and bodies

14
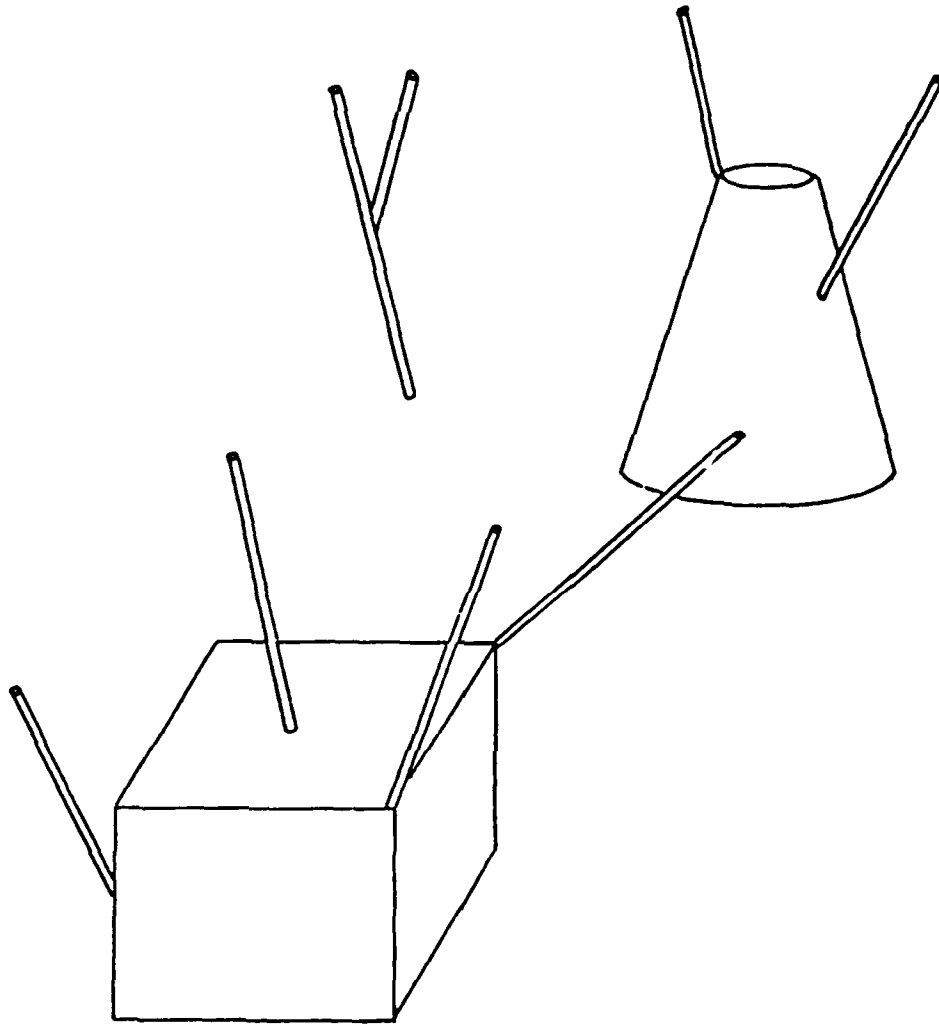
Figure 2.1: Typical wire/surface configuration may consist of a collection of conducting bodies and wires. The wires may be connected to smooth surfaces, edges, or vertices on the bodies, forming different junction configurations.

may be derived by requiring the tangential component of the electric field to vanish on each surface. Thus we have

$$E_{tan}^i = (j\omega A + \nabla\Phi)_{tan}, \quad r \text{ on } S \tag{2.2}$$

where

$$A = \frac{\mu}{4\pi}\left[\int_{S_B} J\frac{e^{-jkR}}{R}dS' + \int_{S_W}\frac{I\hat{\ell}'}{2\pi a(\ell')}\frac{e^{-jkR}}{R}dS'\right], \tag{2.3}$$

$$\Phi = -\frac{1}{j4\pi\omega\epsilon}\left[\int_{S_B}\nabla'\cdot J\frac{e^{-jkR}}{R}dS' + \int_{S_W}\frac{1}{2\pi a(\ell')}\frac{dI}{d\ell'}\frac{e^{-jkR}}{R}dS'\right], \tag{2.4}$$

and $R = |r - r'|$ is the distance between an arbitrarily located observation point r and a source point r' on S. In (2.3) and (2.4), $k = \frac{2\pi}{\lambda}$, where λ is the wavelength, μ and ϵ are the permittivity and permeability, respectively, of the surrounding medium, ℓ' is the arc length along the wire axis, and a is the radius of the wire. Eqs. (2.2)-(2.4) constitute the EFIE for the unknown surface currents J and wire currents I. Because of the thin wire assumption, we further assume that only components of electric field parallel to the wire axis need satisfy (2.2). In the following chapter, the EFIE is approximated by a matrix equation for computer solution.

Chapter 3

Numerical Procedures

In this chapter, a procedure for the numerical solution of the electric field integral equation is developed. Basis functions are chosen to represent the unknown currents, testing functions are chosen to enforce the integral equation, and these are used to derive a matrix approximant to the integral equation.

3.1 Development of Basis Functions

In order to determine the current distribution J, we must first represent it in a form that is convenient for numerical computation. In this section we discuss three sets of basis functions which may be used to represent the current induced on bodies, wires, and in the neighborhood of wire-to-surface junctions. It is required that the basis functions be linearly independent and capable of approximating the actual surface current. A triangular patch model of S_B and a linear tubular segment model of S_W is assumed (c.f. Figs. 3.1 and 3.2). Basis functions suitable for representing currents induced on S_B and S_W are given by

$$\Lambda_n^\gamma(r) = \begin{cases} \dfrac{\rho'^\pm}{h_n^{\gamma\pm}}, & \gamma = B \ \text{or} \ W \ , r \ \text{in} \ S_n^{\gamma\pm} \\ \\ 0 & \text{,otherwise} \end{cases} \tag{3.1}$$

where, as illustrated in Fig. 3.3, $S_n^{\gamma\pm}$, $\gamma = B$ (W), is the $\pm$ reference triangle (segment) attached to the nth non-boundary edge (node) of a body (wire). The height (length)
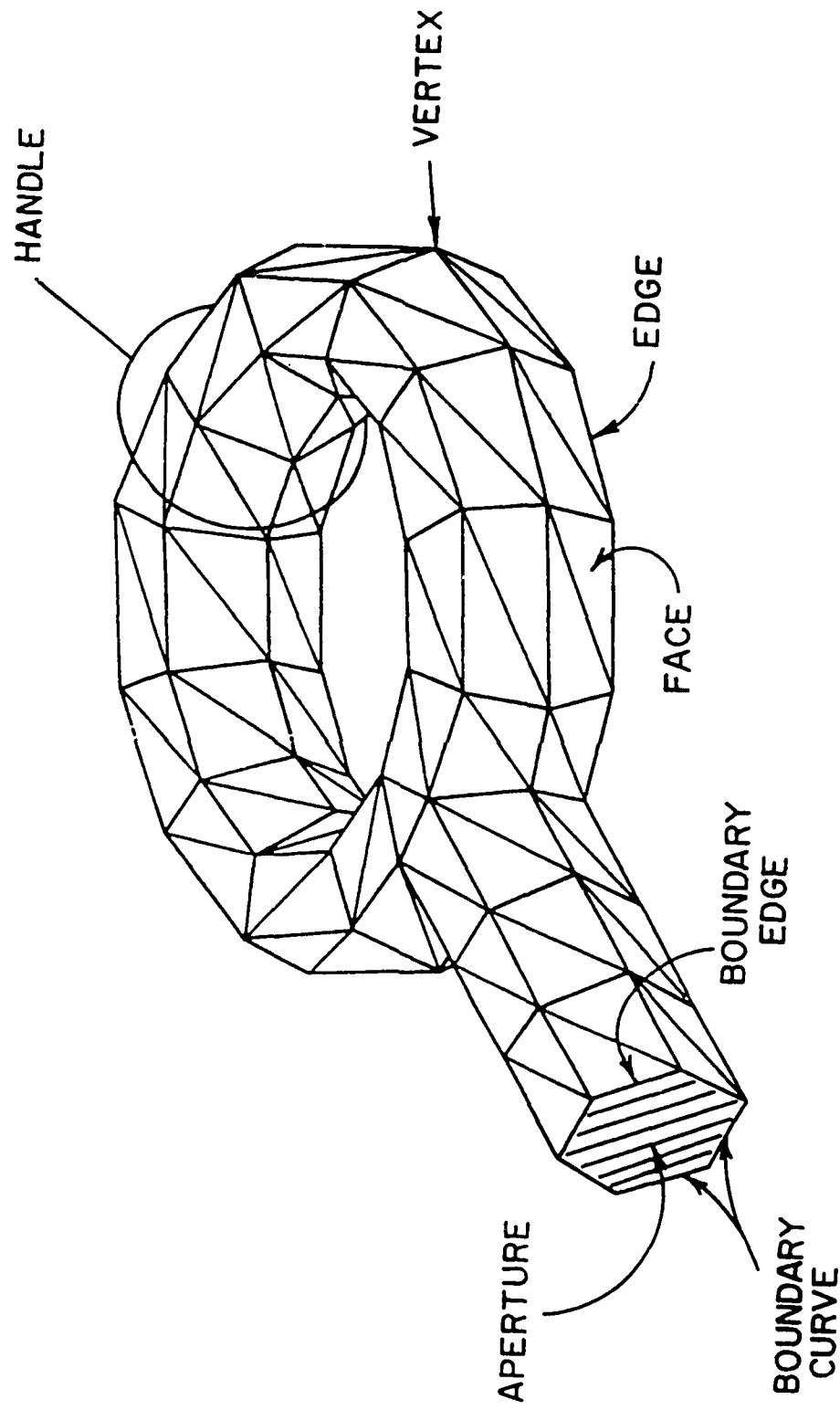
Figure 3.1: Arbitrary surface modeled by triangular patches.
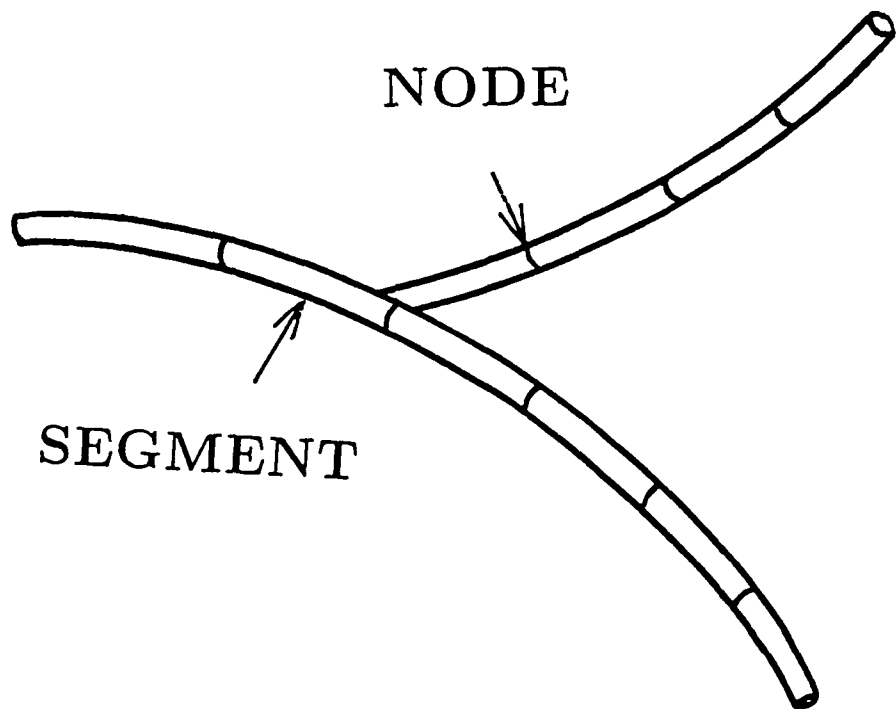
NODE

SEGMENT

Figure 3.2: Arbitrary wire modeled by tubular segments.

of $S_n^{\gamma\pm}$ relative to the nth edge (node) of $S_\gamma, \gamma = B$ (W) is $h_n^{\gamma\pm}$, and $\rho'^{\pm}$ is $(\pm 1)\times$(the vector from the free vertex (node) of $S_n^{\gamma\pm}$ to r). The surface divergence of $\Lambda_n^\gamma(r)$, which is proportional to the linear charge density associated with this basis function, is

$$\nabla_s \cdot \Lambda_n^\gamma(r) = \begin{cases} \pm \dfrac{2}{h_n^{B\pm}}, & \gamma = B \quad, r \text{ in } S_n^{B\pm} \\[2ex] \pm \dfrac{1}{h_n^{W\pm}}, & \gamma = W \quad, r \text{ in } S_n^{W\pm} \\[2ex] 0 & , \text{otherwise}. \end{cases} \tag{3.2}$$

Finally, we define a basis function associated with wire junctions on S_B. A wire-to-surface junction is assumed to exist only at a triangle vertex. Referring to Fig. 3.4, the vector basis function associated with the nth junction is

$$\Lambda_n^J(r) = \begin{cases} K_{nl} \left[1 - \dfrac{(h_{nl}^{J+})^2}{(\rho'^+ \cdot \hat{h}_{nl}^{J+})^2}\right] \Lambda_{nl}^B(r) & , r \text{ in } S_{nl}^{J+} \\[2ex] \Lambda_n^W(r) & , r \text{ in } S_n^{J-} \\[2ex] 0 & , \text{otherwise}, \end{cases} \tag{3.3}$$

where the double index nl refers to the lth triangle, S_{nl}^{J+}, at the nth junction (c.f. Fig. 3.4). $\Lambda_{nl}^B(r)$ and h_{nl}^{J+} are the previously defined body basis function and the vector height, respectively, associated with the edge opposite the junction vertex in S_{nl}^{J+}. The total flux from the junction triangles into the wire is normalized to unity if we choose

$$K_{nl} = \frac{\alpha_{nl}}{\ell_{nl} \displaystyle\sum_{l=1}^{N_{Jn}} \alpha_{nl}} = \frac{\alpha_{nl}}{\ell_{nl}\alpha_n^t}, \tag{3.4}$$

where α_{nl} is the angle between the two edges of S_{nl}^{J+} common to the nth junction vertex, ℓ_{nl} is the length of the edge opposite the junction in S_{nl}^{J+}, and α_n^t is the sum of the nth junction vertex angles. N_{Jn} is the number of patches attached to the nth junction. We list here some of the properties which make this basis function suited for representing the current in the neighborhood of a junction:
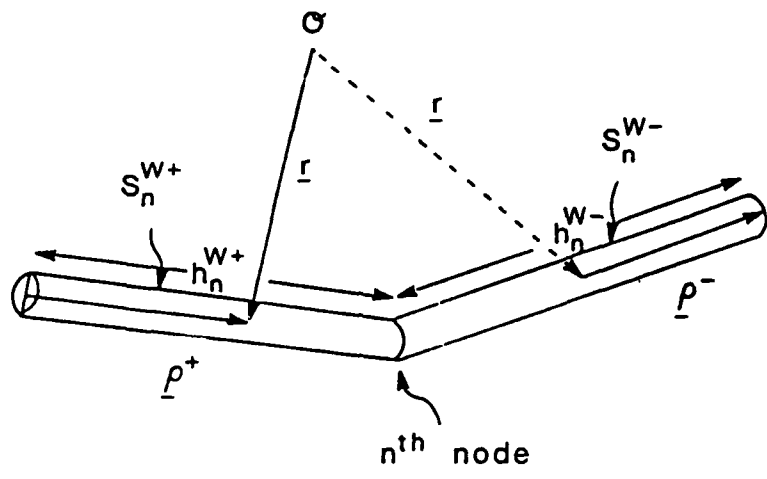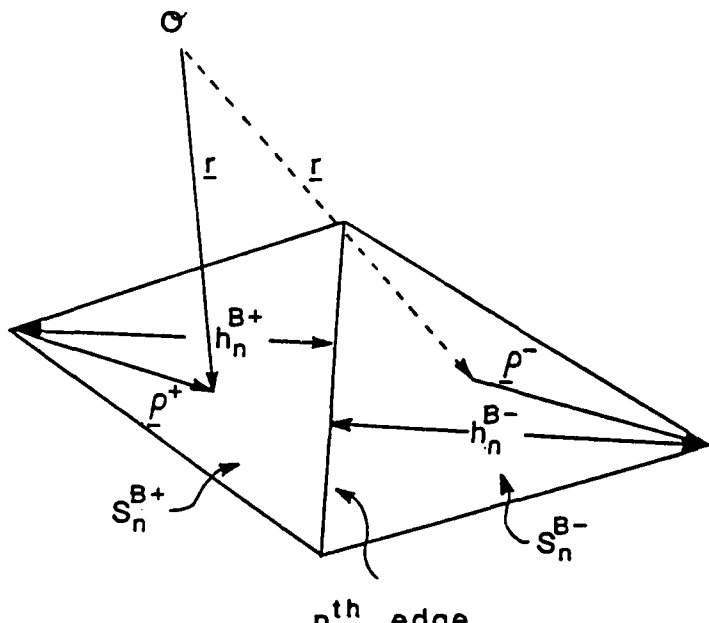
Figure 3.3: (a) Geometrical parameters associated with the nth node of wire. (b) Geometrical parameters associated with the nth edge of body.

21
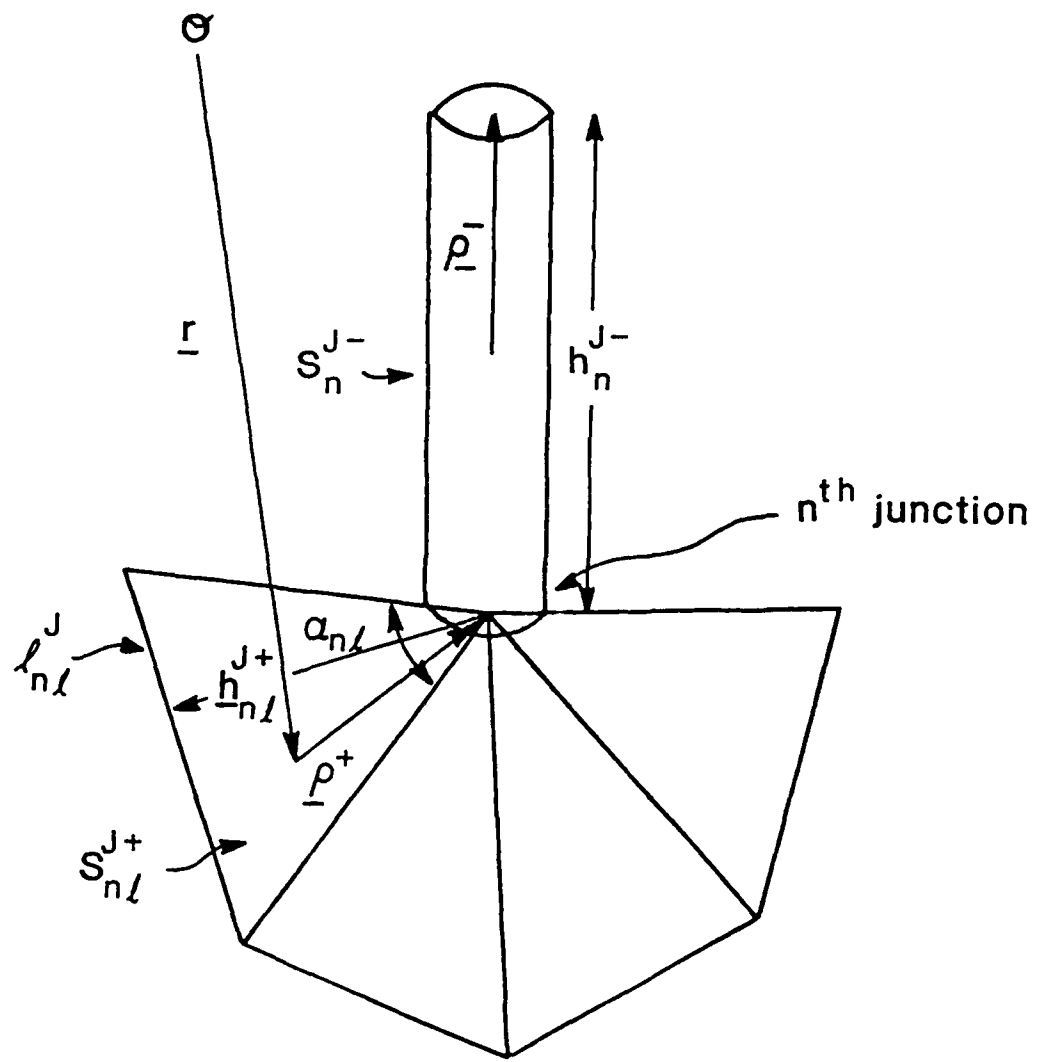
Figure 3.4: Geometrical parameters associated with the nth wire-to-surface junction.

1. The radially directed basis function has a $1/|\rho'|$ magnitude variation in the neighborhood of the junction vertex. It can be shown that the current has this radial variation in the neighborhood of a thin wire junction regardless of the vertex shape. The normalization (3.4) of (3.3) distributes the associated surface current approximately uniformly around the junction regardless of its shape; it can be shown that the surface currents on S_B at the junction are capable of representing any angular variation of the junction current.

2. The function $\Lambda_n^J(\boldsymbol{r})$ vanishes at the edge opposite to the junction vertex; thus no charge is deposited along this edge.

3. The surface divergence of $\Lambda_n^J(\boldsymbol{r})$, which is proportional to the surface charge density, is given by

$$
\nabla_s \cdot \Lambda_n^J(\boldsymbol{r}) = \begin{cases} \dfrac{2K_{nl}}{h_{nl}^{J+}} & ,\boldsymbol{r} \text{ in } S_{nl}^{J+} \\[2mm] -\dfrac{1}{h_n^{J-}} & ,\boldsymbol{r} \text{ in } S_n^{J-} \\[2mm] 0 & ,\text{otherwise.} \end{cases} \tag{3.5}
$$

4. The current flows parallel to the two edges of S_{nl}^{J+} common to the junction vertex. This implies that no line charges are deposited along edges of S_{nl}^{J+}.

The current on the surfaces S_B may now be represented as

$$
\boldsymbol{J}(\boldsymbol{r}) \approx \sum_{n=1}^{N_B} I_n^B \Lambda_n^B(\boldsymbol{r}) + \sum_{n=1}^{N_J} I_n^J \Lambda_n^J(\boldsymbol{r}), \quad \boldsymbol{r} \text{ on } S_B, \tag{3.6}
$$

and the total axial current on the wire may be represented as

$$
I(\boldsymbol{r})\,\hat{\boldsymbol{l}} \approx \sum_{n=1}^{N_W} I_n^W \Lambda_n^W(\boldsymbol{r}) + \sum_{n=1}^{N_J} I_n^J \Lambda_n^J(\boldsymbol{r}), \quad \boldsymbol{r} \text{ on } S_W, \tag{3.7}
$$

where N_β, $\beta = B, W$, or J is the unknown number of bodies, wires, or junctions, respectively. Note that according to (3.2) and (3.5), the surface divergence, and hence the charge, is constant on all body, wire, and junction subdomains.

3.2 Testing Procedure

The next step in applying the method of moments is to select a suitable testing procedure. Referring to Fig. 3.5, we enforce the integral equation on S_B by integrating the vector component of (2.2) parallel to the path from the centroid of S_m^{B+} to the middle of the edge ℓ_m^B and thence to the centroid of S_m^{B-}. Similarly, we enforce the integral equation on S_W by integrating the vector component of (2.2) parallel to the path from the centroid of S_m^{W+} to node m and thence to the centroid of S_m^{W-}. At a junction (c.f. Fig. 3.6), we first integrate the tangential electric field along a path from the centroid of each junction triangle to the junction, and then along the wire axis to the center of the attached wire segment. The resulting equations are then combined into a single equation for the junction by weighting each with the associated triangle vertex angle, and summing the results for each junction patch. For all path integrals, E^i and A are approximated along each portion of the path by their respective values at the centroids. The integral on $\nabla\Phi$ reduces to a difference of scalar potentials at the path endpoints, thus the eliminating the requirement implied in (2.2) that Φ be differentiable. With $\ell_m^{\gamma\pm}$, $\gamma = B, W$, or J, as the vector path segment, we thus have

$$j\omega\left[\, A(r_m^{\gamma+}) \cdot \ell_m^{\gamma+} + A(r_m^{\gamma-}) \cdot \ell_m^{\gamma-}\,\right] + \left[\, \Phi(r_m^{\gamma-}) - \Phi(r_m^{\gamma+})\,\right]$$

$$= \left[\, E^i(r_m^{\gamma+}) \cdot \ell_m^{\gamma+} + E^i(r_m^{\gamma-}) \cdot \ell_m^{\gamma-}\,\right], \tag{3.8}$$

$$m = 1, 2, \ldots, N_\gamma, \quad \gamma = B \text{ or } W,$$

and

$$\frac{1}{\alpha_m^t} \sum_{l=1}^{N_{Jm}} \alpha_{ml} \left[j\omega A(r_{ml}^{J+}) \cdot \ell_{ml}^{J+} - \Phi(r_{ml}^{J+}) \right] + j\omega A(r_m^{J-}) \cdot \ell_m^{J-} + \Phi(r_m^{J-})$$

$$= \frac{1}{\alpha_m^t} \sum_{l=1}^{N_{Jm}} \alpha_{ml} E^i(r_{ml}^{J+}) \cdot \ell_{ml}^{J+} + E^i(r_m^{J-}) \cdot \ell_m^{J-}, \tag{3.9}$$
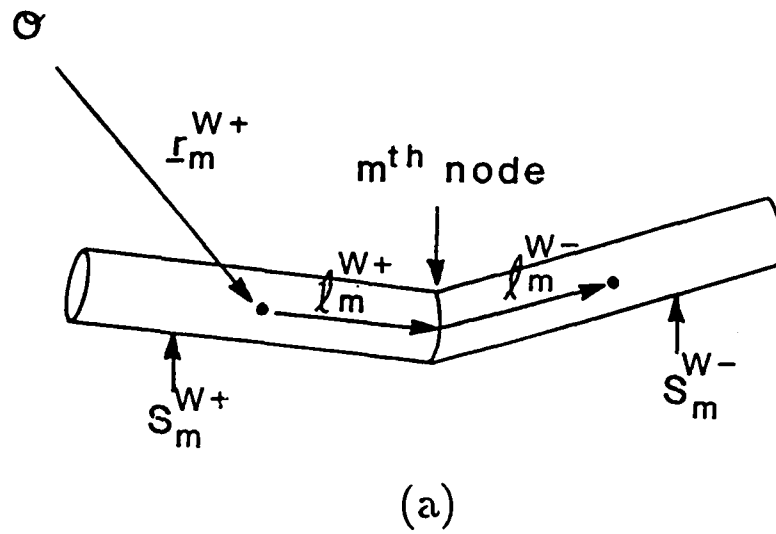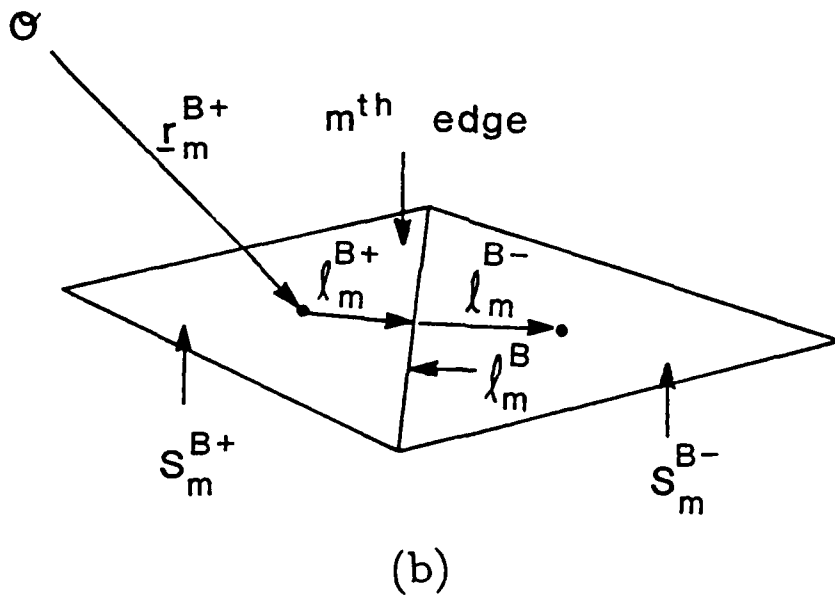
Figure 3.5: (a) Testing path associated with the mth node of wire. (b) Testing path associated with the mth edge of body.
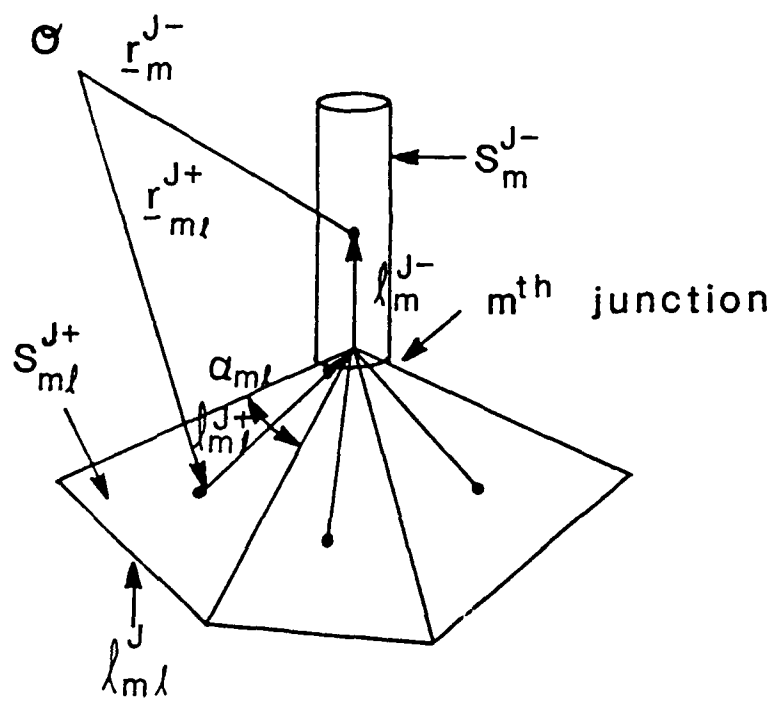
Figure 3.6: Testing paths associated with the mth wire-to-surface junction.

$$m = 1, 2, \ldots, N_J.$$

Using the source expansion defined in (3.6) and (3.7), we obtain from (3.8) and (3.9) a set of linear equations whose solution yields the unknown current coefficients.

3.3 Evaluation of Matrix Elements

Substituting the current representations (3.6) and (3.7) into (3.8) and (3.9), we obtain an $N \times N$ system of linear equations, where $N = N_B + N_W + N_J$, which may be written in matrix form as

$$\begin{bmatrix} [Z^{BB}] & [Z^{BW}] & [Z^{BJ}] \\ [Z^{WB}] & [Z^{WW}] & [Z^{WJ}] \\ [Z^{JB}] & [Z^{JW}] & [Z^{JJ}] \end{bmatrix} \begin{bmatrix} [I^B] \\ [I^W] \\ [I^J] \end{bmatrix} = \begin{bmatrix} [V^B] \\ [V^W] \\ [V^J] \end{bmatrix} \tag{3.10}$$

where the elements of the submatrices are given by

$$Z_{mn}^{\gamma\beta} = j\omega \left[A_{mn}^{\gamma\beta+} \cdot \boldsymbol{\ell}_m^+ + A_{mn}^{\gamma\beta-} \cdot \boldsymbol{\ell}_m^- \right] + \left[\Phi_{mn}^{\gamma\beta-} - \Phi_{mn}^{\gamma\beta+} \right], \quad \gamma \neq J, \tag{3.11}$$

$$Z_{mn}^{J\beta} = \frac{1}{\alpha_m^t} \sum_{l=1}^{N_{Jm}} \alpha_{ml} \left(j\omega A_{mln}^{J\beta+} \cdot \boldsymbol{\ell}_{ml}^{J+} - \Phi_{mln}^{J\beta+} \right) + j\omega A_{mn}^{J\beta-} \cdot \boldsymbol{\ell}_m^{J-} + \Phi_{mn}^{J\beta-}, \tag{3.12}$$

$$A_{mn}^{\gamma\beta\pm} = A_n^\beta(r_m^{\gamma\pm}), \quad \Phi_{mn}^{\gamma\beta\pm} = \Phi_n^\beta(r_m^{\gamma\pm}),$$

$$A_{mln}^{J\beta+} = A_n^\beta(r_{ml}^{J+}), \quad \Phi_{mln}^{J\beta+} = \Phi_n^\beta(r_{ml}^{J+}), \tag{3.13}$$

$$A_n^\beta(r) = \frac{\mu}{4\pi} \int_{S_\beta} \Lambda_n^\beta(r') \frac{e^{-jkR}}{R} dS' \tag{3.14}$$

$$\Phi_n^\beta(r) = -\frac{1}{j4\pi\omega\epsilon} \int_{S_\beta} \nabla_s \cdot \Lambda_n^\beta(r') \frac{e^{-jkR}}{R} dS' \tag{3.15}$$

27

$$\gamma = B, W, \text{ or } J \qquad \beta = B, W, \text{ or } J \tag{3.16}$$

and

$$V_m^\gamma = \left[E^i(r_m^{\gamma+}) \cdot \boldsymbol{\ell}_m^{\gamma+} + E^i(r_m^{\gamma-}) \cdot \boldsymbol{\ell}_m^{\gamma-} \right] \quad \gamma \neq J, \tag{3.17}$$

$$V_m^J = \frac{1}{\alpha_m^i} \sum_{l=1}^{N_{Jm}} \alpha_{ml} E^i(r_{ml}^{J+}) \cdot \boldsymbol{\ell}_{ml}^{J+} + E^i(r_m^{J-}) \cdot \boldsymbol{\ell}_m^{\gamma-}. \tag{3.18}$$

For plane wave scattering problems, for example, we may set (c.f. Fig. 3.7)

$$E^i(r) = (E_\theta^i \hat{\theta}^i + E_\phi^i \hat{\phi}^i) e^{j\mathbf{k} \cdot \mathbf{r}} \tag{3.19}$$

where the propagation vector $\mathbf{k}$ is

$$\mathbf{k} = k(\sin \theta^i \cos \phi^i \hat{x} + \sin \theta^i \sin \phi^i \hat{y} + \cos \theta^i \hat{z}) \tag{3.20}$$

and $(\hat{\theta}^i, \hat{\phi}^i)$ define the angle of arrival in the usual spherical coordinate convention, and can be expressed as

$$\hat{\theta}^i = \cos \theta^i \cos \phi^i \hat{x} + \cos \theta^i \sin \phi^i \hat{y} - \sin \theta^i \hat{z}$$

$$\hat{\phi}^i = -\sin \phi^i \hat{x} + \cos \phi^i \hat{y}.$$

For antenna radiation problems $E_\theta^i = E_\phi^i = 0$, in this case the wire segments attached to node (junction) m may be thought of as separated by a gap across which the voltage V_m^W (V_m^J) is specified.

Solution of the linear system of equations (3.10) yields the set of unknown current coefficients used in the representation of the surface, wire, and junction currents, (3.6) and (3.7). Once the surface current is known, the scattered field or any other electromagnetic quantity of interest may be readily determined.
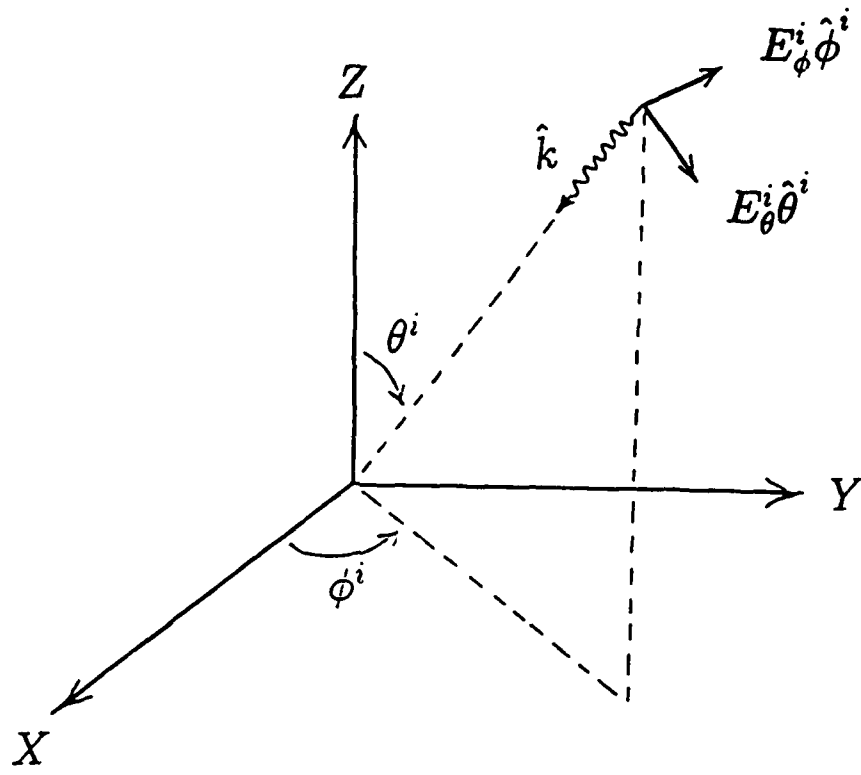
Figure 3.7: Incident field geometrical parameters.

Chapter 4

Numerical Results

In this chapter numerical results such as the surface current near a junction or the input impedance of a monopole or far field pattern are presented for different junction configurations. The geometries considered include wires attached to a smooth surface, an edge, and a vertex.

4.1 Calculation of Current and Charge Distributions

Fig. 4.1 illustrates the current distribution near the junction between a circular cone and a monopole attached at the vertex and inclined at an angle of 60° to the axis. The length of the monopole, the height of the cone, and the diameter of the cone base are all $a = 0.333\lambda$. The radius of the monopole is $r = 0.001a$. The result is compared with the magnetostatic current distribution on an infinite cone with a semi-infinite filamentary current attached to its vertex [24]. The current filament is also inclined at an angle of 60° to the cone axis. Since the magnetostatic result gives the shape but not the magnitude of the current distribution, a complex normalizing constant is chosen so that the magnetostatic current interpolates the dynamic result at one point. Also shown is the uniform distribution that would result from taking the current in the wire and distributing it uniformly about the cone.

Fig. 4.2 illustrates similar quantities near the junction of a circular disk and a monopole attached at the center and inclined at an angle of 30° to the disk axis. The length of the monopole, and the radius of the disk are $a = 0.333\lambda$. The radius of the monopole is $r = 0.001a$.

Figs. 4.3 and 4.4 show the computed current distributions on a circular cylinder with monopoles attached to the center of each endcap and driven at the attachment point. Measured results by Cooper [6] are shown for comparison. The diameter and the height of the cylinder are 0.25λ. The wire radius is 0.007λ and the lengths are 0.125λ and 0.25λ in the two figures, respectively. Similar results are shown in Fig. 4.5 for a cylinder whose diameter and height are 0.5λ with a wire length of 0.125λ. Charge distributions corresponding to these three cases are shown in Figs. 4.6, 4.7 and 4.8.

4.2 Calculation of Input Impedance

4.2.1 Wire mounted on a smooth surface

Fig. 4.9 shows the input admittance as a function of frequency for an monopole attached to the center of a flat plate and fed at the attachment point. The length of the monopole is 0.421 m, its radius is 0.0008 m, and it is oriented normal to the 0.914 m square plate. The results are compared with those calculated and measured by Newman and Pozar [15].

In Fig. 4.10 is shown the input impedance of a monopole of length $h = d$ and radius $a = 0.0165d$ mounted on a sphere of radius d as a function of the frequency. The results are compared with calculations by Bolle and Morganstern [3], [4].

In Fig. 4.11 is illustrated the input impedance versus frequency of a monopole inclined at an angle of 60° from normal and attached off-axis on a circular disk. The results are compared with measurements by Marin and Catedra[12]. The agreement is very good except for the reactance at the highest frequency measured.

Fig. 4.12 illustrates the input admittance of a monopole mounted near the corner of a box on an infinite ground plane. The box is a 100 mm cube and the monopole length is 60 mm with a radius of 0.8 mm. The measured results of [25] on a ground plane of 780 mm × 780 mm are also shown in the figure. Also shown are results computed by replacing the monopole with an equivalent tape model and then modeling the structure as in [2].
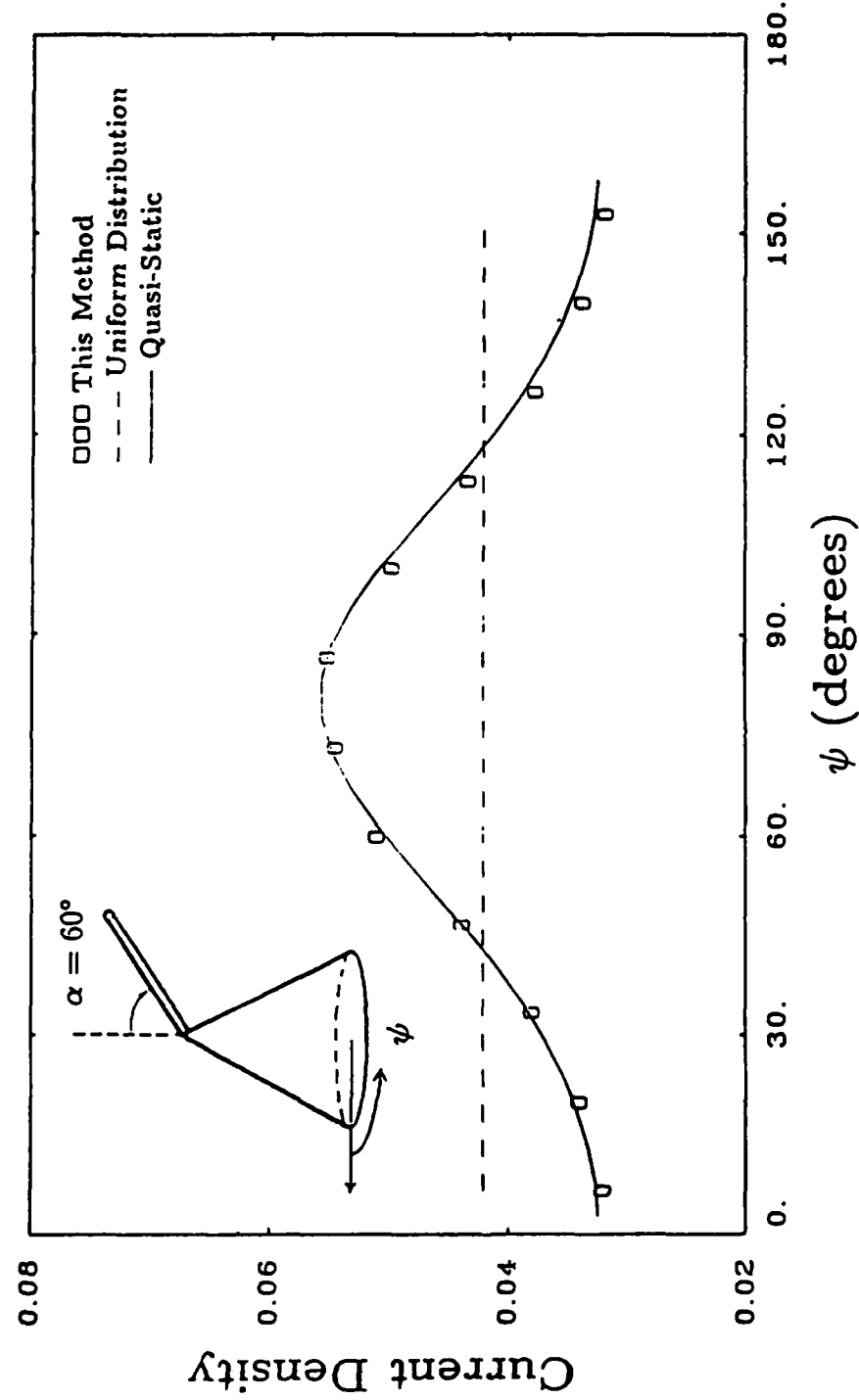
Figure 4.1: Current distribution near the junction of a circular cone and a monopole attached at the vertex and inclined at an angle of 60° to the axis. The length of the monopole, the height of the cone and the diameter of the cone base are all $a = 0.333\lambda$. The radius of the monopole is $r = 0.001a$.
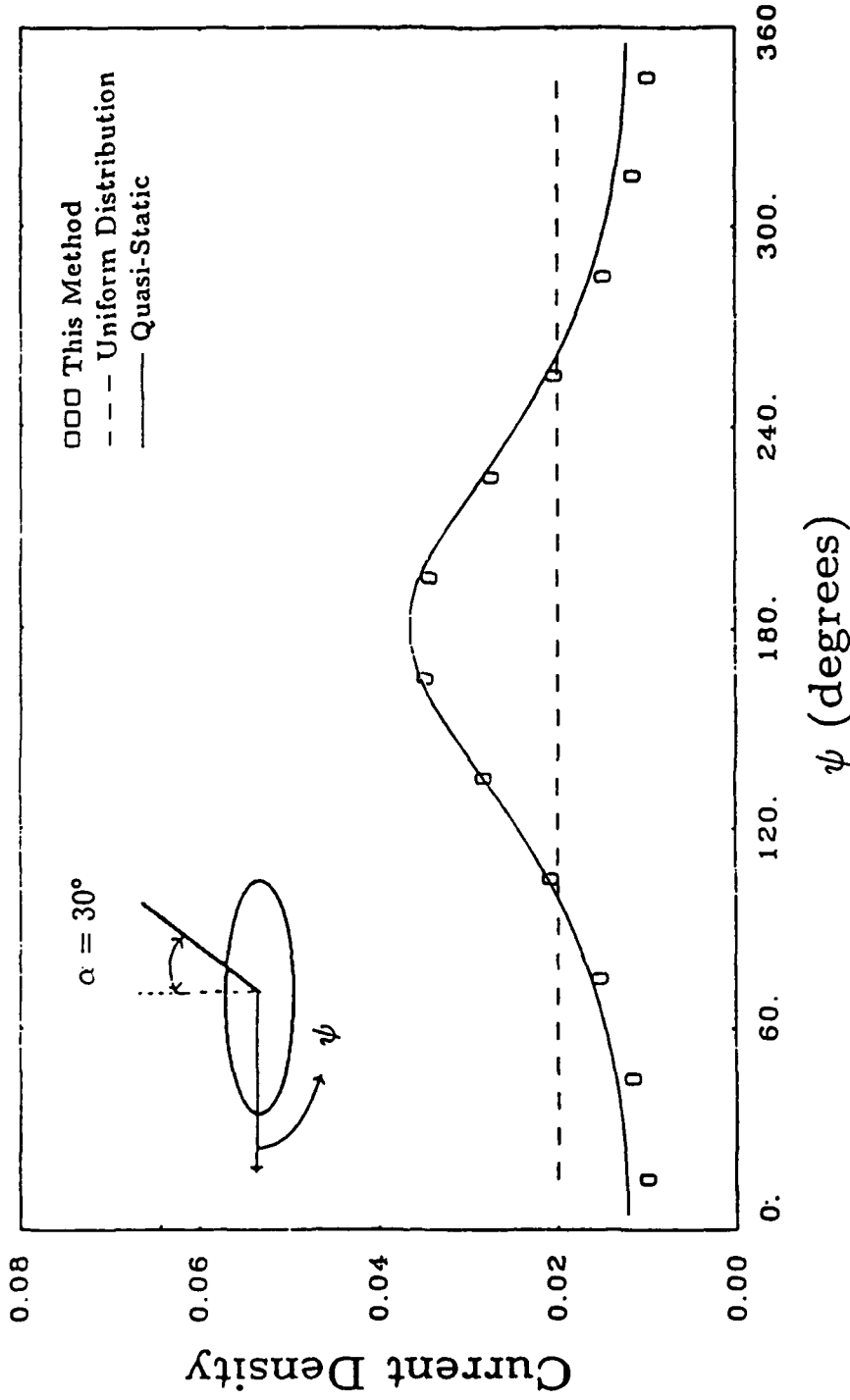
Figure 4.2: Current distribution near the junction of a circular disk and a monopole attached at the center and inclined at an angle of 30° to the axis. The length of the monopole, the radius of the disk are a = 0.333λ. The radius of the monopole is r = 0.001a.

34
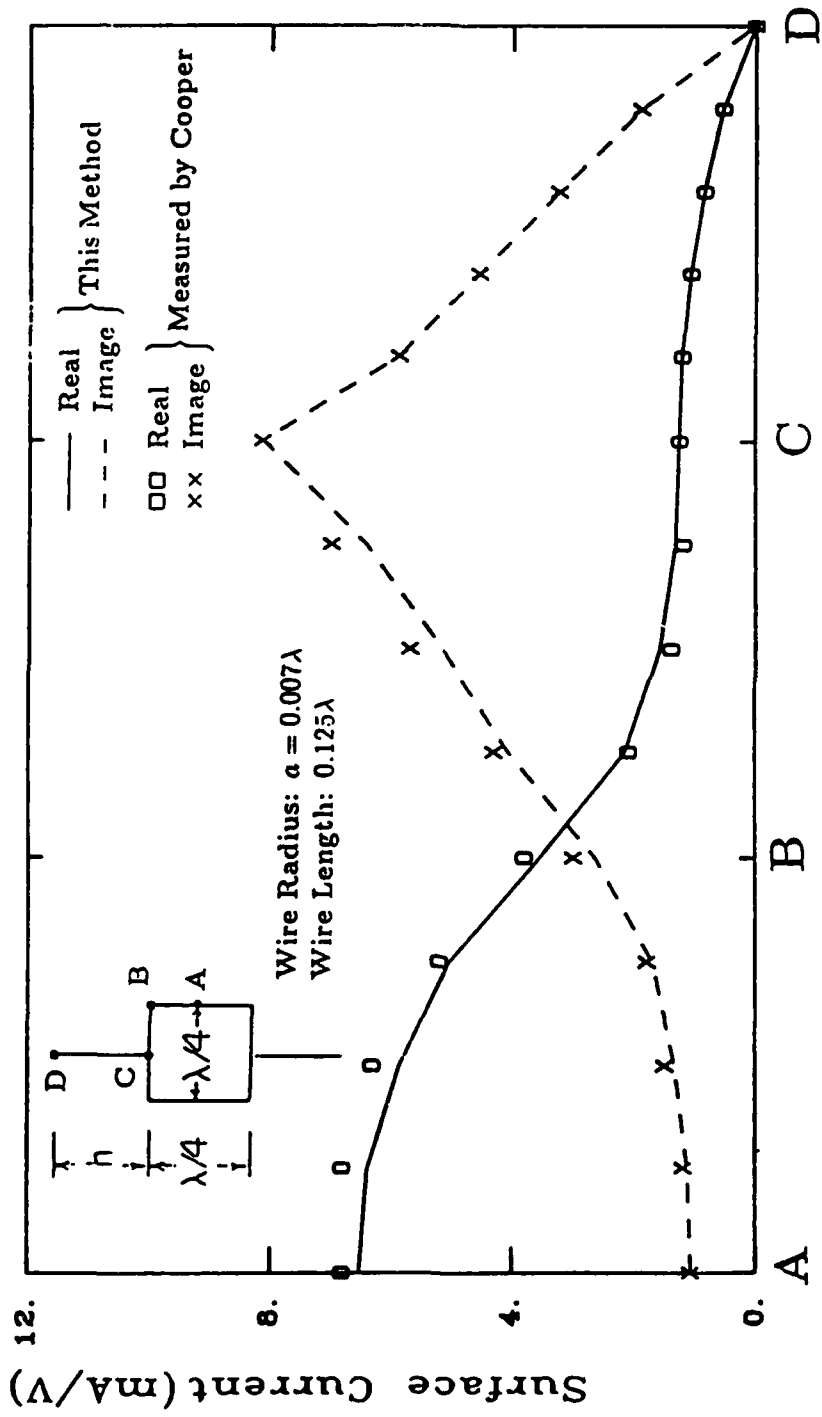
Figure 4.3: Current distribution for a dipole whose arms are attached at the center of the endcaps of a circular cylinder. The wire radius and length are 0.007λ and 0.125λ, respectively.
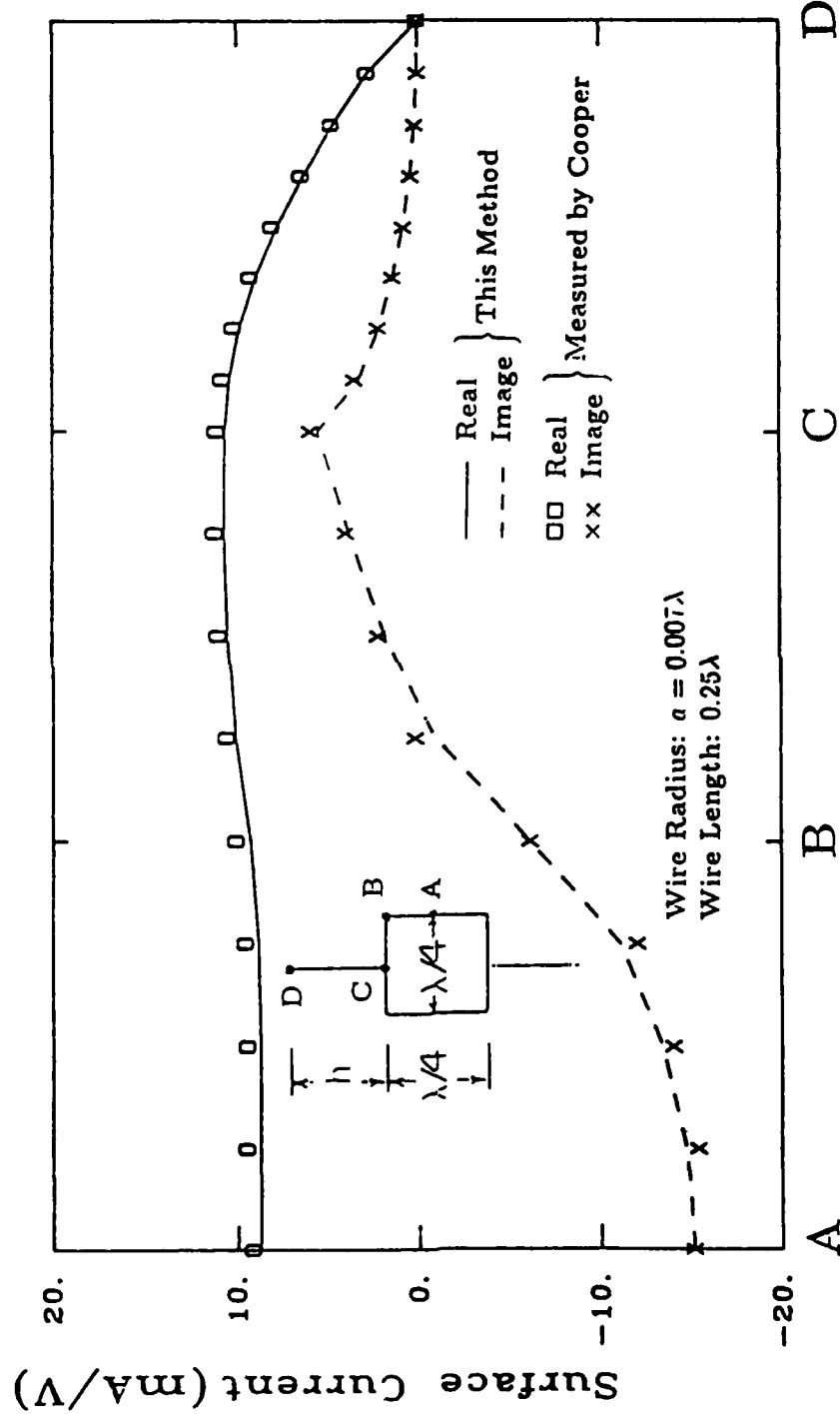
Figure 4.4: Current distribution for a dipole whose arms are attached at the center of the endcaps of a circular cylinder. The wire radius and length are 0.007λ and 0.25λ, respectively.
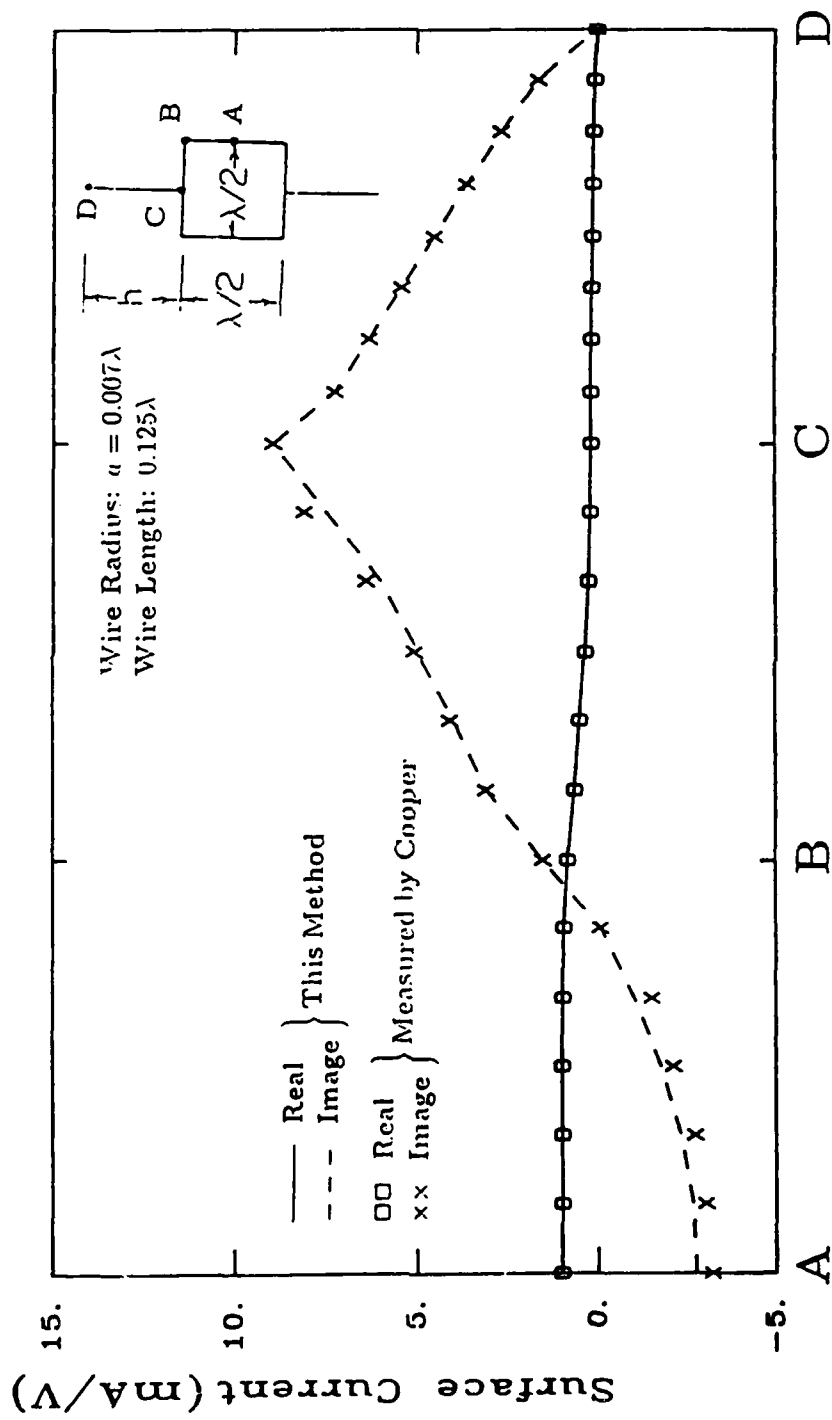
Figure 4.5: Current distribution for a dipole whose arms are attached at the center of the endcaps of a circular cylinder. The wire radius and length are 0.007λ and 0.125λ, respectively.

37
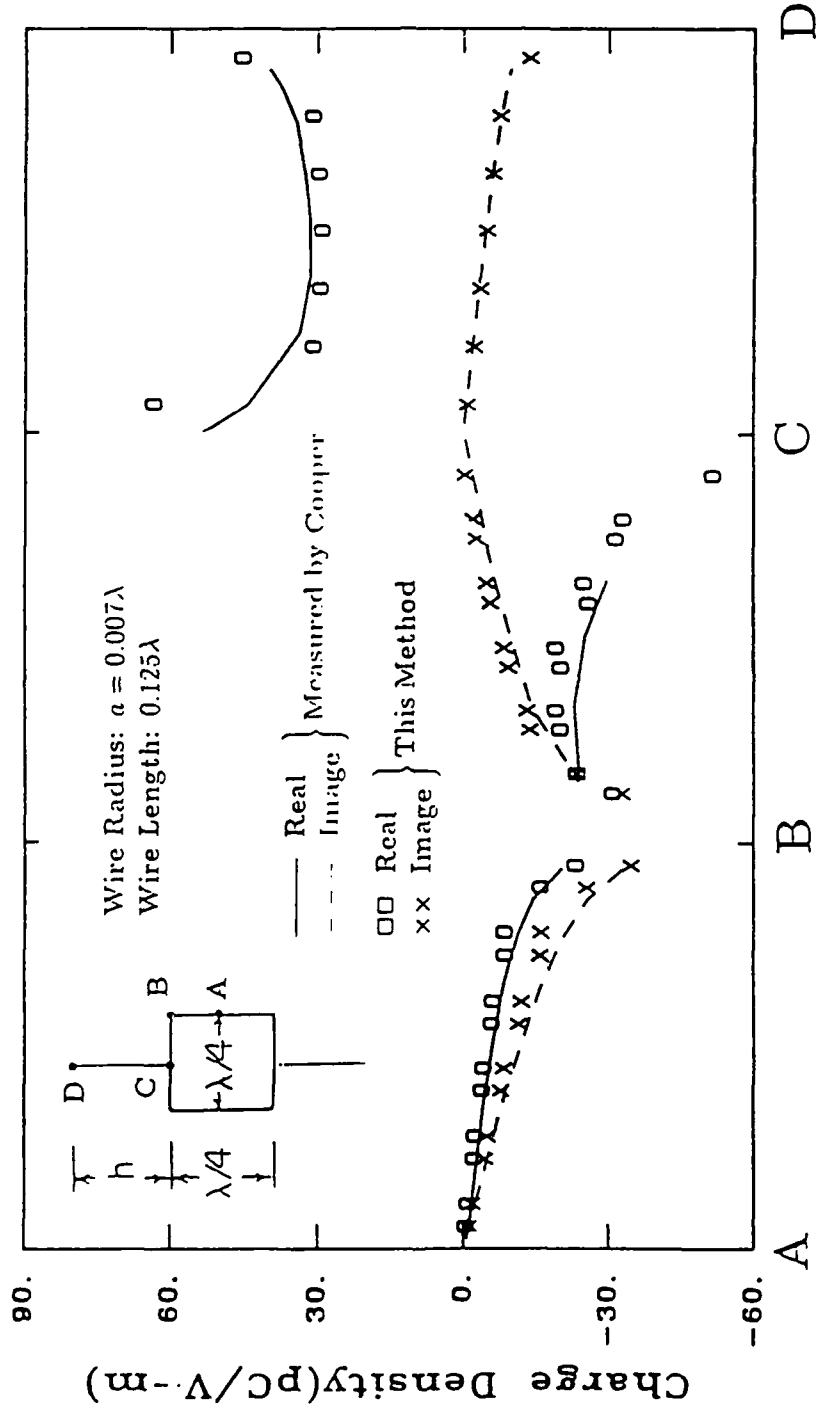
Figure 4.6: Charge distribution for a dipole whose arms are attached at the center of the endcaps of a circular cylinder. The wire radius and length are 0.007λ and 0.125λ, respectively.

38
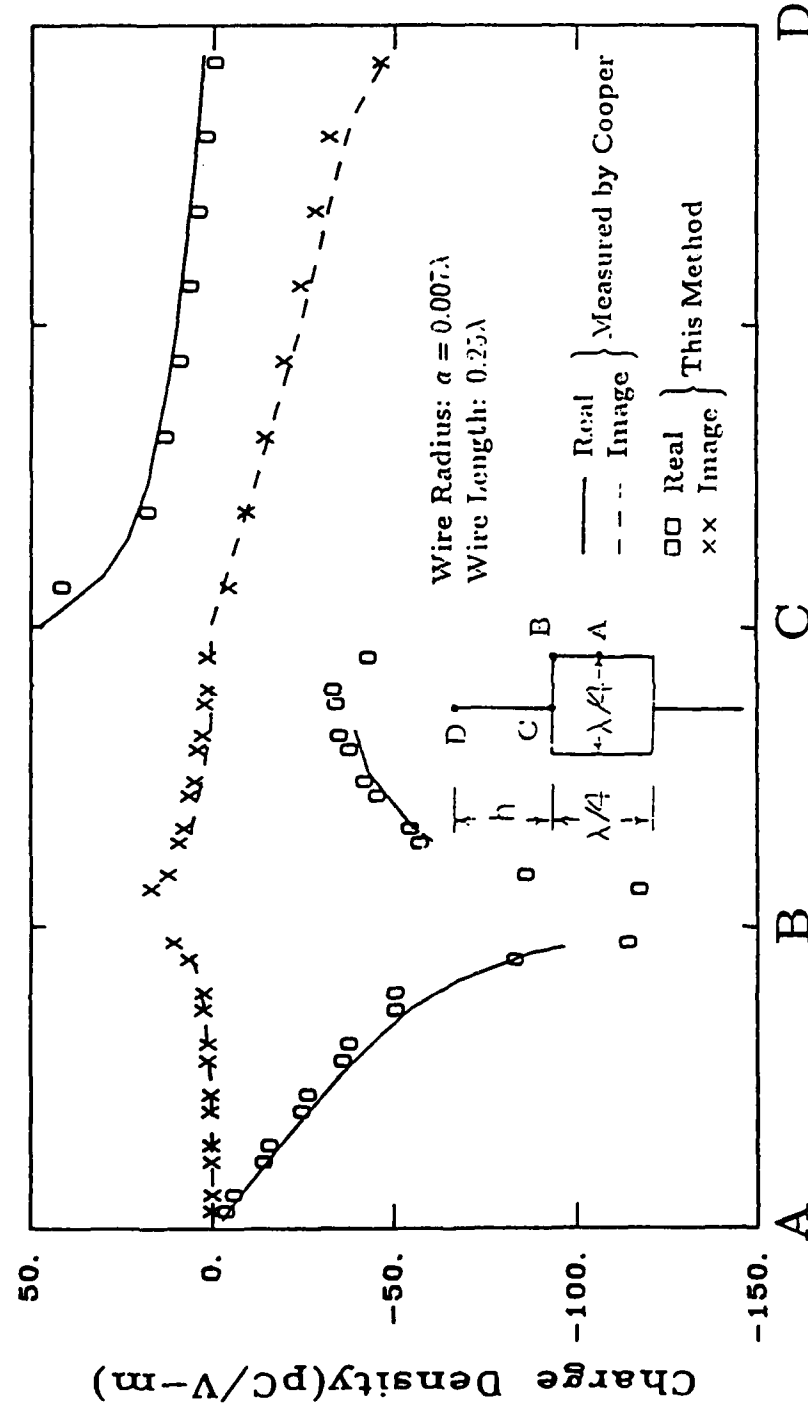
Figure 4.7: Charge distribution for a dipole whose arms are attached at the center of the endcaps of a circular cylinder. The wire radius and length are 0.007λ and 0.25λ, respectively.

39
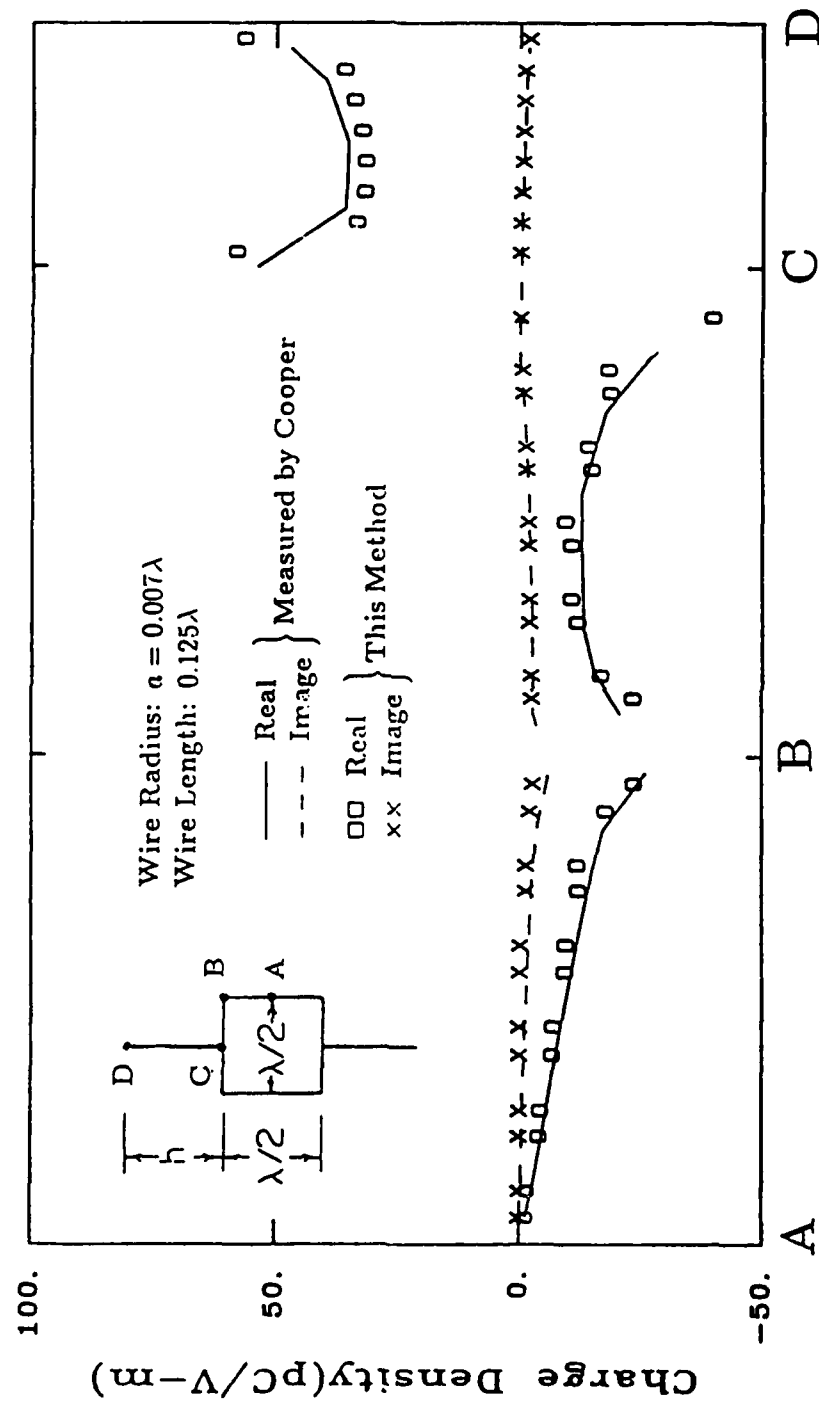
Figure 4.8: Charge distribution for a dipole whose arms are attached at the center of the endcaps of a circular cylinder. The wire radius and length are 0.007λ and 0.125λ, respectively.

40
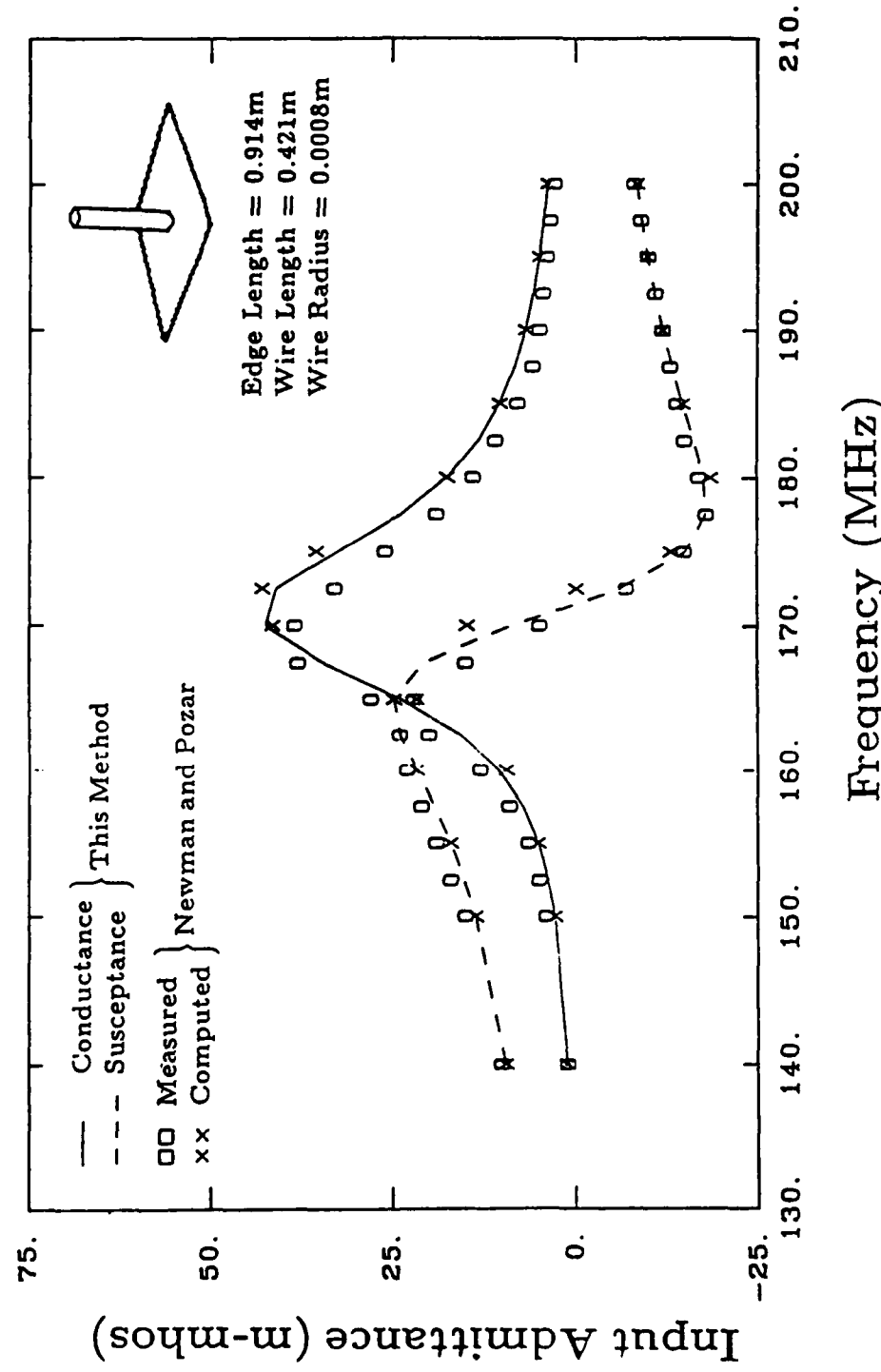
Figure 4.9: Input admittance as a function of frequency for an monopole attached to the center of a flat plate and fed at the attachment point. The length of the monopole is 0.421m, its radius is 0.0008 m, and it is oriented normal to the 0.914 m square plate.
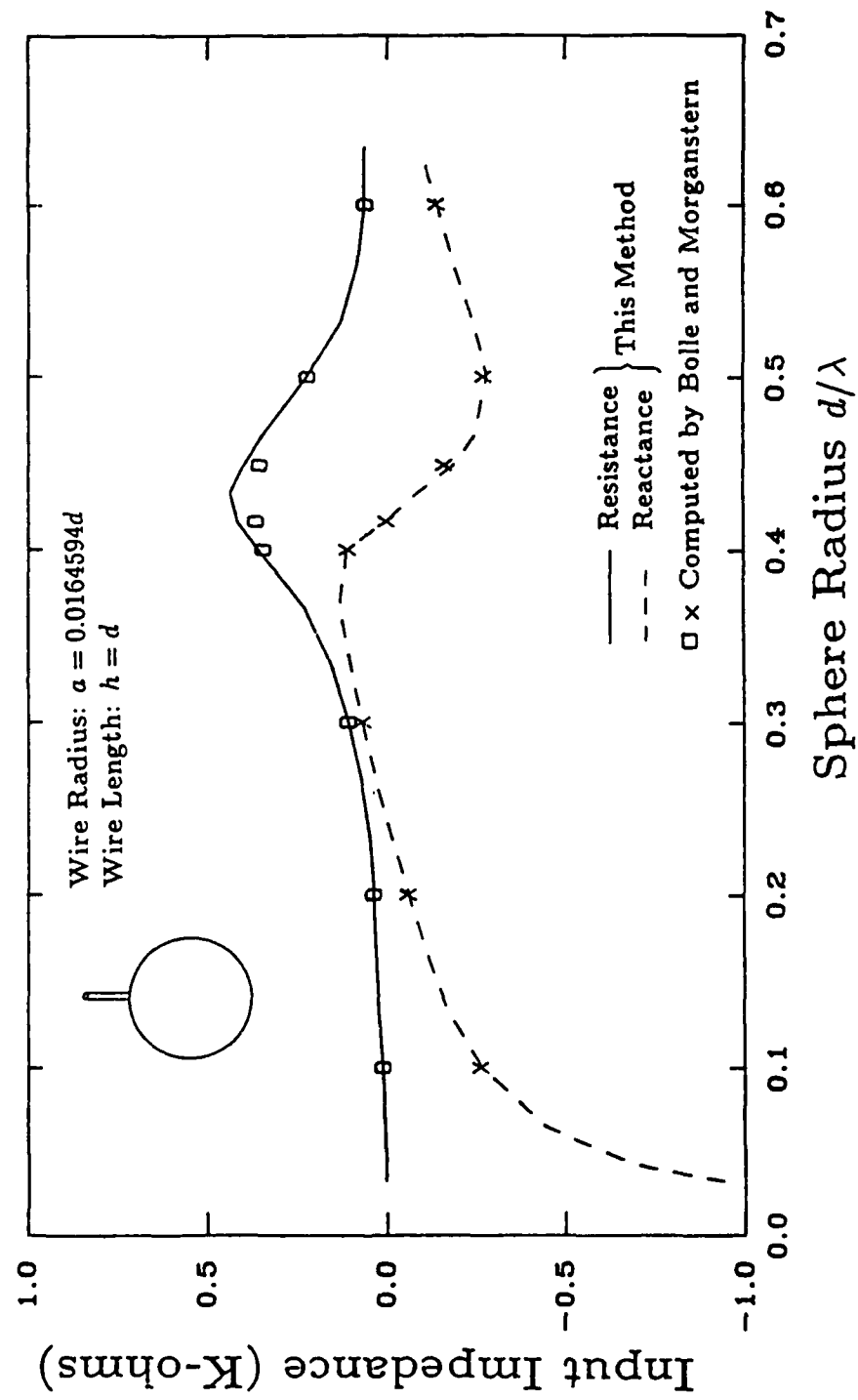
Figure 4.10: Input impedance of a monopole of length $h = d$ and radius $a = 0.0165d$ mounted on a sphere of radius d as a function of the frequency.

42
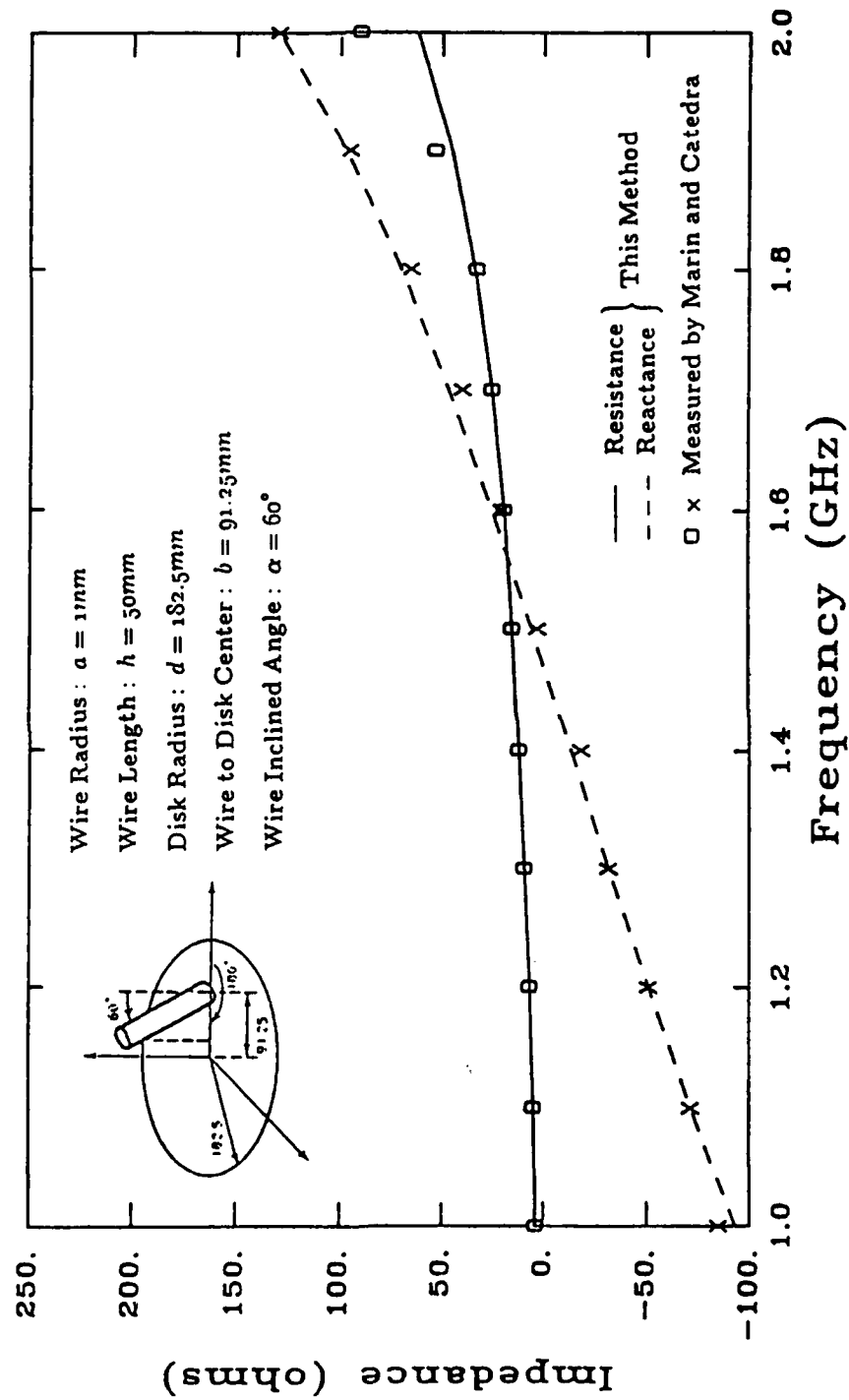
Figure 4.11: Input impedance versus frequency of a monopole inclined 60 degrees and attached off-axis on a circular disk.
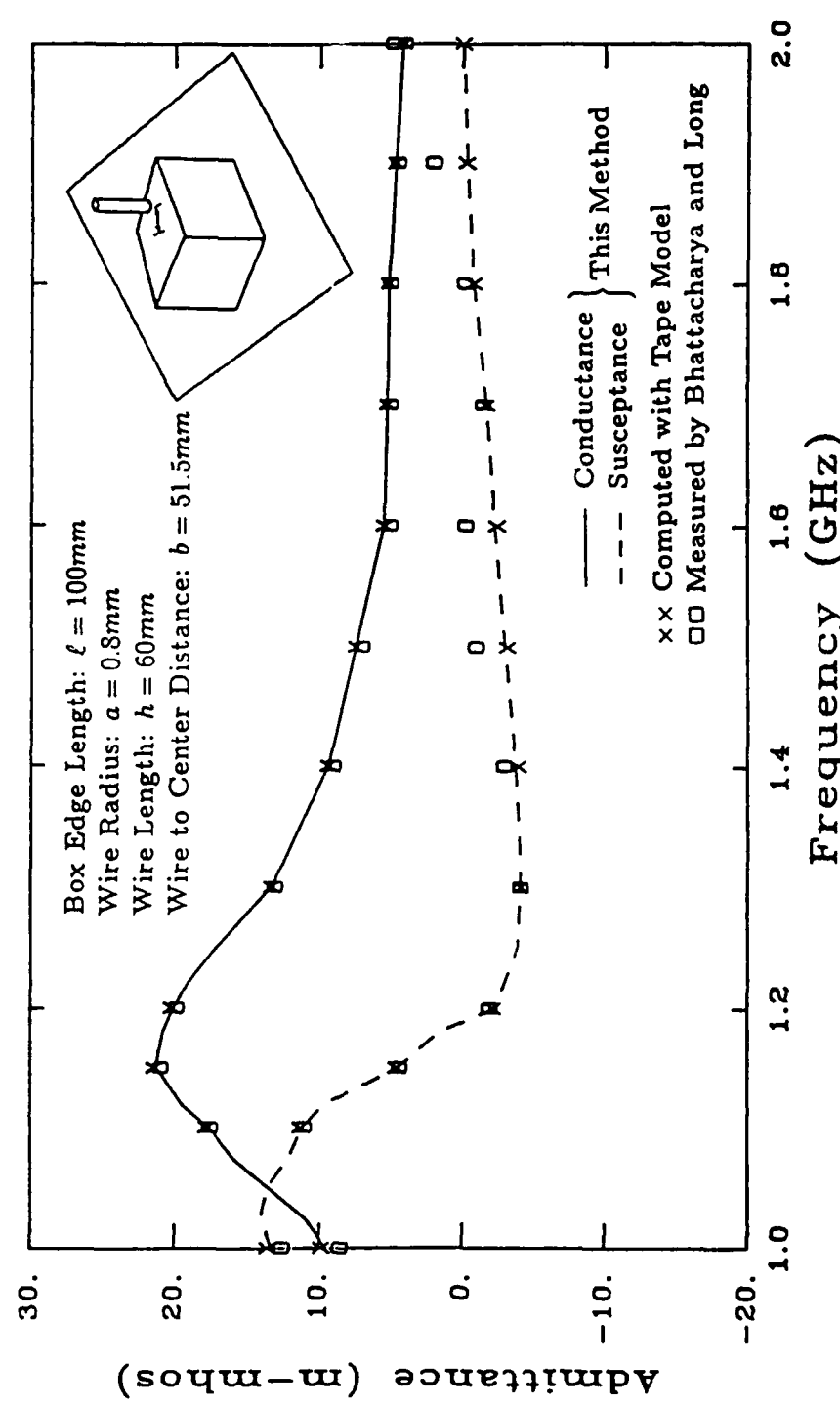
Figure 4.12: Input admittance of a monopole mounted near the corner of a box on a ground plane. The box is a 100 mm cube and the monopole length and radius are 60 mm and 0.8 mm, respectively.

44
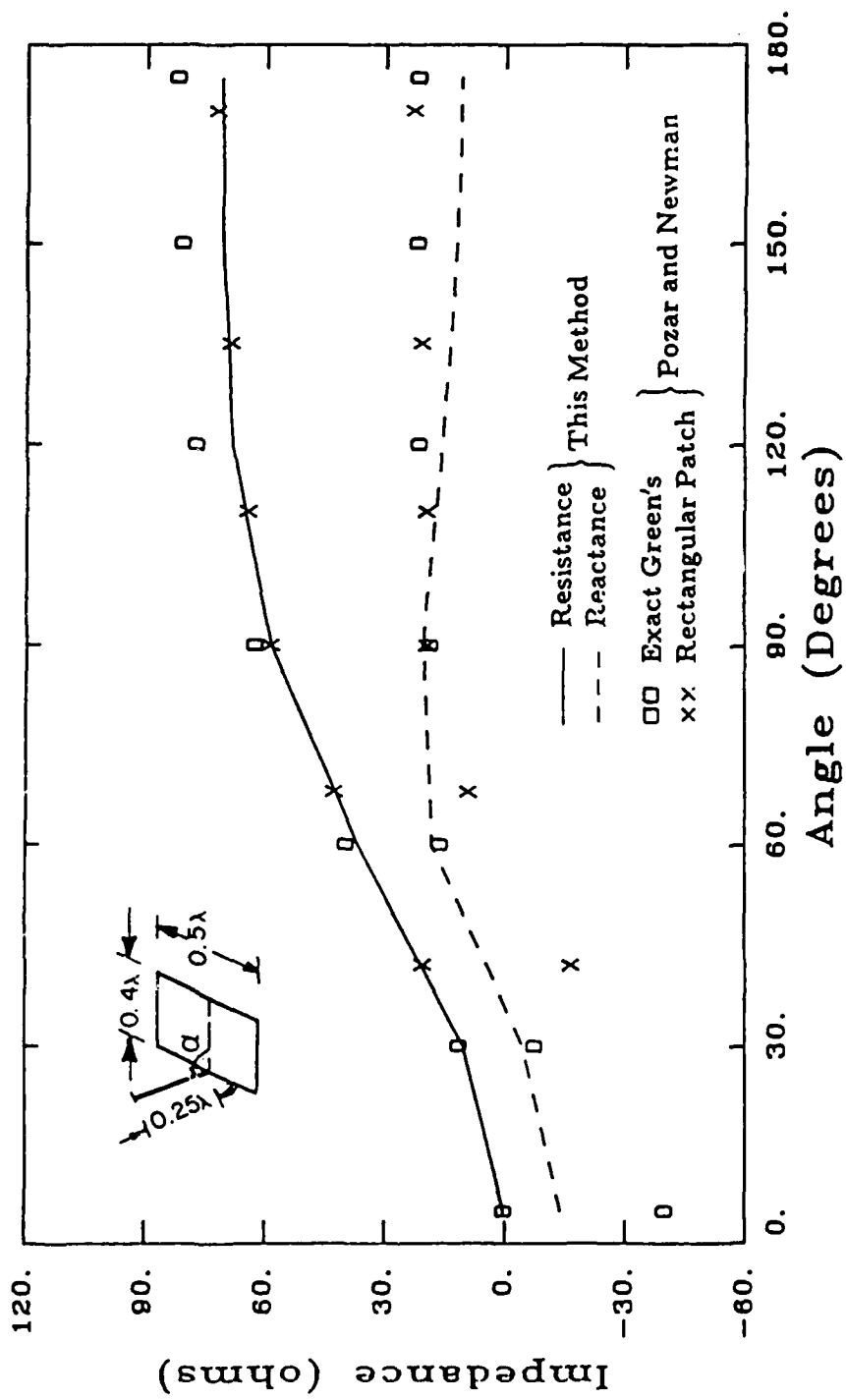
Figure 4.13: Input admittance compared to [18] for monopole attached to plate edge and fed at attachment point. Monopole length and radius are 0.25λ and 0.001λ, respectively, and it is mounted at center of longer edge of rectangular plate.

45
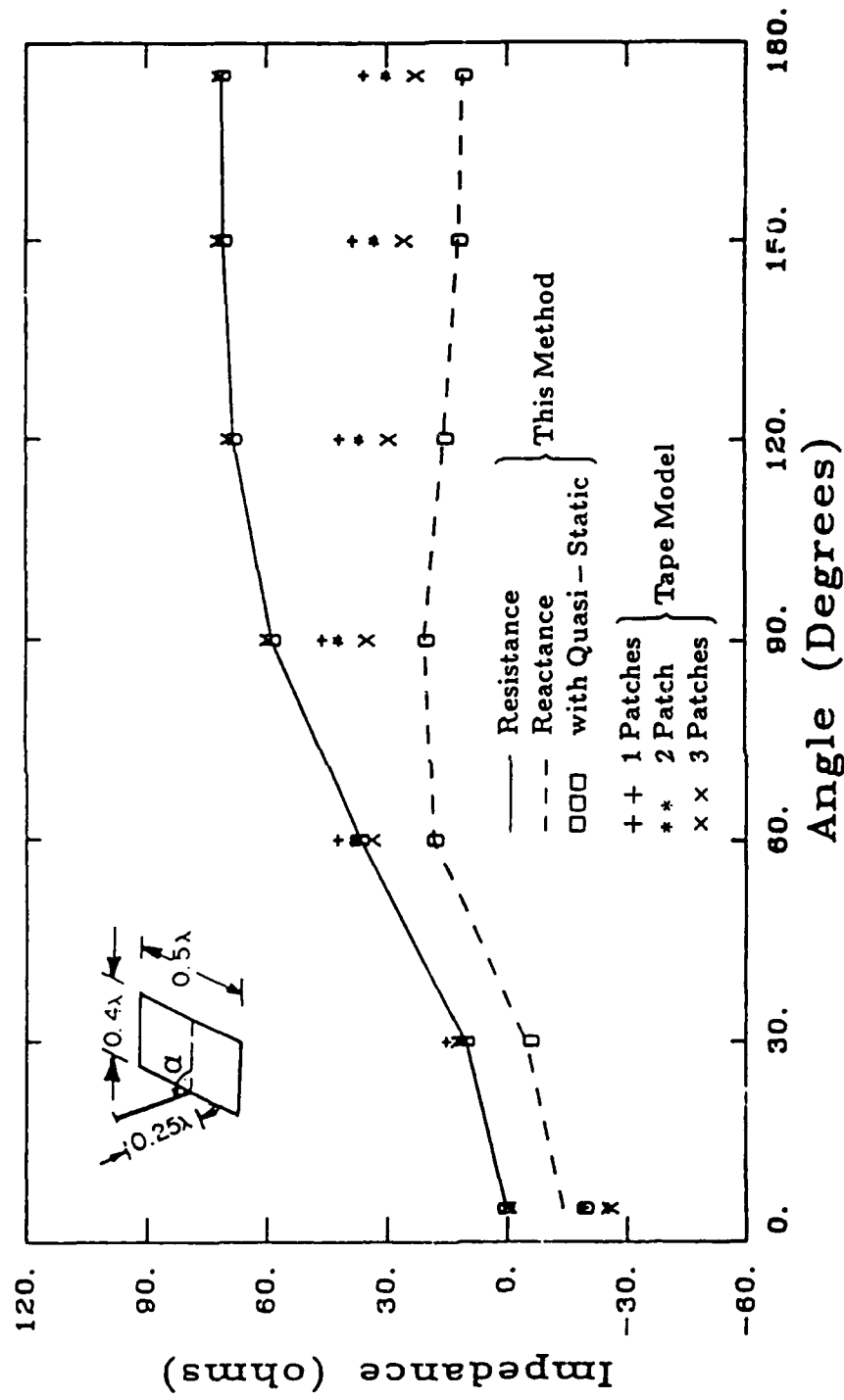
Figure 4.14: Input admittance compared to tape model for monopole attached to plate edge and fed at attachment point. Monopole length and radius are 0.25λ and 0.001λ, respectively, and it is mounted at center of longer edge of rectangular plate.

46

4.2.2 Wire mounted on an edge

Fig. 4.13 shows the input admittance as a function of bend angle for a monopole attached to the edge of a plate and fed at the attachment point. The length of the monopole is 0.25λ, its radius is 0.001λ, and it is mounted at the center of the longer edge of a 0.4λ × 0.5λ rectangular plate. The reactance is not in agreement with [18], in which both an exact Green's function to model the current in the neighborhood of the junction and a rectangular patch model was used, but several different calculations have been used to validate the present results. First, as shown in Fig. 4.14, the magnetostatic current distribution at the junction was calculated and used to deduce weighting coefficients for the junction triangle basis functions for representing the angular variation of the junction current. However, this produced an insignificant change in the result. Secondly, the wire was replaced by equivalent tape models, shown in Fig. 4.15, in which the width of the tape is four times the radius of the wire antenna [26, p. 20], and either 1, 2 or 3 patches are used at the junction to connect the tape to the surface. As Fig. 4.14 shows, as the number of patches increases, allowing the current to flow more freely in any direction on the plate, the results approach those of the present method. Finally, we also observe that as the wire angle α approaches zero, the wire and ground plane configuration approaches a quarter wavelength section of open circuited transmission line, whose input resistance and reactance should approach zero. The present results, contrasting to those of [18], more nearly follow this trend.

4.2.3 Wire mounted near or at a vertex

Fig. 4.16 illustrates the variation of the impedance as a function of attachment position for a quarter wave monopole mounted near or at a corner of a 0.4λ square plate. In Fig. 4.17, the same monopole is attached at or near a corner formed by three 0.4λ square plates. The antenna is attached normal to the top plate and driven at the attachment point. Its radius

is $a = 0.0015\lambda$. The results for these two cases are compared with calculated and measured results by Newman and Pozar [15]. The agreement is good in all three cases. Since the present method, in contrast to [15], should also apply for the wire located directly at the plate corners, we give results for these cases also.

4.3   Calculation of Far Field Patterns

Fig. 4.18 shows the radiation pattern of a wire of length 0.25λ and radius 0.007λ attached to a circular cylinder with diameter and height 0.25λ. Figs. 4.19-4.21 show similar results for cylinders of various sizes. The measured results shown for comparison are by Cooper [6]. In Fig. 4.22 is depicted a 0.25λ monopole mounted near the corner of a square plate with 1.0λ edge length. The results of Pozar [18] are also shown for comparison. Figs. 4.23 and 4.24 show a 0.25λ monopole mounted on a sphere with radius 0.2λ and 0.3λ respectively. The results are in good agreement with those of Tesche [4].
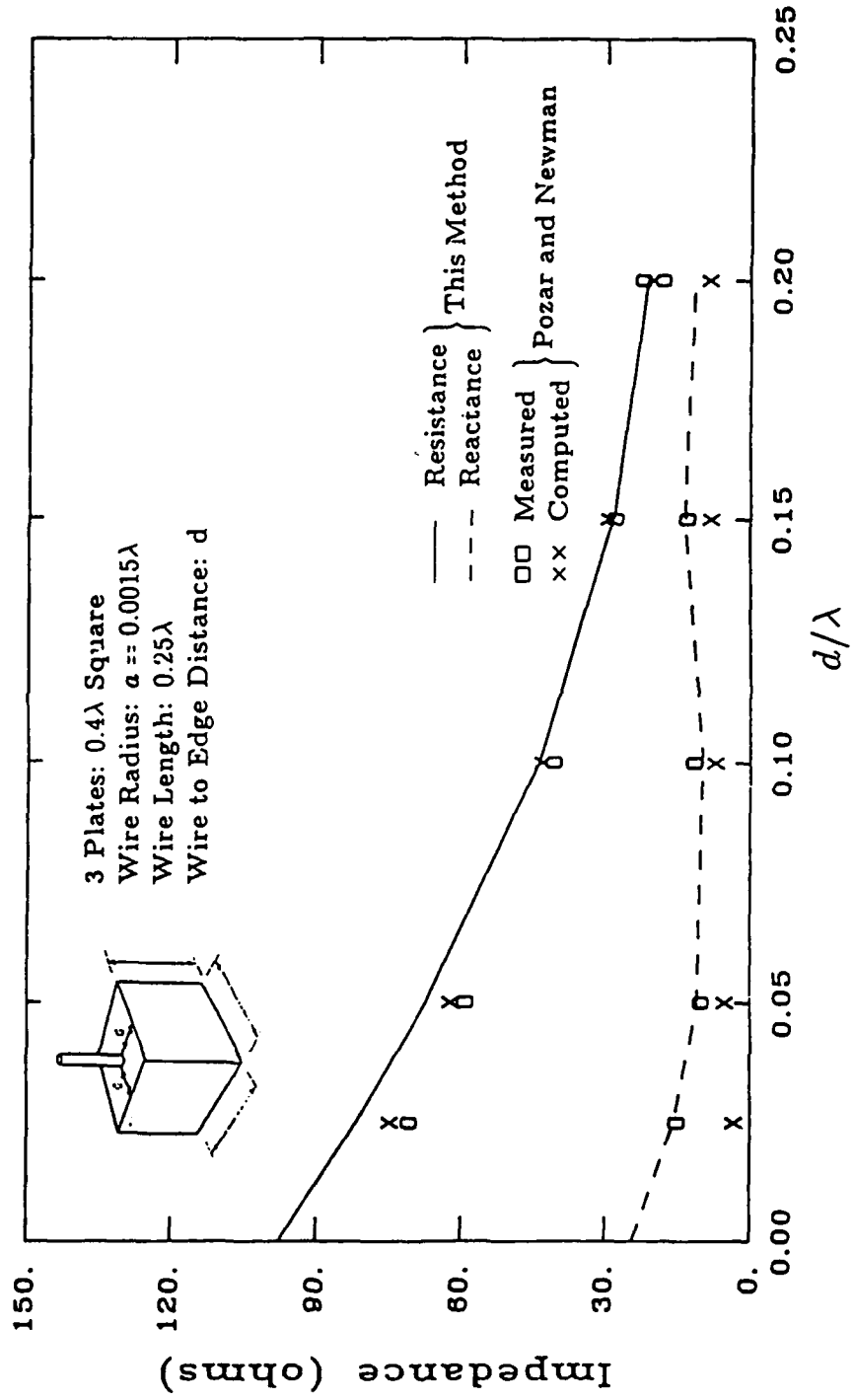
Figure 4.17: Input impedance as a function of attachment position for a quarter wave monopole mounted near or at a corner formed by three 0.4λ square plates. The antenna is attached normal to the top plate and driven at the attachment point. Its radius is a=0.0015λ.
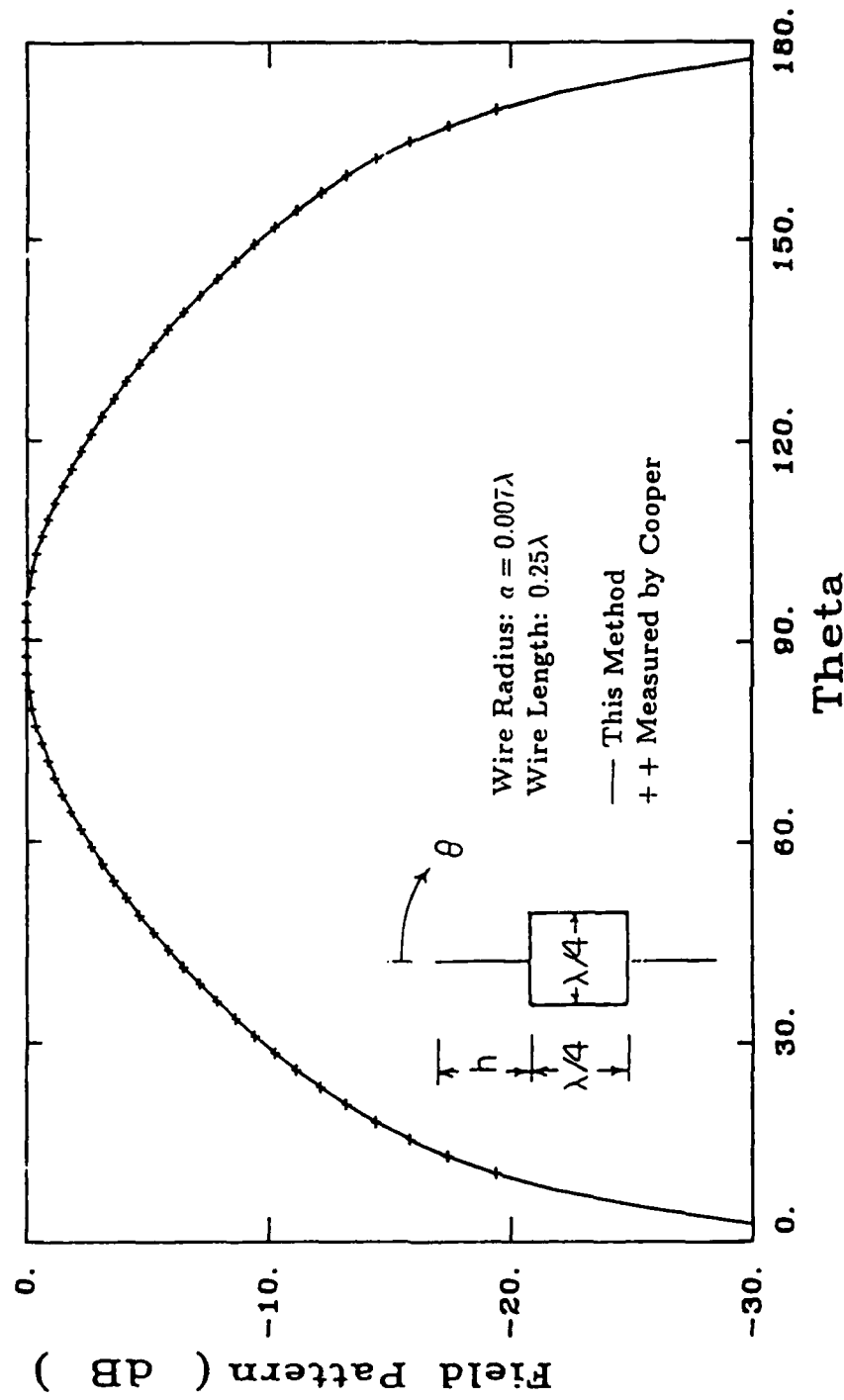
Figure 4.18: Radiation field pattern for a dipole whose arms are attached at the center of the endcaps of a circular cylinder. The wire radius and length are 0.007λ and 0.25λ, respectively.
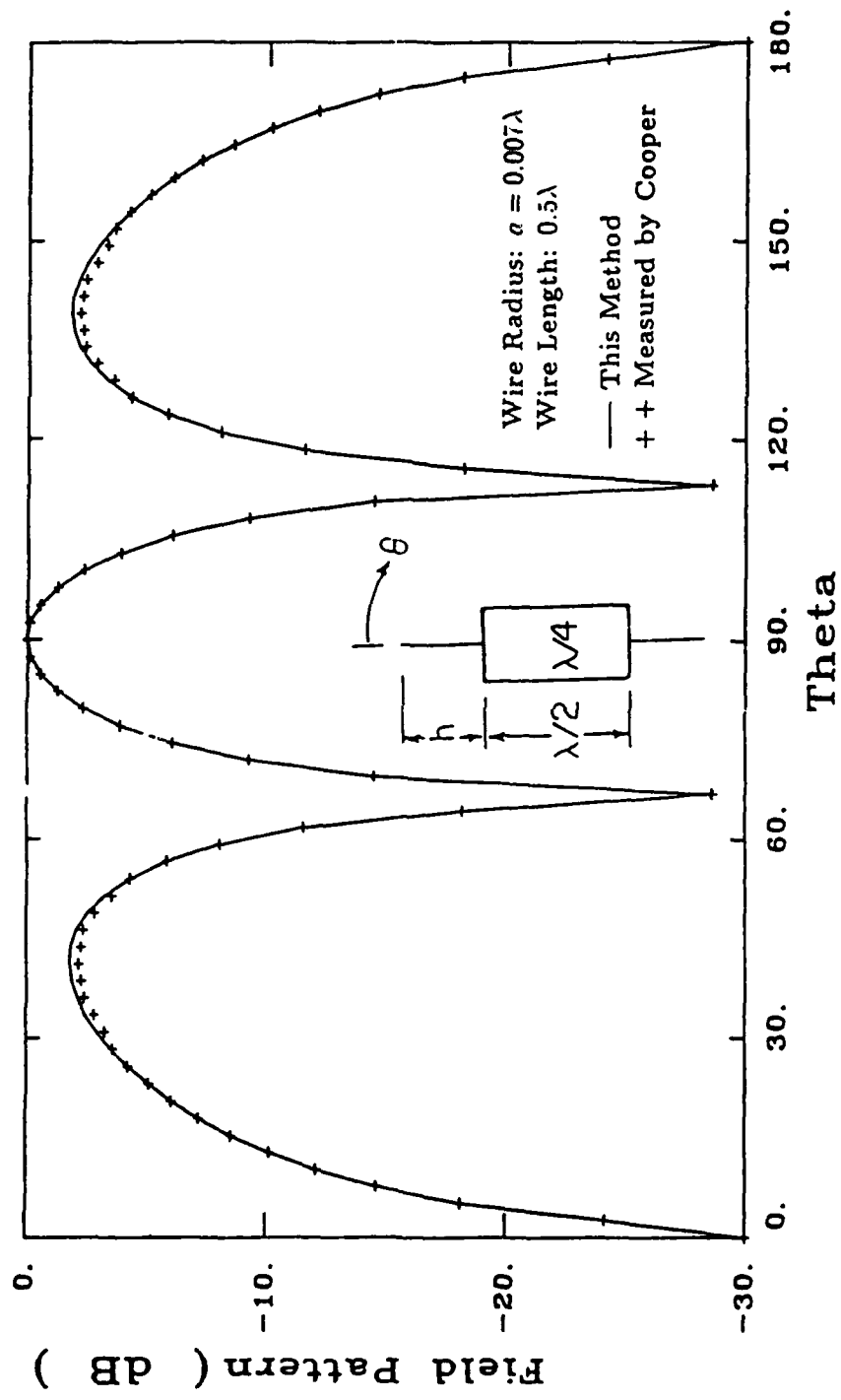
Figure 4.19: Radiation field pattern for a dipole whose arms are attached at the center of the endcaps of a circular cylinder. The wire radius and length are 0.007λ and 0.5λ, respectively.

53
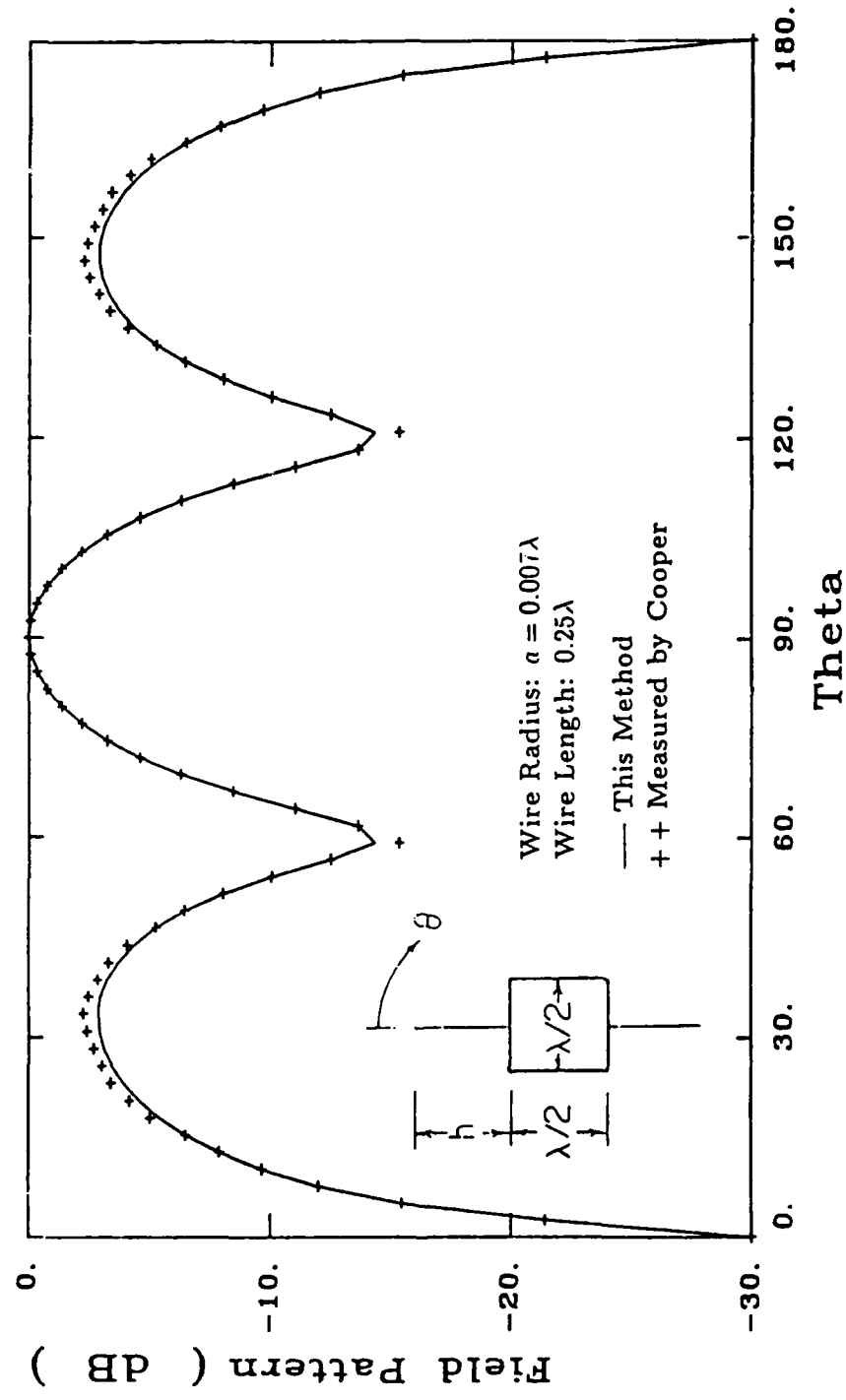
Figure 4.20: Radiation field pattern for a dipole whose arms are attached at the center of the endcaps of a circular cylinder. The wire radius and length are 0.007λ and 0.25λ, respectively.
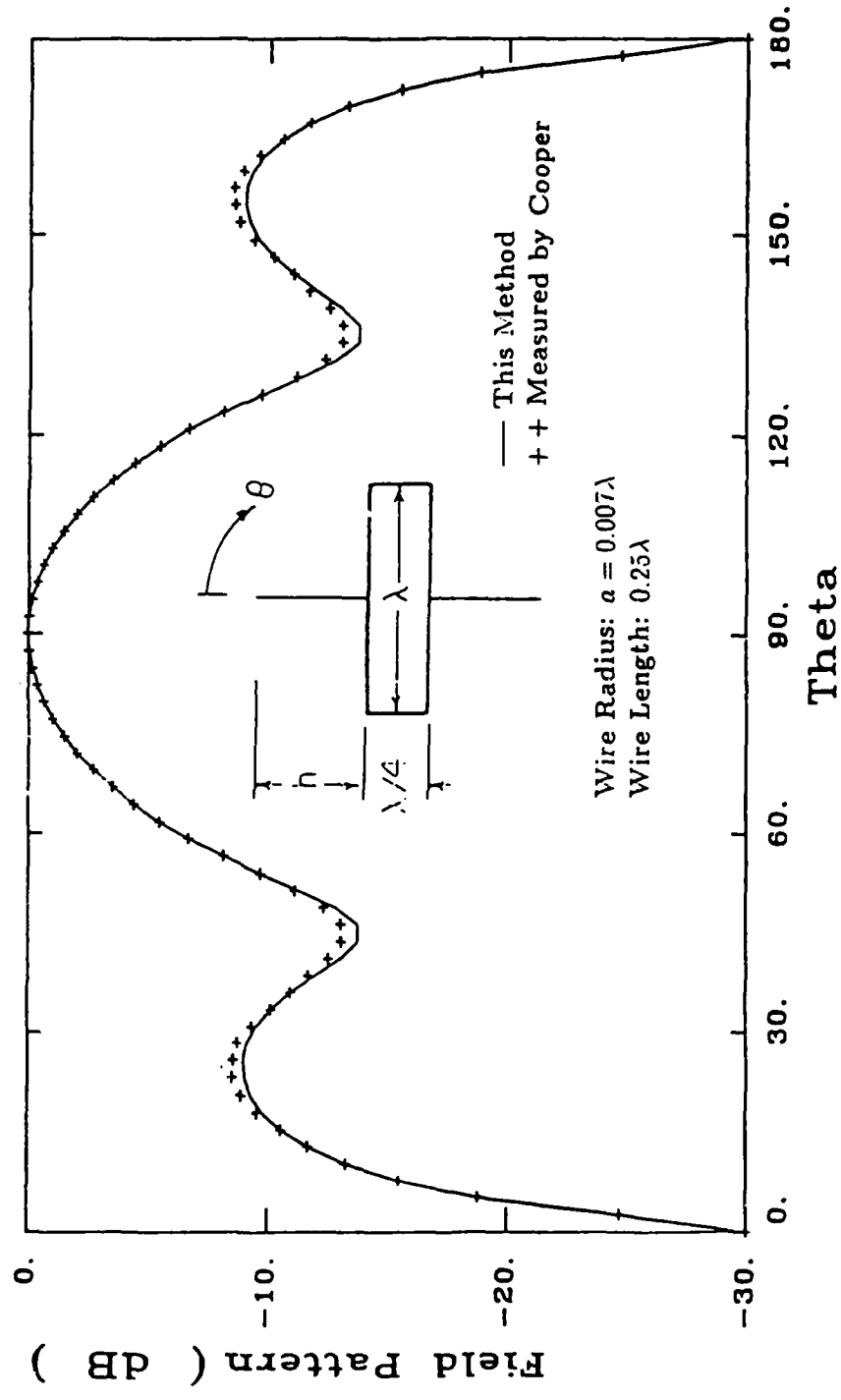
Figure 4.21: Radiation field pattern for a dipole whose arms are attached at the center of the endcaps of a circular cylinder. The wire radius and length are 0.007λ and 0.25λ, respectively.

55
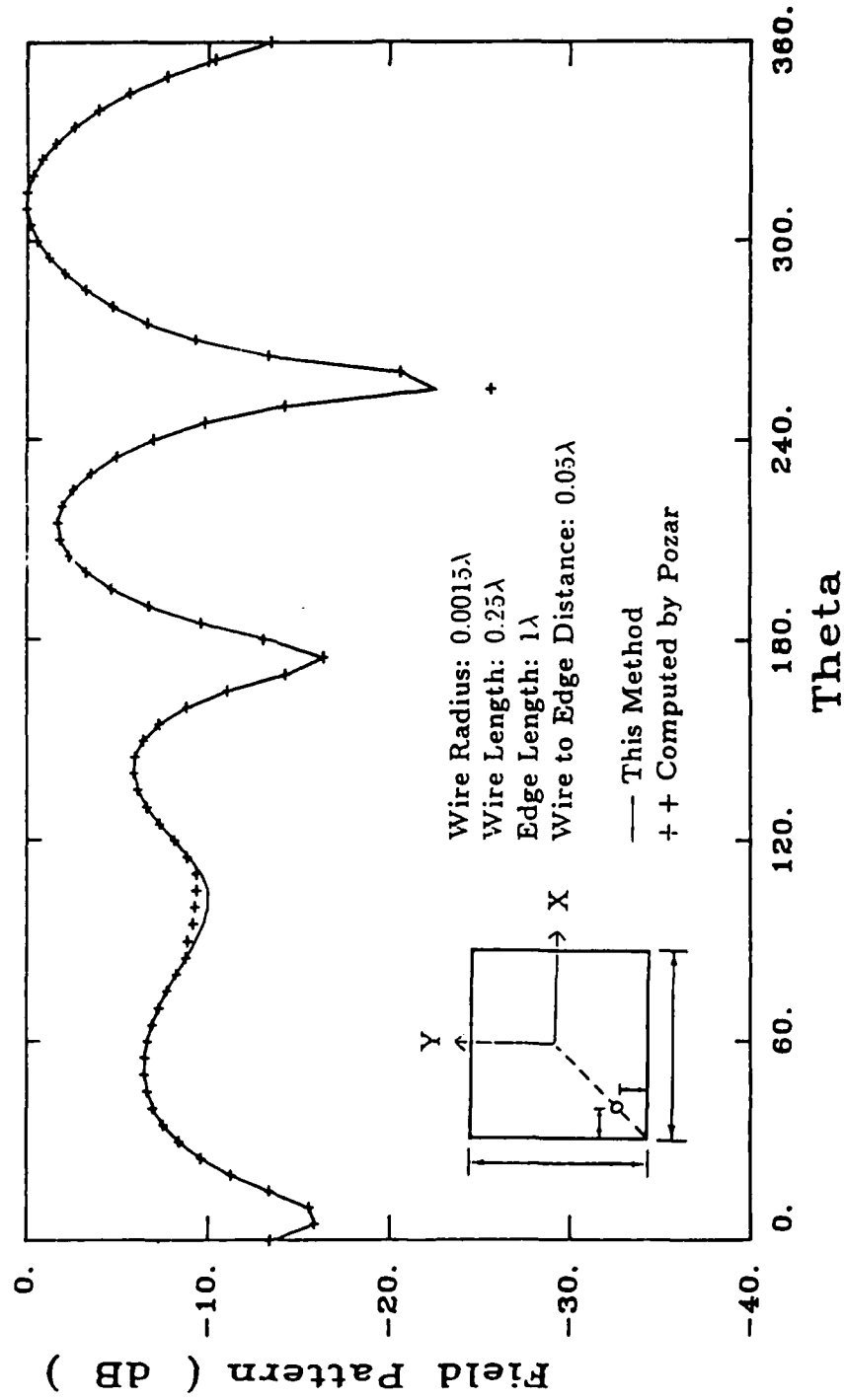
Figure 4.22: Radiation field pattern for a 0.25λ monopole mounted near the corner of a square plate with 1λ edge length.
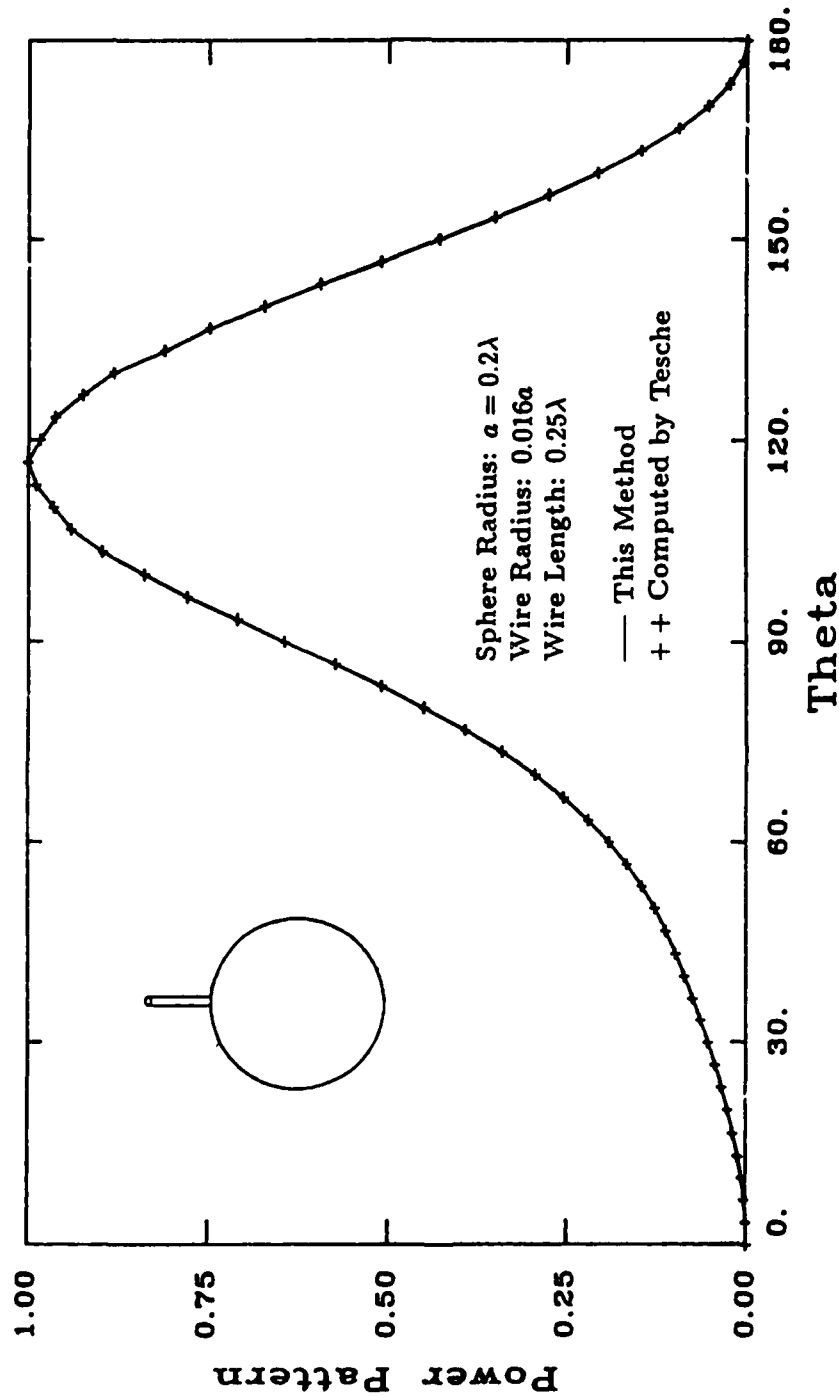
Figure 4.23: Radiation field pattern for a 0.25λ monopole mounted on a sphere of radius 0.2λ
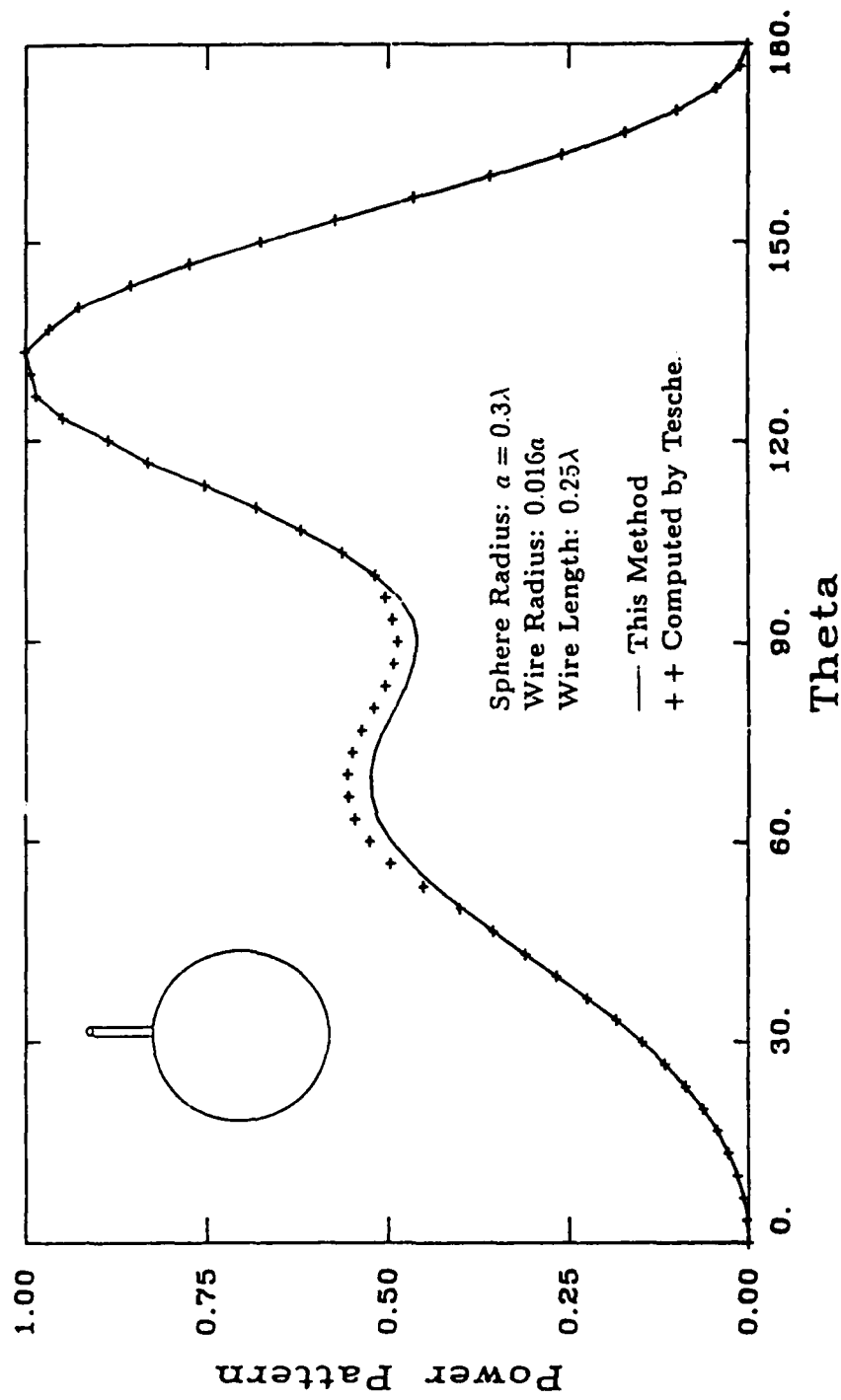
Figure 4.24: Radiation field pattern for a 0.25λ monopole mounted on a sphere of radius 0.3λ

Chapter 5

Summary

The electric field integral equation (EFIE) is used with the moment method to develop a simple and efficient numerical procedure for treating problems of scattering and radiation involving arbitrarily configured and arbitrarily connected bodies and wires. Three triangular-type basis functions are used to represent the physical currents on bodies, wires, and wire-to-body junctions. A junction basis function is developed which appears to be applicable to any junction configuration. Numerical results, which include comparisons with calculations and measurements found in the literature, illustrate the versatility, accuracy, and efficiency of the method for various junction configurations, including wires mounted on smooth surfaces, at edges, or at vertices.

Appendix A

Computation of Potential Integrals for Wire Basis Functions

The basis function associated with current crossing the nth node of a segmented wire model is given by (3.1), and its divergence is given by (3.2). Since $dS' = a\ d\phi\ d\ell'$, the vector and scalar partial potentials due to a unit current source associated with the nth node are given in terms of (3.14) and (3.15) as (c.f. Fig. 3.3(a))

$$
\begin{aligned}
A_n^W(\ell) &= \frac{\mu}{4\pi} \int_{S_n^{W+} + S_n^{W-}} A_n^W(\ell')\, K(\ell,\ell')\ d\ell' \\
&= \frac{\mu}{4\pi} \left[\int_{S_n^{W+}} \frac{\rho^+}{h_n^{W+}}\, K(\ell,\ell')\ d\ell' + \int_{S_n^{W-}} \frac{\rho^-}{h_n^{W-}}\, K(\ell,\ell')\ d\ell' \right],
\end{aligned}
\tag{A.1}
$$

$$
\begin{aligned}
\Phi_n^W(\ell) &= -\frac{1}{j4\pi\omega\epsilon} \int_{S_n^{W+} + S_n^{W-}} \left(\nabla_{\bullet} \cdot A_n^W(\ell') \right) K(\ell,\ell')\ d\ell' \\
&= -\frac{1}{j4\pi\omega\epsilon} \left[\int_{S_n^{W+}} \frac{1}{h_n^{W+}}\, K(\ell,\ell')\ d\ell' + \int_{S_n^{W-}} \frac{1}{h_n^{W-}}\, K(\ell,\ell')\ d\ell' \right],
\end{aligned}
\tag{A.2}
$$

where ℓ is arc length measured from a segment endpoint along the axis of the wire segment in the positive current reference direction, and

$$
K(\ell,\ell') = \frac{1}{2\pi} \int_{-\pi}^{\pi} \frac{e^{-jkR}}{R}\, d\phi,
\tag{A.3}
$$

is the so-called *exact kernel* in which R is the distance between observation point r and source point r' on the wire surface.

A.1 Integrals Associated with a Segment

It is computationally efficient to *simultaneously* compute *all* potential integrals associated with a given segment S^{W_i} (either S_n^{W+} or S_n^{W-}). The vector and scalar potentials associated with a segment involve the following three integrals:

$$I_1 = \frac{1}{h} \int_0^h s' \, K(s, s') \, ds', \tag{A.4}$$

$$I_2 = \frac{1}{h} \int_0^h (h - s') \, K(s, s') \, ds', \tag{A.5}$$

$$I_3 = \int_0^h K(s, s') \, ds', \tag{A.6}$$

where s' is a local segment arc length measured from the end of the axis of the source segment, and h is the length of the segment. The first and second integrals above are involved in the vector potential computation and the third is related to the scalar potential calculation.

A.2 Treatment of Singularities in Wire Potential Integrals

In numerical evaluation of (A.4)-(A.6), two cases are considered:

(a) The observation point is at least two segment lengths away from the source segment.

(b) The observation point is less than two segment lengths away from, or possibly on, the source segment.

For case (a), the so-called *reduced kernel*,

$$K_r(s, s') = \frac{e^{-jkR_r}}{R_r},$$

(A.7)

where

$$R_r = \sqrt{|r - r'|^2 + a^2}$$

(A.8)

and a is the source segment radius, may be used in place of (A.3) to eliminate the numerical integration which computation of the latter implies. With this replacement, (A.4)-(A.6) may be numerically integrated by Gaussian quadrature.

For case (b), the kernel is rewritten as

$$K(s, s') = \frac{1}{2\pi} \left[\int_{-\pi}^{\pi} \frac{e^{-jkR} - 1}{R} \, d\phi + \int_{-\pi}^{\pi} \frac{1}{R} \, d\phi \right].$$

(A.9)

The first integral of (A.9) now has a slowly varying integrand in which the reduced kernel approximation can be used (i.e., R is replaced by R_r of (A.8)) to obviate the need for double integration:

$$\frac{1}{2\pi} \int_{-\pi}^{\pi} \frac{e^{-jkR} - 1}{R} \, d\phi \approx \frac{e^{-jkR_r} - 1}{R_r}.$$

(A.10)

The integral resulting from substituting (A.10) for this slowly varying part of the kernel in (A.4)-(A.6) can be easily evaluated numerically by Gaussian quadrature.

The second integral in (A.9) contains the rapidly varying part of the kernel for observation points close to or on the source segment. Often the reduced kernel is used for this term as well, and its contribution can then be determined analytically. For segment lengths smaller than about five times the wire radius, however, this approach is not sufficiently accurate. On the other hand, it is easy to show that the second integral in (A.9) is expressible in terms of the complete elliptic integral of the first kind. To demonstrate this, we define a number of geometric parameters associated with the segment and the observation point in Fig. A.1. The distance between observation point r and source point r' is

62
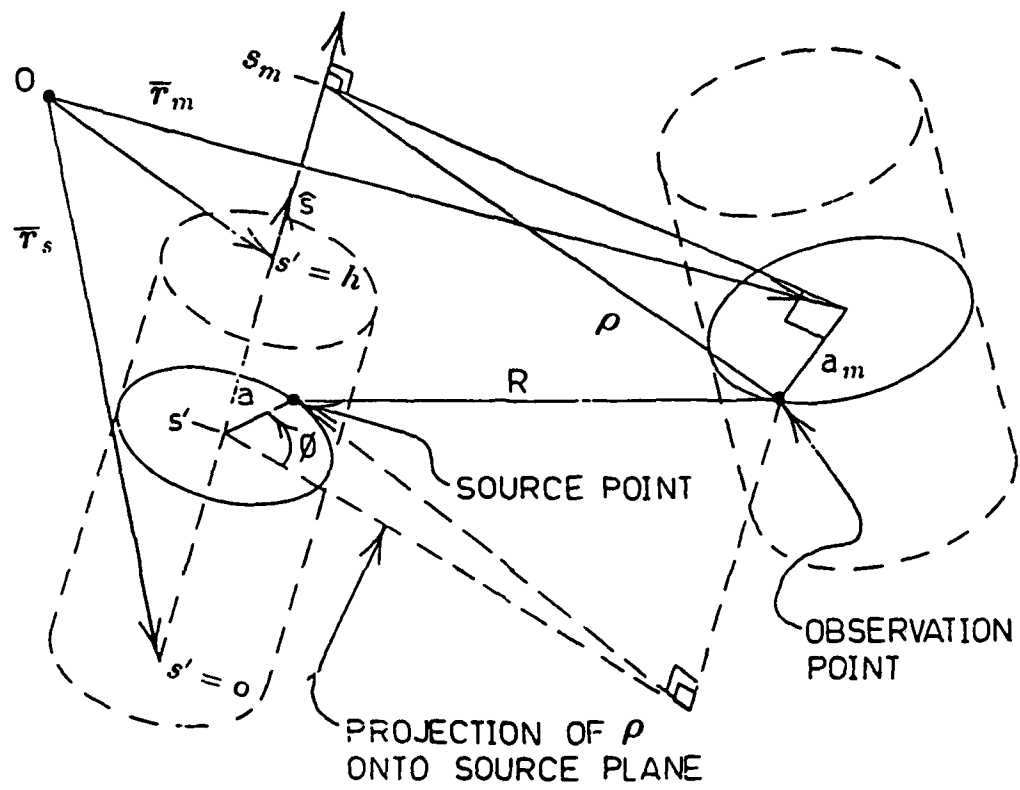
Figure A.1: Geometrical parameters associated with integration of a wire basis function.

$$R = |r - r'| = \sqrt{(s_m - s')^2 + \rho^2 + a^2 - 2\rho a \cos\phi}, \tag{A.11}$$

where

$$s_m = (r_m - r_s) \cdot \hat{s}, \quad \rho = \sqrt{|r_m - r_s|^2 - s_m^2 + a_m^2}. \tag{A.12}$$

Vector $\hat{s}$ is the unit vector pointing in the direction of the source segment, and a_m is the radius of the observation segment. Derivation of the relationship between the singular integral of (A.9) and the complete elliptic integral of the first kind may now be summarized as follows:

$$\frac{1}{2\pi} \int_{-\pi}^{\pi} \frac{1}{R} \, d\phi$$

$$= \frac{1}{2\pi} \int_{-\pi}^{\pi} \frac{d\phi}{\sqrt{(s_m - s')^2 + \rho^2 + a^2 - 2\rho a \cos\phi}}$$

$$= \frac{1}{2\pi} \int_{-\pi}^{\pi} \frac{d\phi}{\sqrt{(s_m - s')^2 + \rho^2 + a^2 + 2\rho a \cos\phi}}$$

$$= \frac{1}{\pi} \int_{0}^{\pi} \frac{d\phi}{\sqrt{(s_m - s')^2 + (\rho + a)^2 - 4\rho a \sin^2\dfrac{\phi}{2}}}$$

$$= \frac{2}{\pi} \frac{1}{\sqrt{(s_m - s')^2 + (\rho + a)^2}} \int_{0}^{\frac{\pi}{2}} \frac{d\psi}{\sqrt{1 - \beta^2 \sin^2\psi}}$$

$$= \frac{2}{\pi} \frac{K(\beta)}{\sqrt{(s_m - s')^2 + (\rho + a)^2}} = \frac{\beta}{\pi\sqrt{\rho a}} K(\beta), \tag{A.13}$$

where

$$\beta^2 = \frac{4\rho a}{(s_m - s')^2 + (\rho + a)^2}, \tag{A.14}$$

and $K(\beta)$ is the complete elliptic integral of the first kind, which can be computed from (17.3.34) of [27].

64

The elliptic integral becomes logarithmically singular when the observation point approaches the source point. It is difficult to numerically evaluate the integrals (A.4)-(A.6) in this case, and hence this singularity is first removed from the integrand by subtracting from it a singular term to which it is asymptotic, and then adding back the *analytically* evaluated contribution of the removed singular term. For extremely thin wires, better accuracy of the numerical integration is obtained if the singularity is extracted only in the interval $s' \in [s_u, s_v]$, where $s_u = \max(0, s_m - 15a)$ and $s_v = \min(h, s_m + 15a)$. For source points near observation points, the elliptic integral behaves as ((17.3.26) of [27])

$$\frac{\beta}{\pi\sqrt{\rho a}} K(\beta) \approx -\frac{2}{\pi(\rho + a)} \ln\left(\frac{\sqrt{1 - \beta^2}}{4}\right)$$

$$= -\frac{2}{\pi(\rho + a)} \ln\left(\frac{\sqrt{(s_m - s')^2 + (\rho - a)^2}}{4(\rho + a)}\right). \tag{A.15}$$

The last term is extracted from the kernel for numerical integration, and its contribution is determined by integrating it analytically. The resulting procedure is summarized in the following section.

A.3 Summary of Computation of Wire Potential Integrals

The computation of potential integrals associated with a wire segment, as given by (A.4)-(A.6), is summarized as follows:

For an observation point at least two segment lengths away from the source segment, the kernel is replaced by the reduced kernel approximation, (A.7) and (A.8), and the integral

$$I_i = \int_0^h f_i(s') \frac{e^{-jkR_r}}{R_r} ds' \tag{A.16}$$

is evaluated by Gaussian quadrature.

For an observation point less than two segment lengths from the source segment, the integral of the exact kernel is decomposed for evaluation as

$$I_i = \int_0^h f_i(s') \left[\frac{e^{-jkR_r} - 1}{R_r} \right] ds'$$

$$+ \frac{1}{\pi} \left(\int_0^{s_u} + \int_{s_v}^h \right) f_i(s') \frac{\beta}{\sqrt{\rho a}} K(\beta) ds'$$

$$+ \frac{1}{\pi} \left(\int_{s_u}^{s_m} + \int_{s_m}^{s_v} \right) f_i(s') \left[\frac{\beta}{\sqrt{\rho a}} K(\beta) + \frac{2}{\rho + a} \ln \frac{\sqrt{1 - \beta^2}}{4} \right] ds'$$

$$- \frac{2}{\rho + a} I_{si}, \quad i = 1, 2, \text{ or } 3, \tag{A.17}$$

where

$$I_{s1} = \int_{s_u}^{s_v} \frac{s'}{h} \ln \left(\frac{\sqrt{(s_m - s')^2 + (\rho - a)^2}}{4(\rho + a)} \right) ds'$$

$$= \frac{1}{4h} \left\{ \left[s'^2 - s_m^2 + (\rho - a)^2 \right] \ln \left[(s_m - s')^2 + (\rho - a)^2 \right] - 2s'^2 \ln \left[4(\rho + a) \right], \right.$$

$$\left. - 4s_m(\rho - a) \tan^{-1} \left(\frac{s_m - s'}{\rho - a} \right) - s'(s' + 2s_m) \right\} \Big|_{s'=s_u}^{s_v}, \tag{A.18}$$

$$I_{s3} = \int_{s_u}^{s_v} \ln \left(\frac{\sqrt{(s_m - s')^2 + (\rho - a)^2}}{4(\rho + a)} \right) ds'$$

$$= \left\{ \frac{(s' - s_m)}{2} \left[\ln \left(\frac{(s_m - s')^2 + (\rho - a)^2}{16(\rho + a)^2} \right) - 2 \right] \right.$$

$$\left. - (\rho - a) \tan^{-1} \left(\frac{s_m - s'}{\rho - a} \right) \right\} \Big|_{s'=s_u}^{s_v}, \tag{A.19}$$

$$I_{s2} = I_{s3} - I_{s1}, \tag{A.20}$$

66

and where R_r, s_m, and ρ are defined in (A.8), and (A.12), and

$$f_1(s') = \frac{s'}{h}, \quad f_2(s') = \frac{1}{h}(h - s'), \quad f_3(s') = 1.$$

The quantities s_u and s_v are defined as

$$s_u = \max(0, \ s_m - 15a),$$

$$s_v = \min(h, \ s_m + 15a).$$

If s_m is located outside of the source segment then $\left(\int_{s_u}^{s_m} + \int_{s_m}^{s_v}\right)$ in (A.17) is replaced by $\left(\int_{s_u}^{s_v}\right)$.

All the integrals in (A.17) have smooth integrands and can be numerically integrated by Gaussian quadrature.

Appendix B

Computation of Potential Integrals for Body Basis Functions

The basis function associated the nth edge of a surface patch model is given by (3.1), and its divergence is given by (3.2). The corresponding vector and scalar partial potentials due to this basis function are given in terms of (3.14) and (3.15) as (c.f. Fig. 3.3(b))

$$
\begin{aligned}
A_n^B(\boldsymbol{r}) &= \frac{\mu}{4\pi} \int_{S_n^{B+}+S_n^{B-}} \Lambda_n^B(\boldsymbol{r}') \frac{e^{-jkR}}{R} \, dS' \\
&= \frac{\mu}{4\pi} \left[\frac{1}{h_n^{B+}} \int_{S_n^{B+}} \boldsymbol{\rho}'^+ \frac{e^{-jkR}}{R} \, dS' + \frac{1}{h_n^{B-}} \int_{S_n^{B-}} \boldsymbol{\rho}'^- \frac{e^{-jkR}}{R} \, dS' \right],
\end{aligned}
\tag{B.1}
$$

$$
\begin{aligned}
\Phi_n^B(\boldsymbol{r}) &= -\frac{1}{j4\pi\omega\epsilon} \int_{S_n^{B+}+S_n^{B-}} \left(\nabla_s \cdot \Lambda_n^B(\boldsymbol{r}') \right) \frac{e^{-jkR}}{R} \, dS' \\
&= -\frac{1}{j4\pi\omega\epsilon} \left[\frac{2}{h_n^{B+}} \int_{S_n^{B+}} \frac{e^{-jkR}}{R} \, dS' + \frac{2}{h_n^{B-}} \int_{S_n^{B-}} \frac{e^{-jkR}}{R} \, dS' \right],
\end{aligned}
\tag{B.2}
$$

where

$$
R = |\boldsymbol{r} - \boldsymbol{r}'|.
$$

It is computationally efficient to *simultaneously* compute *all* the potential integrals associated with each patch S^{Bq} (either S_n^{B+} or S_n^{B-}). The vector and scalar partial potentials
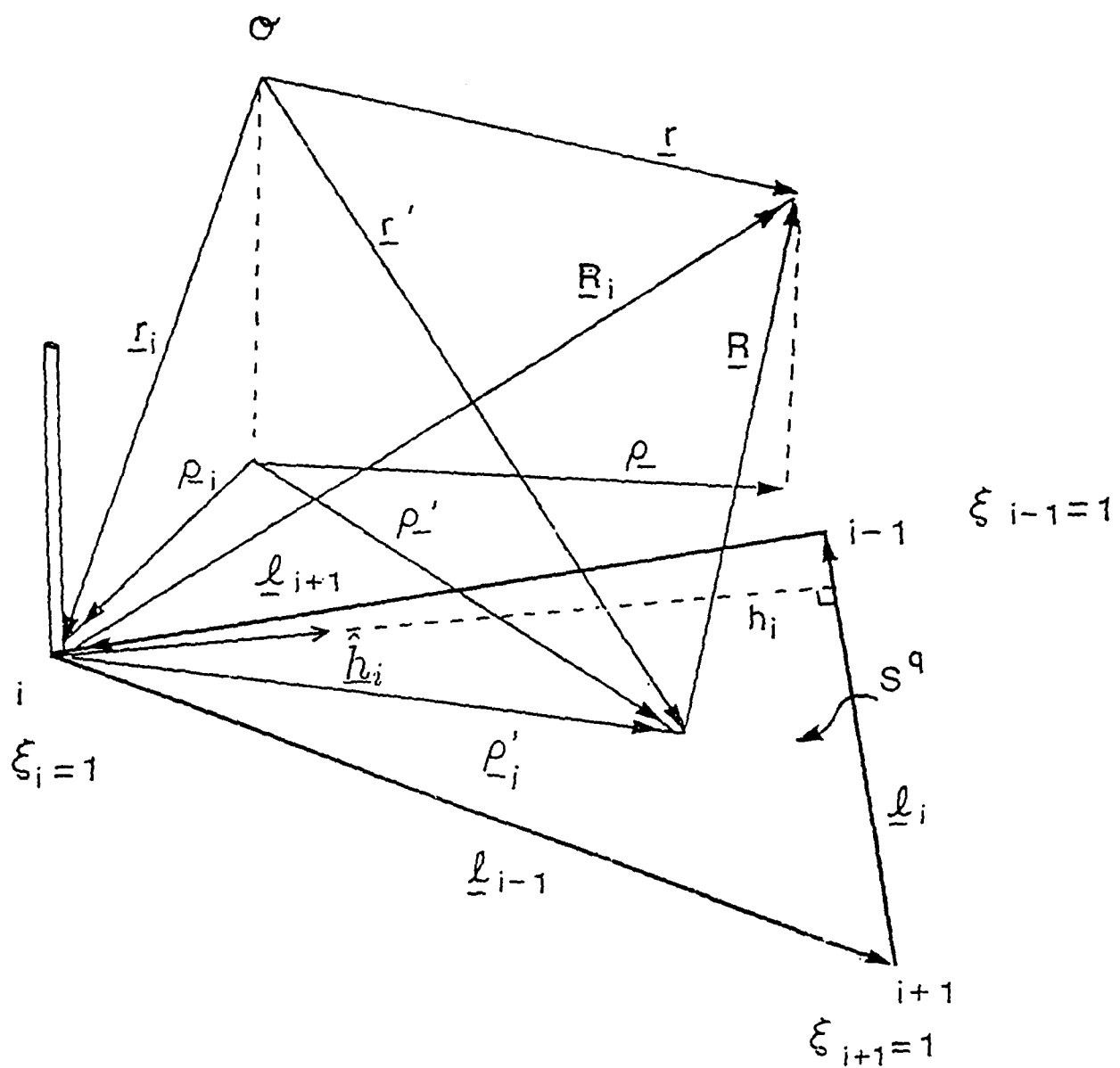
Figure B.1: Geometrical parameters associated with integration of body and junction basis functions.

evaluated at observation point r due to a basis current directed outward across the ith edge ($i = 1, 2$, or 3) of the qth triangular patch, S^{Bq}, are defined as (c.f. Fig. B.1)

$$A_i^B(r) = \frac{\mu}{4\pi} \int_{S^{Bq}} \frac{\rho_i'}{h_i} \frac{e^{-jkR}}{R} dS',$$ (B.3)

$$\Phi_i^B(r) = -\frac{1}{j4\pi\omega\epsilon} \int_{S^{Bq}} \frac{2}{h_i} \frac{e^{-jkR}}{R} dS'.$$ (B.4)

If the current is directed inward across the ith edge, the right hand sides of (B.3) and (B.4) are multiplied by (-1).

B.1 Treatment of Singularities in Body Potential Integrals

The integrands of $A_i^B(r)$ and $\Phi_i^B(r)$ are singular at $R = 0$ corresponding to an observation point coincident with a source point. When r is not close to the source triangle, one can easily evaluate (B.3) and (B.4) by numerical quadrature as discussed in Appendix E. Thus when r is close to or on the source triangle, extraction of the $1/R$ behavior is necessary before numerical integration is performed. We can represent both of these cases by introducing a *closeness parameter* $\sigma(r)$ defined as

$$\sigma(r) = \begin{cases} 0 & \text{,if distance } R_c \text{ is larger than the longest edge of } S^{Bq}, \\ 1 & \text{,otherwise.} \end{cases}$$ (B.5)

where R_c is the distance from the centroid of the source triangular patch to the observation point. Thus we write (B.3) and (B.4) as

$$A_i^B(r) = \frac{\mu}{4\pi} \frac{1}{h_i} \left[\int_{S^{Bq}} \rho_i' \frac{e^{-jkR} - \sigma(r)}{R} dS' + \sigma(r) \int_{S^{Bq}} \frac{\rho_i'}{R} dS' \right]$$ (B.6)

and

$$\Phi_i^B(r) = -\frac{1}{j4\pi\omega\epsilon} \frac{2}{h_i} \left[\int_{S^{Bq}} \frac{e^{-jkR} - \sigma(r)}{R} dS' + \sigma(r) \int_{S^{Bq}} \frac{1}{R} dS' \right].$$ (B.7)

The integrand of the first integral of (B.6) and (B.7) is always slowly varying and can be satisfactorily integrated numerically via the methods of Appendix E. The remaining integrals in both (B.6) and (B.7) can be integrated analytically, and are given as [28]

$$g_s \equiv \int_{S^{Bq}} \frac{1}{R} dS' = \sum_i \hat{P}_i^0 \cdot \hat{u}_i \left[P_i^0 \ln \frac{R_i^+ + l_i^+}{R_i^- + l_i^-} - |d| \left(\tan^{-1} \frac{P_i^0 l_i^+}{(R_i^0)^2 + |d|R_i^+} \right. \right.$$

$$\left. \left. - \tan^{-1} \frac{P_i^0 l_i^-}{(R_i^0)^2 + |d|R_i^-} \right) \right] \tag{B.8}$$

and

$$g_i \equiv \int_{S^{Bq}} \frac{\rho'_i}{R} dS' = \int_{S^{Bq}} \frac{\rho' - \rho_i}{R} dS'$$

$$= \int_{S^{Bq}} \frac{\rho' - \rho}{R} dS' + (\rho - \rho_i) \int_{S^{Bq}} \frac{1}{R} dS'$$

$$= \frac{1}{2} \sum_i \hat{u}_i \left[(R_i^0)^2 \ln \frac{R_i^+ + l_i^+}{R_i^- + l_i^-} + l_i^+ R_i^+ - l_i^- R_i^- \right] + (\rho - \rho_i) g_s. \tag{B.9}$$

For numerical evaluation of (B.6) and (B.7), it is convenient to express all their terms in the area coordinates of Appendix E. Accordingly, using (E.5), the position vector ρ'_i relative to vertex i is expanded in terms of the adjacent edge vectors, which act as basis vectors in the local coordinate system on patch S^{Bq}:

$$\rho'_i = \xi_{i+1} \ell_{i-1} - \xi_{i-1} \ell_{i+1}, \tag{B.10}$$

where the edge vectors $\ell_{i \pm 1}$ are defined in Fig. B.1. Substituting (B.10) into (B.6) and using (E.7), we can express the vector function $A_i^B(r)$ as

$$A_i^B(r) = \frac{\mu}{4\pi h_i} \left[(A_i^{B+} + \sigma(r) g_i^+) \ell_{i-1} - (A_i^{B-} + \sigma(r) g_i^-) \ell_{i+1} \right], \tag{B.11}$$

where

$$A_i^{B\pm} = 2A \int_0^1 \int_0^{1-\xi_i} \xi_{i\pm1} \frac{e^{-jkR} - \sigma(r)}{R} d\xi_{i\pm1} d\xi_i, \tag{B.12}$$

71

and

$$g_i^{\pm} = 2A \int_0^1 \int_0^{1-\xi_i} \frac{\xi_{i\pm1}}{R} \, d\xi_{i\pm1} \, d\xi_i. \tag{B.13}$$

The singular integrals $g_i^{\pm}$ in (B.11) are related to the vector $\boldsymbol{g}_i$ of (B.9) as may be seen by substituting (B.10) into (B.9) and comparing to (B.13). We obtain

$$\boldsymbol{g}_i = g_i^+ \, \boldsymbol{\ell}_{i-1} - g_i^- \, \boldsymbol{\ell}_{i+1}, \tag{B.14}$$

where, from (E.10), we have

$$g_i^{\pm} = - \frac{\hat{\boldsymbol{h}}_{i\pm1}}{h_{i\pm1}} \cdot \boldsymbol{g}_i, \tag{B.15}$$

and this result, together with (B.8) and (B.9), allows all but the terms $A_i^{B\pm}$ in (B.11) to be evaluated.

Similarly, the scalar function $\Phi_i^B(\boldsymbol{r})$ can be expressed as

$$\Phi_i^B(\boldsymbol{r}) = -\frac{1}{j4\pi\omega\epsilon} \frac{2}{h_i} \left[I + \sigma(\boldsymbol{r}) \, g_s \right], \tag{B.16}$$

with

$$I = 2A \int_0^1 \int_0^{1-\xi_i} \frac{e^{-jkR} - \sigma(\boldsymbol{r})}{R} \, d\xi_{i\pm1} \, d\xi_i, \tag{B.17}$$

and g_s is defined as in (B.8).

The remaining terms in (B.11) and (B.16)—the nonsingular contributions to the vector and scalar potentials, $A_i^{B\pm}$ and I, respectively—are computed by numerical quadrature as discussed in Appendix E.

B.2   Summary of Computation of Body Potential Integrals

The vector potential integral associated with an edge as given by (B.3) is obtained by substituting (B.8), (B.9), and (B.15) into (B.11) and is summarized as follows:

$$A_i^B(\boldsymbol{r}) = \frac{\mu}{4\pi h_i} \left[\left(2A \int_0^1 \int_0^{1-\xi_i} \xi_{i+1} \frac{e^{-jkR} - \sigma(\boldsymbol{r})}{R} d\xi_{i+1} d\xi_i - \sigma(\boldsymbol{r}) \frac{\hat{h}_{i+1} \cdot \boldsymbol{g}_i}{h_{i+1}} \right) \boldsymbol{\ell}_{i-1} \right.$$

$$\left. - \left(2A \int_0^1 \int_0^{1-\xi_i} \xi_{i-1} \frac{e^{-jkR} - \sigma(\boldsymbol{r})}{R} d\xi_{i-1} d\xi_i - \sigma(\boldsymbol{r}) \frac{\hat{h}_{i-1} \cdot \boldsymbol{g}_i}{h_{i-1}} \right) \boldsymbol{\ell}_{i+1} \right], \quad \text{(B.18)}$$

where $\sigma(\boldsymbol{r})$ is defined in (B.5).

The scalar potential integral associated with face S^{Bq} in (B.4) is evaluated by substituting (B.17) and (B.8) into (B.16) and the result is summarized as follows:

$$\Phi_i^B(\boldsymbol{r}) = -\frac{1}{j4\pi\omega\epsilon} \frac{2}{h_i} \left[2A \int_0^1 \int_0^{1-\xi_i} \frac{e^{-jkR} - \sigma(\boldsymbol{r})}{R} d\xi_{i\pm1} d\xi_i + \sigma(\boldsymbol{r}) g_s \right]. \quad \text{(B.19)}$$

The integrals in Eqs. (B.18) and (B.19) are well-behaved and may be integrated numerically via (E.12).

Appendix C

Computation of Potential Integrals for Junction Basis Functions

The basis function associated with current entering the nth junction of a wire/body junction model is given by (3.3) and its divergence is given by (3.5). The vector and scalar potentials due to a unit current source associated with the nth junction may be given in terms of (3.14) and (3.15) as (c.f. Figs. 3.4 and B.1)

$$A_n{}^J(r) = \frac{\mu}{4\pi} \int_{S_n^{J+}+S_n^{J-}} \Lambda_n^J(r') \frac{e^{-jkR}}{R} dS'$$

$$= \frac{\mu}{4\pi} \left\{ \int_{S_n^{J-}} \Lambda_n^W(r') \frac{e^{-jkR}}{R} dS' + \sum_{l=1}^{N_{Jn}} K_{nl} \left[\int_{S_{nl}^{J+}} \Lambda_{nl}^B(r') \frac{e^{-jkR}}{R} dS' \right. \right.$$

$$\left. \left. - \int_{S_{nl}^{J+}} \frac{(h_{nl}^{J+})^2}{(\rho'^+ \cdot \hat{h}_{nl}^{J+})^2} \Lambda_{nl}^B(r') \frac{e^{-jkR}}{R} dS' \right] \right\}, \qquad (C.1)$$

$$\Phi_n^J(r) = -\frac{1}{j4\pi\omega\epsilon} \int_{S_n^{J+}+S_n^{J-}} \left(\nabla_\bullet \cdot \Lambda_n^J(r') \right) \frac{e^{-jkR}}{R} dS'$$

$$= -\frac{1}{j4\pi\omega\epsilon} \left[\frac{-1}{h_{nl}^{J-}} \int_{S_n^{J-}} \frac{e^{-jkR}}{R} dS' + \sum_{l=1}^{N_{Jn}} \frac{2K_{nl}}{h_{nl}^{J+}} \int_{S_{nl}^{J+}} \frac{e^{-jkR}}{R} dS' \right]. \qquad (C.2)$$

All the integrals in (C.1) and (C.2) except the last integral in (C.1) are evaluated in Appendices A and B. For the remaining integral, we first assume that the qth junction

74

surface patch has a junction at vertex i (a local index) in the patch. Then the integral can be written in the form

$$A_i^{J'}(\boldsymbol{r}) = \frac{\mu}{4\pi}K_i \int_{S^{J_q}} \frac{h_i^2}{(\boldsymbol{\rho'}_i \cdot \hat{\boldsymbol{h}}_i)^2} \Lambda_i^B(\boldsymbol{r'}) \frac{e^{-jkR}}{R} dS'$$

$$= \frac{\mu}{4\pi}K_i \, h_i \int_{S^{J_q}} \frac{\boldsymbol{\rho'}_i}{(\boldsymbol{\rho'}_i \cdot \hat{\boldsymbol{h}}_i)^2} \frac{e^{-jkR}}{R} dS'. \tag{C.3}$$

where K_i is the weight factor for the patch and the remaining quantities are defined in Fig. B.1. Evaluation of this integral is considered in the following section.

C.1   Treatment of Singularities in Junction Potential Integrals

The integrand of $A_i^{J'}(\boldsymbol{r})$ in (C.3) is singular when the source point is at junction vertex (i.e., when $\boldsymbol{\rho'}_i = 0$), and when an observation point is coincident with a source point (i.e., when $R = 0$). Thus when $\boldsymbol{r}$ is close to the source triangle or $\boldsymbol{r'}$ is close to the junction vertex, extraction of the dominant singular or nearly singular form of the integrand is necessary before numerical integration is performed. To discern the behavior of the integrand near these singularities we expand it in a Taylor series about each singularity.

At $\boldsymbol{\rho'}_i = 0$ we expand terms of the integrand in Taylor series in $\boldsymbol{\rho'}_i$ and then combine them to obtain the Taylor series for the integrand as a whole. For example (c.f. Fig. B.1), we first note that

$$R = |\boldsymbol{R}_i - \boldsymbol{\rho'}_i| = \sqrt{R_i^2 + \rho_i'^2 - 2\boldsymbol{R}_i \cdot \boldsymbol{\rho'}_i}. \tag{C.4}$$

Since for sufficiently small $\boldsymbol{\rho'}_i$, it is clear from Fig. B.1 that $R_i^2 > \rho_i'^2 - 2\boldsymbol{R}_i \cdot \boldsymbol{\rho'}_i$, and hence R may be expanded in the series

$$R \cong R_i \left[1 + \frac{1}{2} \frac{\rho_i'^2 - 2\boldsymbol{\rho'}_i \cdot \boldsymbol{R}_i}{R_i^2} + \cdots \right]. \tag{C.5}$$

Thus the exponential in (C.3) may be expanded as

$$e^{-jkR} \cong e^{-jkR_i} \left[1 - jk\frac{\rho_i'^2 - 2\rho_i' \cdot R_i}{2R_i} + \cdots \right] \tag{C.6}$$

and hence

$$\frac{e^{-jkR}}{R} \cong \frac{e^{-jkR_i}}{R_i} \left[1 + \left(jk + \frac{1}{R_i} \right) \frac{\rho_i' \cdot R_i}{R_i} + \cdots \right]. \tag{C.7}$$

Finally, we have

$$\frac{\rho_i'}{(\rho_i' \cdot \hat{h}_i)^2} \frac{e^{-jkR}}{R} \cong f_{\rho}, \tag{C.8}$$

where

$$f_{\rho} = \frac{\rho_i'}{(\rho_i' \cdot \hat{h}_i)^2} \frac{e^{-jkR_i}}{R_i} \left[1 + (jk + \frac{1}{R_i}) \frac{\rho_i' \cdot R_i}{R_i} \right]. \tag{C.9}$$

All the higher order terms in the series vanish as $\rho_i' \to 0$.

For the singularity at $R = 0$, we expand the integrand in a Taylor series in R. Since (c.f. Fig. B.1)

$$\rho_i' = R_i - R \tag{C.10}$$

then

$$\rho_i' \cdot \hat{h}_i = R_i \cdot \hat{h}_i \left[1 - \frac{R \cdot \hat{h}_i}{R_i \cdot \hat{h}_i} \right] \tag{C.11}$$

and therefore

$$\frac{1}{(\rho_i' \cdot \hat{h}_i)^2} \cong \frac{1}{(R_i \cdot \hat{h}_i)^2} \left[1 + 2\frac{R \cdot \hat{h}_i}{R_i \cdot \hat{h}_i} + \cdots \right]. \tag{C.12}$$

Since

$$\frac{e^{-jkR}}{R} \cong \frac{1}{R} - jk - \frac{k^2 R}{2} + \cdots, \tag{C.13}$$

we have

$$\frac{\rho'_i}{(\rho'_i \cdot \hat{h}_i)^2} \frac{e^{-jkR}}{R} \cong \frac{\rho'_i}{(R_i \cdot \hat{h}_i)^2} \left[\frac{1}{R} + \frac{2R \cdot \hat{h}_i}{(R_i \cdot \hat{h}_i)R} + \cdots \right].$$

$$= \frac{1}{(R_i \cdot \hat{h}_i)^2} \left[\frac{\rho'_i}{R} + \frac{2[(\rho - \rho_i) - (\rho - \rho')] R \cdot \hat{h}_i}{(R_i \cdot \hat{h}_i)R} \cdots \right]$$

$$\cong \frac{1}{(R_i \cdot \hat{h}_i)^2} \left[\frac{\rho'_i}{R} + \frac{2(\rho - \rho_i)(R_i - \rho'_i) \cdot \hat{h}_i}{(R_i \cdot \hat{h}_i)R} \cdots \right] \tag{C.14}$$

in which we have used the following relations:

$$\rho'_i = R_i - R = (\rho - \rho_i) - (\rho - \rho'),$$

$$\frac{|\rho - \rho'|R \cdot \hat{h}_i}{R} \longrightarrow 0 \quad \text{as} \quad R \longrightarrow 0 \quad \text{since} \quad |\rho - \rho'| \le R.$$

All the higher order terms in the series are bounded and well-behaved as $R \to 0$, and since

$$R \cdot \hat{h}_i = (R_i - \rho'_i) \cdot \hat{h}_i = (\rho - \rho_i - \rho'_i) \cdot \hat{h}_i,$$

we define

$$f_R \equiv \frac{1}{(R_i \cdot \hat{h}_i)^2} \left[\frac{\rho'_i}{R} + \frac{2(\rho - \rho_i)[(\rho - \rho_i) - \rho'_i] \cdot \hat{h}_i}{(R_i \cdot \hat{h}_i)R} \right]. \tag{C.15}$$

With the expansions of f_ρ and f_R in (C.9) and (C.15), then (C.3) can be rewritten as

$$A_i^{J'}(r) = \frac{\mu}{4\pi} K_i h_i \left[\int_{S^{J_q}} F \, dS' + \int_{S^{J_q}} f_\rho \, dS' + \sigma(r) \int_{S^{J_q}} f_R \, dS' \right], \tag{C.16}$$

where

$$F = \frac{\rho'_i}{(\rho'_i \cdot \hat{h}_i)^2} \frac{e^{-jkR}}{R} - f_\rho - \sigma(r) f_R. \tag{C.17}$$

and $\sigma(r)$ is defined in (B.5). The integrand of the first integral in (C.16) has the singularity at $\rho'_i = 0$ removed, and—when the observation point is near the source triangular patch S^{Bq}—has the $1/R$ behavior removed. The integrand is thus bounded and continuous,

77

and the integral can be integrated numerically by numerical quadrature as described in Appendix E. At $R = 0$, $\boldsymbol{F}$ is indeterminant and hence, for numerical purposes, is replaced by its limit,

$$\lim_{R \to 0} \boldsymbol{F} = -\frac{\boldsymbol{\rho}'_i}{(\boldsymbol{\rho}'_i \cdot \hat{\boldsymbol{h}}_i)^2} \left[jk + \frac{1 + jkR_i}{R_i} \left(2 + jkR_i \right) \right]. \tag{C.18}$$

The second and the third integrals of (C.16), as shown below, can be integrated analytically.

C.2 Efficient Numerical Evaluation of Integrals

For efficient computation, we rewrite the vector integral equation (C.16) and (C.17) in terms of adjacent edges which act as basis vectors in a local coordinate system. Since

$$\boldsymbol{\rho}'_i \cdot \hat{\boldsymbol{h}}_i = h_i \left(1 - \xi_i \right), \tag{C.19}$$

from (B.10) and (C.16-C.18), we have

$$A_i^{J'}(\boldsymbol{r}) = \frac{\mu}{4\pi} K_i h_i \left(A_i^{J'+} \boldsymbol{\ell}_{i-1} - A_i^{J'-} \boldsymbol{\ell}_{i+1} \right), \tag{C.20}$$

and

$$\boldsymbol{F} = F^+ \boldsymbol{\ell}_{i-1} - F^- \boldsymbol{\ell}_{i+1}, \tag{C.21}$$

where

$$A_i^{J'\pm} = \int_{S^{J_q}} F^\pm \, dS' + \int_{S^{J_q}} f_\rho^\pm \, dS' + \sigma(\boldsymbol{r}) \int_{S^{J_q}} f_R^\pm \, dS', \tag{C.22}$$

and

$$F^\pm = \frac{1}{h_i^2} \frac{\xi_{i\pm1}}{(1 - \xi_i)^2} \frac{e^{-jkR}}{R} - f_\rho^\pm - \sigma(\boldsymbol{r}) f_R^\pm, \tag{C.23}$$

$$\lim_{R \to 0} F^\pm = -\frac{1}{h_i^2} \frac{\xi_{i\pm1}}{(1 - \xi_i)^2} \left[jk + \frac{1 + jkR_i}{R_i} \left(2 + jkR_i \right) \right], \tag{C.24}$$

78

with

$$f_\rho^\pm = \frac{1}{h_i^2} \frac{\xi_{i\pm1}}{(1-\xi_i)^2} \frac{e^{-jkR_i}}{R_i} \left[1 + (jk + \frac{1}{R_i})(\xi_{i+1}\boldsymbol{\ell}_{i-1} - \xi_{i-1}\boldsymbol{\ell}_{i+1}) \cdot \hat{\boldsymbol{R}}_i \right], \quad (C.25)$$

and

$$f_R^\pm = \frac{1}{(\boldsymbol{R}_i \cdot \hat{\boldsymbol{h}}_i)^2} \left\{ \frac{\xi_{i\pm1}}{R} - \frac{2}{\boldsymbol{R}_i \cdot \hat{\boldsymbol{h}}_i} \left[\frac{\hat{\boldsymbol{h}}_{i\pm1} \cdot (\boldsymbol{\rho} - \boldsymbol{\rho}_i)}{h_{i\pm1}} \right] \right.$$

$$\left. \hat{\boldsymbol{h}}_i \cdot \left[\frac{(\boldsymbol{\rho} - \boldsymbol{\rho}_i) - (\xi_{i+1}\boldsymbol{\ell}_{i-1} - \xi_{i-1}\boldsymbol{\ell}_{i+1})}{R} \right] \right\} \quad (C.26)$$

The nonsingular integrand $F^\pm$ of (C.22) can be integrated numerically by Gaussian quadrature as described in Appendix E. The remaining integrals in (C.22) are singular and may be evaluated analytically as follows. From (E.7), we note the results

$$\int_{S^{Jq}} \frac{\xi_{i\pm1}}{(1-\xi_i)^2} \, dS' = 2A_i \int_0^1 \int_0^{1-\xi_i} \frac{\xi_{i\pm1}}{(1-\xi_i)^2} \, d\xi_{i\pm1} d\xi_i = A_i, \quad (C.27)$$

Similarly,

$$\int_{S^{Jq}} \frac{\xi_{i\pm1}^2}{(1-\xi_i)^2} \, dS' = \frac{1}{3}A_i, \qquad \int_{S^{Jq}} \frac{\xi_{i+1}\xi_{i-1}}{(1-\xi_i)^2} \, dS' = \frac{1}{6}A_i, \quad (C.28)$$

where A_i is the area of the triangular patch S^{Jq}. From (C.25-C.28), we now have

$$\int_{S^{Jq}} f_\rho^\pm \, dS' = \frac{A_i}{6} \frac{1}{h_i^2} \left\{ \frac{e^{-jkR_i}}{R_i} \left(6 + \frac{1+jkR_i}{R_i} \right. \right.$$

$$\left. \left. \left[(\hat{\boldsymbol{R}}_i \cdot \boldsymbol{\ell}_{i-1}) \begin{pmatrix} 2 \\ 1 \end{pmatrix} - (\hat{\boldsymbol{R}}_i \cdot \boldsymbol{\ell}_{i+1}) \begin{pmatrix} 1 \\ 2 \end{pmatrix} \right] \right) \right\}, \quad (C.29)$$

$$\int_{S^{Jq}} f_R^\pm \, dS' = \frac{1}{(\boldsymbol{R}_i \cdot \hat{\boldsymbol{h}}_i)^2} \left\{ \int_{S^{Jq}} \frac{\xi_{i\pm1}}{R} \, dS' - \frac{2}{\boldsymbol{R}_i \cdot \hat{\boldsymbol{h}}_i} \left[\frac{\hat{\boldsymbol{h}}_{i\pm1} \cdot (\boldsymbol{\rho} - \boldsymbol{\rho}_i)}{h_{i\pm1}} \right] \right.$$

$$\left. \hat{\boldsymbol{h}}_i \cdot \left[(\boldsymbol{\rho} - \boldsymbol{\rho}_i) \int_{S^{Jq}} \frac{1}{R} \, dS' - \boldsymbol{\ell}_{i-1} \int_{S^{Jq}} \frac{\xi_{i+1}}{R} \, dS' + \boldsymbol{\ell}_{i+1} \int_{S^{Jq}} \frac{\xi_{i-1}}{R} \, dS' \right] \right\} \quad (C.30)$$

From (B.8), (B.9), and (B.15), the singular integrals (C.29) and (C.30) both can be obtained explicitly.

C.3 Summary of Computation of Junction Potential Integrals

The vector potential integral associated with a vertex of a junction triangular patch as given by (C.3) is obtained by substituting (C.22-C.23), (C.25-C.26), and (C.29-C.30) into (C.20) and is summarized as follows:

$$\boldsymbol{A}_i^{J\prime}(\boldsymbol{r}) = \frac{\mu}{4\pi} K_i h_i \left(A_i^{J\prime+} \,\boldsymbol{\ell}_{i-1} - A_i^{J\prime-} \,\boldsymbol{\ell}_{i+1} \right), \tag{C.31}$$

where

$$
\begin{aligned}
A_i^{J\prime\pm} = \; & 2A_i \int_0^1 \int_0^{1-\xi_i} \left\{ \frac{1}{h_i^2} \frac{\xi_{i\pm1}}{(1-\xi_i)^2} \left(\frac{e^{-jkR}}{R} \right. \right. \\
& \left. - \frac{e^{-jkR_i}}{R_i} \left[1 + \left(jk + \frac{1}{R_i} \right)(\xi_{i+1}\boldsymbol{\ell}_{i-1} - \xi_{i-1}\boldsymbol{\ell}_{i+1}) \cdot \hat{\boldsymbol{R}}_i \right] \right) \\
& - \sigma(\boldsymbol{r}) \frac{1}{(\boldsymbol{R}_i \cdot \hat{\boldsymbol{h}}_i)^2} \left\{ \frac{\xi_{i\pm1}}{R} - \frac{2}{\boldsymbol{R}_i \cdot \hat{\boldsymbol{h}}_i} \left[\frac{\hat{\boldsymbol{h}}_{i\pm1} \cdot (\boldsymbol{\rho} - \boldsymbol{\rho}_i)}{h_{i\pm1}} \right] \right. \\
& \left. \left. \hat{\boldsymbol{h}}_i \cdot \left[\frac{(\boldsymbol{\rho} - \boldsymbol{\rho}_i) - (\xi_{i+1}\boldsymbol{\ell}_{i-1} - \xi_{i-1}\boldsymbol{\ell}_{i+1})}{R} \right] \right\} \right\} \, d\xi_{i\pm1} d\xi_i \\
& + \frac{A_i}{6h_i^2} \left\{ \frac{e^{-jkR_i}}{R_i} \left(6 + \frac{1+jkR_i}{R_i} \left[(\hat{\boldsymbol{R}}_i \cdot \boldsymbol{\ell}_{i-1}) \begin{pmatrix} 2 \\ 1 \end{pmatrix} - (\hat{\boldsymbol{R}}_i \cdot \boldsymbol{\ell}_{i+1}) \begin{pmatrix} 1 \\ 2 \end{pmatrix} \right] \right) \right\} \\
& + \sigma(\boldsymbol{r}) \frac{1}{(\boldsymbol{R}_i \cdot \hat{\boldsymbol{h}}_i)^2} \left\{ \frac{\hat{\boldsymbol{h}}_{i\pm1}}{h_{i\pm1}} \cdot \boldsymbol{g}_i - \frac{2}{\boldsymbol{R}_i \cdot \hat{\boldsymbol{h}}_i} \left[\frac{\hat{\boldsymbol{h}}_{i\pm1} \cdot (\boldsymbol{\rho} - \boldsymbol{\rho}_i)}{h_{i\pm1}} \right] \right. \\
& \left. \hat{\boldsymbol{h}}_i \cdot \left[(\boldsymbol{\rho} - \boldsymbol{\rho}_i)g_s + \boldsymbol{\ell}_{i-1} \frac{\hat{\boldsymbol{h}}_{i+1}}{h_{i+1}} \cdot \boldsymbol{g}_i - \boldsymbol{\ell}_{i+1} \frac{\hat{\boldsymbol{h}}_{i-1}}{h_{i-1}} \cdot \boldsymbol{g}_i \right] \right\},
\end{aligned} \tag{C.32}
$$

in which $\sigma(\boldsymbol{r})$, g_s, and $\boldsymbol{g}_i$ were defined as (B.5), (B.8), and (B.9).

Appendix D

Computation of Far Fields

We define a normalized far electric field $\mathcal{E}$ as

$$\mathcal{E}(\boldsymbol{r}) \equiv \lim_{r \to \infty} r \, e^{jkr} \, \boldsymbol{E}^s(\boldsymbol{r}) \tag{D.1}$$

in which the radial phase and amplitude dependence of the far field is removed, leaving only an angular dependence, and where, in the far field,

$$\boldsymbol{E}^s(\boldsymbol{r}) = -j\omega \left[\boldsymbol{A}(\boldsymbol{r}) - \boldsymbol{A}(\boldsymbol{r}) \cdot \hat{\boldsymbol{r}} \hat{\boldsymbol{r}} \right]. \tag{D.2}$$

The unit vector $\hat{\boldsymbol{r}}$ points in the direction of observation of the far field, and is given by

$$\hat{\boldsymbol{r}} = \frac{\boldsymbol{r}}{|\boldsymbol{r}|} = \hat{\boldsymbol{x}} \sin\theta \cos\phi + \hat{\boldsymbol{y}} \sin\theta \sin\phi + \hat{\boldsymbol{z}} \cos\theta.$$

In the far field, the vector potential $\boldsymbol{A}(\boldsymbol{r})$ reduces to

$$\boldsymbol{A}(\boldsymbol{r}) = \frac{\mu}{4\pi} \frac{e^{-jkr}}{r} \int_S \boldsymbol{J}(\boldsymbol{r}') \, e^{jk\hat{\boldsymbol{r}} \cdot \boldsymbol{r}'} \, dS' \tag{D.3}$$

which is evaluated in the same manner as (A.1), (B.1) and (C.1) except that the kernel $\frac{e^{-jkR}}{R}$ is replaced by $e^{jk\hat{\boldsymbol{r}} \cdot \boldsymbol{r}'}$. The various forms that the integrals take on are summarized in the following sections.

D.1 Far Field Vector Potentials for Wire Basis Functions

The vector potential in the far field due to a unit current source across the nth node of a wire is given as

$$A_n^W(\ell) = \frac{\mu}{4\pi} \frac{e^{-jkr}}{r} \int_{S_n^W} \Lambda_n^W(\ell') e^{jk\hat{\boldsymbol{r}}\cdot\boldsymbol{r}'} \; d\ell'$$

$$= \frac{\mu}{4\pi} \frac{e^{-jkr}}{r} \left[\int_{S_n^{W+}} \frac{\rho^+}{h_n^{W+}} e^{jk\hat{\boldsymbol{r}}\cdot\boldsymbol{r}'} \; d\ell' + \int_{S_n^{W-}} \frac{\rho^-}{h_n^{W-}} e^{jk\hat{\boldsymbol{r}}\cdot\boldsymbol{r}'} \; d\ell' \right] \qquad (D.4)$$

This integral may be evaluated in closed form, but it is generally more efficient to evaluate it by Gaussian quadrature.

D.2 Far Field Vector Potentials for Body Basis Functions

The vector potential evaluated in the far field point due to a basis current directed outward across the ith ($i = 1, 2,$ or 3) edge of a triangular patch S^{Bq} is given by

$$A_i^B(\boldsymbol{r}) = \frac{\mu}{4\pi} \int_{S^{Bq}} \frac{\rho'_i}{h_i} e^{jk\hat{\boldsymbol{r}}\cdot\boldsymbol{r}'} \; dS', \qquad (D.5)$$

which, using (E.5) and (E.7), may be expressed as

$$A_i^B(\boldsymbol{r}) = \frac{\mu\ell_i}{4\pi} \frac{e^{-jkr}}{r} \left[A_i^{B+} \boldsymbol{\ell}_{i-1} - A_i^{B-} \boldsymbol{\ell}_{i+1} \right], \qquad (D.6)$$

where

$$A_i^{B\pm} = \int_0^1 \int_0^{1-\xi_i} \xi_{i\pm1} e^{jk\hat{\boldsymbol{r}}\cdot\boldsymbol{r}'} \; d\xi_{i\pm1} \; d\xi_i. \qquad (D.7)$$

The integrals in (D.7) may be evaluated in closed form, but it is generally more efficient to evaluate them by numerical quadrature as described in Appendix E.

D.3 Far Field Vector Potentials for Junction Basis Functions

In the far field, the vector potential integral associated with a vertex of a junction triangular patch as given in (C.3) becomes the following:

$$A_i^{J'}(\boldsymbol{r}) = \frac{\mu}{4\pi} K_i \, h_i \, \frac{e^{-jkr}}{r} \int_{S^{J_q}} \frac{\boldsymbol{\rho'}_i}{(\boldsymbol{\rho'}_i \cdot \hat{\boldsymbol{h}}_i)^2} \, e^{jk\hat{\boldsymbol{r}}\cdot\boldsymbol{r}'} \, dS'. \tag{D.8}$$

Note that there is still a singularity at $\boldsymbol{\rho'}_i = 0$, i.e., when the source point is at the junction vertex. The treatment of Appendix C may be adapted to remove the singularity from the integrand with the result that the final form of $A_i^{J'}$ in the far field becomes

$$A_i^{J'}(\boldsymbol{r}) = \frac{\mu \ell_i K_i}{4\pi} \frac{e^{-jkr}}{r} \left[A_i^{J'+} \boldsymbol{\ell}_{i-1} - A_i^{J'+} \boldsymbol{\ell}_{i+1} \right], \tag{D.9}$$

where

$$
\begin{aligned}
A_i^{J'\pm} &= \int_0^1 \int_0^{1-\xi_i} \frac{\xi_{i\pm1}}{(1-\xi_i)^2} \left[e^{jk\hat{\boldsymbol{r}}\cdot\boldsymbol{r}'} - e^{jk\hat{\boldsymbol{r}}\cdot\boldsymbol{r}_i} \right] \, d\xi_{i\pm1} \, d\xi_i \\[2mm]
&+ e^{jk\hat{\boldsymbol{r}}\cdot\boldsymbol{r}_i} \int_0^1 \int_0^{1-\xi_i} \frac{\xi_{i\pm1}}{(1-\xi_i)^2} d\xi_{i\pm1} \, d\xi_i \\[2mm]
&= \int_0^1 \int_0^{1-\xi_i} \frac{\xi_{i\pm1}}{(1-\xi_i)^2} \left[e^{jk\hat{\boldsymbol{r}}\cdot\boldsymbol{r}'} - e^{jk\hat{\boldsymbol{r}}\cdot\boldsymbol{r}_i} \right] \, d\xi_{i\pm1} \, d\xi_i + \frac{e^{jk\hat{\boldsymbol{r}}\cdot\boldsymbol{r}_i}}{2}. \tag{D.10}
\end{aligned}
$$

The integrals in the last line of (D.10) may be evaluated by numerical quadrature as described in Appendix E.

Appendix E

Local Coordinates and Numerical Integration on Triangular Patches

In this Appendix, we introduce a convenient set of local coordinates defined on triangular patches. This set of coordinates is useful for representing both scalar and vector functions on triangles and for performing numerical integration over the patches.

E.1 Normalized Area Coordinate System

We introduce the so-called normalized area coordinates ξ_i ($i = 1, 2, 3$), defined as

$$\xi_i = \frac{A_i}{A}, \tag{E.1}$$

where the area A_i is the area of the triangle formed by point r and edge i (Fig. E.1), and A is the total area of triangle S^q. Hence

$$\sum_{i=1}^{3} \xi_i = 1. \tag{E.2}$$

Clearly, only two of the coordinates are independent, and the third can always be eliminated via (E.2). The transformation between the global and local coordinate systems is summarized by the relation

$$r = \xi_{i+1} r_{i+1} + \xi_{i-1} r_{i-1} + \xi_i r_i \tag{E.3}$$
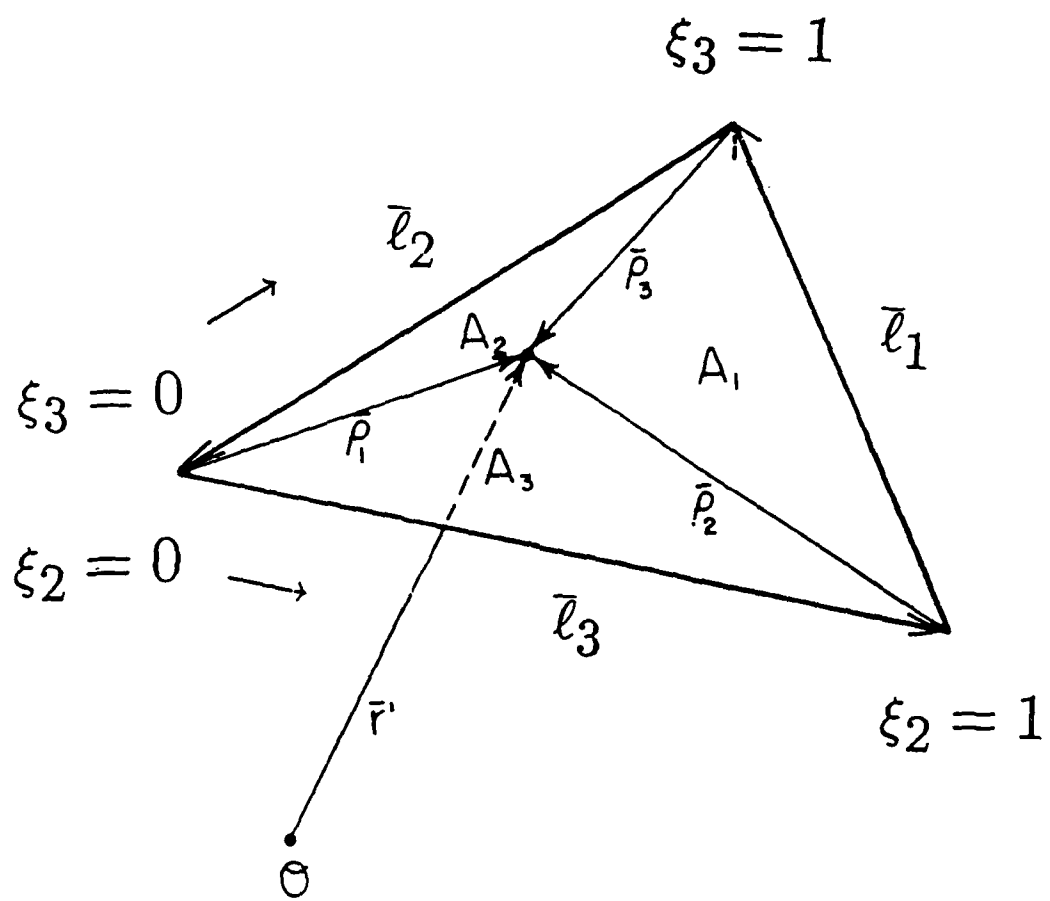
Figure E.1: Definition of local coordinate system.

where the position vector r and the vertex vectors r_1, r_2, and r_3 are given in the global coordinate system. Using (E.2) to express the position vector in terms of the two independent coordinates $\xi_{i\pm1}$ and ξ_i, and noting that $r_{i\pm1} - r_{i\mp1} = \mp\ell_i$ and $r_{i\mp1} - r_i = \mp\ell_{i\pm1}$, we have

$$
\begin{aligned}
r &= (1 - \xi_{i\pm1} - \xi_i)r_{i\mp1} + \xi_{i\pm1}r_{i\pm1} + \xi_i r_i \\
&= \mp(\xi_{i\pm1}\ell_i - \xi_i\ell_{i\pm1}) + r_{i\mp1}.
\end{aligned}
\tag{E.4}
$$

A frequently used result is that

$$
\begin{aligned}
\rho'_i &= r' - r_i \\
&= \xi_{i+1}r_{i+1} + \xi_{i-1}r_{i-1} + (\xi_i - 1)r_i \\
&= \xi_{i+1}r_{i+1} + \xi_{i-1}r_{i-1} - (\xi_{i+1} + \xi_{i+1})r_i \\
&= \xi_{i+1}\ell_{i-1} - \xi_{i-1}\ell_{i+1}.
\end{aligned}
\tag{E.5}
$$

From (E.4) we also have

$$
\begin{aligned}
dS' &= |\frac{\partial r(\xi_{i\pm1}, \xi_i)}{\partial \xi_{i\pm1}} \times \frac{\partial r(\xi_{i\pm1}, \xi_i)}{\partial \xi_i}| \, d\xi_{i\pm1} \, d\xi_i \\
&= |\ell_i \times \ell_{i\pm1}| \, d\xi_{i\pm1} \, d\xi_i \\
&= 2A \, d\xi_{i\pm1} \, d\xi_i.
\end{aligned}
\tag{E.6}
$$

From (E.5) and (E.6), it follows that surface integrals over an arbitrary scalar function $f(\rho'_i)$ on S^q can be expressed in terms of local coordinates as

$$
\int_{S^q} f(\rho'_i) \, dS' = 2A \int_0^1 \int_0^{1-\xi_i} f(\xi_{i+1}\ell_{i-1} - \xi_{i-1}\ell_{i+1}) \, d\xi_{i\pm1} \, d\xi_i.
\tag{E.7}
$$

E.2 Expansion of Tangent Vectors on a Triangle in Terms of Edge Vectors

Any tangent vector in S^q can be expressed in terms of a pair of triangle edge vectors, which act as basis vectors in the local coordinate system. For an arbitrary tangent vector f, for example, we wish to write it as

$$f = f^+ \boldsymbol{\ell}_{i-1} - f^- \boldsymbol{\ell}_{i+1}, \tag{E.8}$$

i.e., we wish to determine its expansion coefficients f^+ and f^- in terms of (non-orthogonal) basis vectors $\boldsymbol{\ell}_{i-1}$ and $\boldsymbol{\ell}_{i+1}$. This is easily done once we notice that (c.f. Fig. E.2)

$$\boldsymbol{h}_i \cdot \boldsymbol{\ell}_i = 0, \tag{E.9}$$

(i.e. $\boldsymbol{\ell}_i$ and $\boldsymbol{h}_i$ are *biorthogonal*) where $\boldsymbol{h}_i = h_i \hat{\boldsymbol{h}}_i$. Hence, from (E.8) and (E.9), and since

$$\boldsymbol{h}_{i\pm1} \cdot \boldsymbol{\ell}_{i\mp1} = \mp h_{i\pm1}^2,$$

we have

$$\boldsymbol{h}_{i\pm1} \cdot \boldsymbol{f} = \pm f^\pm \, \boldsymbol{h}_{i\pm1} \cdot \boldsymbol{\ell}_{i\mp1} = - f^\pm \, h_{i\pm1}^2.$$

Thus

$$f^\pm = - \frac{\hat{\boldsymbol{h}}_{i\pm1}}{h_{i\pm1}} \cdot \boldsymbol{f}. \tag{E.10}$$

and finally, from (E.8),

$$\boldsymbol{f} = \left(-\frac{\boldsymbol{\ell}_{i-1}\hat{\boldsymbol{h}}_{i+1}}{h_{i+1}} + \frac{\boldsymbol{\ell}_{i+1}\hat{\boldsymbol{h}}_{i-1}}{h_{i-1}} \right) \cdot \boldsymbol{f} \tag{E.11}$$

where the quantity in parentheses is the identity dyad in local coordinates, multiplication by which expresses a tangent vector in terms of the triangle's edge vectors. Since the vectors $\boldsymbol{\ell}_{i\pm1}$ in (E.8) are constant, a frequent use of this result is to reduce an integral over an arbitrary vector $\boldsymbol{f}$ to two scalar integrals of the form of (E.7) over the components $f^\pm$.

E.3 Numerical Integration over Triangular Patches

Numerical integration over a triangle can be accomplished in terms of the area coordinates by the following rule:
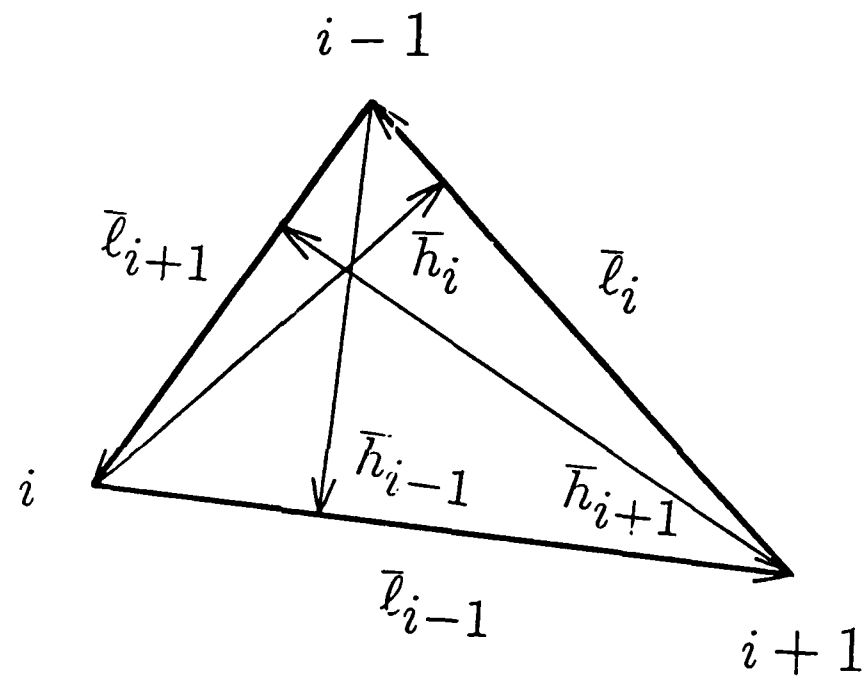
Figure E.2: Definition of triangle edge and height vectors.

$$\int_0^1 \int_0^{1-\xi_{i\pm1}} f(\xi_i, \xi_{i\pm1}) \, d\xi_i \, d\xi_{i\pm1} \approx \sum_{j=1}^{N} w_j \, f((\xi_i)_j, (\xi_{i\pm1})_j), \qquad (E.12)$$

where N is the number of evaluation points of the quadrature. Appropriate weight coefficients w_j and coordinates $((\xi_i)_j, (\xi_{i\pm1})_j)$ of points at which the function must be evaluated for Gaussian schemes are given in [29]. Only one-point, three-point, and seven-point schemes (depending on the ratio of distance between observation point and centroid to the maximum edge length of the source triangular patch) are used in the code JUNCTION, and the corresponding weight coefficients and corresponding coordinates are presented in Tables E.1-E.3.

Table E.1: Weight Coefficients and Local Coordinates for One-Point Gaussian Quadrature on a Triangle.

j	w_j	$(\xi_i)_j$	$(\xi_{i\pm1})_j$
1	0.5	0.333333333333333	0.333333333333333

Table E.2: Weight Coefficients and Local Coordinates for Three-Point Gaussian Quadrature on a Triangle.

j	w_j	$(\xi_i)_j$	$(\xi_{i\pm1})_j$
1	0.166666666666667	0.666666666666667	0.166666666666667
2	0.166666666666667	0.166666666666667	0.666666666666667
3	0.166666666666667	0.166666666666667	0.166666666666667

Table E.3: Weight Coefficients and Local Coordinates for Seven-Point Gaussian Quadrature on a Triangle.

j	w_j	$(\xi_i)_j$	$(\xi_{i\pm1})_j$
1	0.1125	0.333333333333333	0.333333333333333
2	0.062969590272413	0.797426985353087	0.101286507323456
3	0.062969590272413	0.101286507323456	0.797426985353087
4	0.062969590272413	0.101286507323456	0.101286507323456
5	0.066197076394253	0.470142064105115	0.470142064105115
6	0.066197076394253	0.470142064105115	0.059715871789770
7	0.066197076394253	0.059715871789770	0.470142064105115

Acknowledgements

Bibliography

[1] R. F. Harrington, *Field Computations by Moment Methods.* New York: MacMillan, 1968.

[2] S. M. Rao, D. R. Wilton, and A. W. Glisson, "Electromagnetic Scattering by Surfaces of Arbitrary Shape," *IEEE Transactions on Antennas and Propagation,* Vol. AP-30, No. 3, pp. 409-418, May 1982.

[3] D. M. Bolle and M. D. Morganstern, "Monopole and Conic Antennas on Spherical Vehicles," *IEEE Transactions on Antennas and Propagation,* Vol. AP-17, No. 4, pp. 477-484, July 1969.

[4] F. M. Tesche and A. R. Neureuther, "The Analysis of Monopole Antennas Located on a Spherical Vehicle: Part 1 and Part 2," *IEEE Transactions on Electromagnetic Compatibility,* Vol. EMC-18, No. 1, pp. 2-15, Feb. 1976.

[5] Leonard L. Tsai, "Analysis and Measurement of A Dipole Antenna Mounted Symmetrically on A Conducting Sphere or Cylinder," Technical Report No. 2648-3, ElectroScience Laboratory, Ohio State University, 1970.

[6] Lee J. Cooper and Ronold W. P. King, "Monopole Antennas on Electrically Thick Conducting Cylinders," Technical Report No. 660, Division of Engineering and Applied Physics, Harvard University, 1975.

[7] N. C. Albertsen, J. E. Hansen and N. E. Jensen, "Computation of Radiation from Wire Antennas on Conducting Bodies," *IEEE Transactions on Antennas and Propagation,* Vol. AP-22, No. 2, pp. 200-206, March 1974.

[8] J. F. Shaeffer and L. N. Medgyesi-Mitschang, "Radiation from Wire Antennas Attached to Bodies of Revolution: The Junction Problem," *IEEE Transactions on Antennas and Propagation,* Vol. AP-29, No. 3, pp. 479-487, May 1981.

[9] J. F. Shaeffer, "EM Scattering from Bodies of Revolution with Attached Wires," *IEEE Transactions on Antennas and Propagation,* Vol. AP-30, No. 3, pp. 426-431, May 1982.

[10] L. N. Medgyesi-Mitschang and J. M. Putnam, "Formulation for Wire Radiators on Bodies of Translation With and Without End Caps," *IEEE Transactions on Antennas and Propagation,* Vol. AP-31, No. 6, pp. 853-862, Nov. 1983.

[11] J. H. Richmond, "Monopole Antenna on a Circular Disk," *IEEE Transactions on Antennas and Propagation,* Vol. AP-32, No. 12, pp. 1282-1287, Dec. 1984.

[12] M. Marin and M. F. Catedra, " A Study of a Monopole Arbitrarily Located on a Disk Using Hybrid MM/GTD Techniques," *IEEE Transactions on Antennas and Propagation,* Vol. AP-35, No. 3, pp. 287-292, March 1987.

[13] A. W. Glisson and D. R. Wilton, "Simple and Efficient Numerical Methods for Problems of Electromagnetic Radiation and Scattering from Surfaces," *IEEE Transactions on Antennas and Propagation,* Vol. AP-28, No. 5, pp. 593-603, Sept. 1980.

[14] A. W. Glisson, "On the Development of Numerical Techniques for Treating Arbitrarily-Shaped Surfaces," Ph.D. dissertation, University of Mississippi, 1978.

[15] E. H. Newman and D. M. Pozar, "Electromagnetic Modeling of Composite Wire and Surface Geometries," *IEEE Transactions on Antennas and Propagation,* Vol. AP-26, No. 6, pp. 784-789, November 1978.

[16] E. H. Newman and D. M. Pozar, "Considerations for Efficient Wire/Surface Modeling," *IEEE Transactions on Antennas and Propagation,* Vol. AP-28, No. 1, pp. 121-125, Jan. 1980.

[17] D. M. Pozar and E. H. Newman, "Analysis of a Monopole Mounted Near or at the Edge of a Half-plane," *IEEE Transactions on Antennas and Propagation,* Vol. AP-29, No. 3, pp. 488-495, May 1981.

[18] D. M. Pozar and E. H. Newman, "Analysis of a Monopole Mounted Near an Edge or a Vertex," *IEEE Transactions on Antennas and Propagation,* Vol. AP-30, No. 3, pp. 401-408, May 1982.

[19] S. M. Rao, "Electromagnetic Scattering and Radiation of Arbitrary Shape Surfaces by Triangular Patch Modeling," Ph.D. dissertation, University of Mississippi, August 1980.

[20] M. F. Costa and R. F. Harrington, "Minimization of Radiation from Computer Systems," International Electrical Electronics Conference and Exposition proceedings, Toronto, Canada, pp. 660-665, Sept. 1983.

[21] M. F. Costa and R. F. Harrington, "Electromagnetic Radiation and Scattering from a System of Conducting Bodies Interconnected by Wires," Report TR-83-8, Syracuse University, April 1983.

[22] D. R. Wilton and S. U. Hwu, "JUNCTION CODE USER'S MANUAL", Technical Report No. 87-18, Applied Electromagnetics Laboratory, Department of Electrical

Engineering, University of Houston, 1987.

[23] R. F. Harrington, *Time-Harmonic Electromagnetic Fields.* New York: McGraw - Hill, 1961, pp. 232-235.

[24] Qinglun Chen and D. R. Wilton, "Computation of Magnetostatic Current Distributions Near Wire-To-Surface Junctions," National Radio Science Meeting Digest, Syracuse, NY, June 1988.

[25] S. Bhattacharya, S. A. Long, and D. R. Wilton, "The Input Impedance of a Monopole Antenna Mounted on a Cubical Conducting Box," *IEEE Transactions on Antennas and Propagation,* Vol. AP-35, No. 7, pp. 756-762, July 1987.

[26] R. W. P. King, *The Theory of Linear Antennas.* Harvard University Press, Massachusetts, 1956.

[27] M. Abramowitz and I. A. Stegun, Eds., *Handbook of Mathematical Functions, Applied Mathematics Series 55,* U. S. Printing Office, 1964.

[28] D. R. Wilton, S. M. Rao, A. W. Glisson, D. H. Schaubert, O. M. Al-Bundak, and C. M. Butler, "Potential Integrals for Uniform and Linear Source Distributions on Polygonal and Polyhedral Domains," *IEEE Transactions on Antennas and Propagation,* Vol. AP-32, No. 3, pp. 276-281, March 1984.

[29] G. Strang and G. Fix, *An Analysis of the Finite Element Method,* Englewood Cliffs, N. J.: Prentice-Hall, 1973.

[30] W. A. Johnson, D. R. Wilton, and R. M. Sharpe, "PATCH Code User's Manual," Sandia National Laboratories, Albuquerque, N.M. 87185, 1988.

[31] S. U. Hwu, D. R. Wilton, and S. M. Rao, "Electromagnetic Scattering and Radiation by Arbitrary Conducting Wire/Surface Configurations," *1988 International Symposium Digest - Antennas and Propagation*, Syracuse, NY, June, 1988.

[32] D. R. Wilton, and S. U. Hwu, "A Numerical Approach to Modeling Wires Attached to Surfaces," *National Radio Science Meeting Digest*, Philadelphia, PA, June 1986.

[33] W. A. Johnson, D. R. Wilton, R. M. Sharpe and S. U. Hwu, "Current Progress in the Development of and Modeling with the Electric Field Integral Equation Surface Patch Code," *1985 International Symposium Digest - Antennas and Propagation*, Vancouver, Canada, pp. 263-264, June, 1985.

INITIAL DISTRIBUTION

U.S. NAVY

Office of Naval Research
Arlington, VA 22203-5000
    ONNR-211

Naval Weapons Center
China Lake, CA 93555
    Code 35203

David Taylor Research Center
Bethesda, MD 20084-5000
    Code 0119

Pacific Missile Test Center
Point Mugu, CA 93042
    Code 3242

Naval Postgraduate School
Monterey, CA 93940
    Code 62AB

U.S. ARMY

U.S. Army Communications Electronics Command
Fort Monmouth, NJ 07703-5202
    AMSEL-COM-TN-4

U.S. Army Information Systems Engineering Installation Activity
Fort Huachuca, AZ 85613-7300
    ASBH-SET-P

U.S. AIR FORCE

Rome Air Development Center
Hanscom Air Force Base, MA 01731

OTHER

Lawrence Livermore Laboratory
Livermore, CA 94550

Defense Technical Information Center
Alexandria, VA 22314